

Towards non-parametric reconstruction of axon diameter distributions using diffusion MRI and regularized discrete linear modeling

Thèse N° 9091

Présentée le 25 janvier 2019

à la Faculté des sciences et techniques de l'ingénieur

Laboratoire de traitement des signaux 5

Programme doctoral en génie électrique

pour l'obtention du grade de Docteur ès Sciences

par

DAVID PAUL ROGER ROMASCANO

Acceptée sur proposition du jury

Prof. D. N. A. Van De Ville, président du jury

Prof. J.-Ph. Thiran, Prof. T. B. Dyrby, directeurs de thèse

Prof. E. Fieremans, rapporteuse

Dr G. Zhang, rapporteur

Dr I. Jelescu, rapporteuse

2019

Acknowledgements

I would first like to thank my supervisor, Prof. Jean-Philippe Thiran, for giving me the opportunity to work in the exciting and complex field that is diffusion MRI, his guidance when I needed assistance and in particular the support he gave me to share our contributions with the research community, fostering international collaborations and mobility projects abroad. I would then like to thank Prof. Alessandro Daducci, for introducing me to microstructure imaging and the AMICO framework that he developed, as well as Dr Anna Auría, who wisely advised me and oriented me during the first part of my PhD thesis. The work presented in this thesis was also closely supervised by my co-supervisor, Prof. Tim B. Dyrby, who I'd like to thank for his patience and pedagogy, in particular regarding the long sessions we spent with the preclinical scanner. I particularly enjoyed the time I was able to spend in Denmark and hope we will continue to work together. Among senior researchers in the lab, I would like to thank Dr. Erick Canales-Rodriguez, mainly for introducing me to the theory of Dr. Chunlei Liu and Higher Order Tensors, as well as the many discussions regarding the derivation of the HOTmix model. I would also like to thank Prof. Giorgio Innocenti, for his wise and precious insight on the real white matter structure and objective criticism regarding the simplifications made in our models. This work was also strongly supported by my labmates, starting with Muhamed Barakovic, who I'd like to thank for his eternal positiveness and emotional support, discussions on crazy (and not so crazy) ideas, and the organization of trips and activities with the lab. We travelled almost everytime together and I really enjoyed sharing these trips with him. I wish you the best for the rest of your PhD. Next, I would like to thank Mr. Jonathan Rafael Patiño Lopez, or Jonathan Rafael-Patiño, or Jony. All the simulations presented in this manuscript would not have been possible without his amazing c++ coding skills, distilled into the MC/DC Simulator. Sorry if I kept pushing the limits, but your simulator handled everything like a charm. Thank you also to Gab, Marco, Gaëtan, Thomas and Francesco, for very useful discussions, proofreading parts of this manuscript, pointing out errors in model implementations, and very nice moments spent together inside and outside the lab. Finally, I would like to thank the jury present at my oral exam, the president Prof. Dimitri Van De Ville, the external experts Prof. Els Fieremans and Dr Gary Zhang, and the internal expert Dr Ileana Jelescu, for the thorough evaluation of my initial manuscript, the constructive discussion during the exam, and the detailed comments to improve the content of my final manuscript.

Lausanne, 15th of December 2018

D. R.

Résumé

La distribution des diamètres axonaux (DDA) est une caractéristique importante de la substance blanche : elle influence la vitesse des potentiels d'action, évolue pendant le développement et est affectée lors d'événements pathologiques. L'imagerie de diffusion par résonance magnétique est un outil puissant, non invasif, et sensible au déplacement des molécules d'eau. Les diamètres axonaux étant bien en dessous de la résolution de l'image, la DDA est estimée indirectement en ajustant un modèle biophysique au signal mesuré. L'imagerie microstructurale se base sur ce principe et utilise des modèles compartimentaux, séparant l'espace intra-axonal et extra-axonal. La reconstruction de la DDA demeure un problème difficile en pratique, notamment à cause de la dégénérescence du problème (des solutions différentes peuvent avoir des signaux similaires), le diamètre minimum visible par le scanner, ainsi que la difficulté de modéliser le signal extra-axonal de manière adéquate.

Dans cette thèse, nous avons abordé le problème en nous concentrant séparément sur le compartiment intra-axonal et extra-axonal. La précision des différents modèles a été évaluée en comparant les estimations avec la valeur réelle fournie par des simulations de Monte Carlo.

La dégénérescence a été abordée en utilisant une régularisation de Laplace, qui a fourni des estimations plus précises de la DDA à partir du signal intra-axonal. La sensibilité aux petits diamètres a été améliorée par l'utilisation d'un protocole de diffusion conçu pour maximiser la sensibilité à un ensemble de diamètres, ayant permis de reconstruire des distributions unimodales et bimodales, sensibles aux changements spécifiques à une des populations.

En ce qui concerne l'espace extra-axonal, nous avons montré que l'utilisation d'un mélange de tenseurs d'ordre supérieur améliore la reconstruction du signal par rapport aux modèles standards. Le modèle proposé est suffisamment flexible pour s'adapter à la variété de signaux simulés, surpassant les modèles actuels.

L'estimation de la DDA à partir de signaux contenant les deux compartiments a été légèrement améliorée. La similitude entre les signaux intra-axonaux et extra-axonaux pourrait cependant être le principal facteur limitant lors de l'utilisation de séquences de type PGSE.

Mots-clefs : IRM de diffusion, distribution de diamètres axonaux, problèmes inverses, imagerie de microstructure, Monte Carlo.

Abstract

The distribution of axon diameters (ADD) is an important white matter feature: it influences action potential speed, it has been shown to evolve during development, and also to be affected during pathological processes. Diffusion Magnetic Resonance Imaging is a powerful non-invasive tool that is sensitive to the displacement of water molecules. In theory, as axon diameters are well below the imaging resolution, the ADD can be estimated indirectly by fitting a biophysical model to the measured signal. Such an approach is the basis of microstructure imaging. Microstructure imaging usually relies on compartment models, splitting the signal into the intra-axonal or the extra-axonal compartments. However, in practice, ADD reconstruction remains a challenging problem, mainly due to model degeneracy (different solutions can have similar signals), the diameter lower bound which dictates the smallest diameter visible by the scanner, and the difficulty in modeling properly the extra-axonal signal.

In this thesis, we addressed the challenges at stake by focusing on the intra-axonal and extra-axonal compartments separately. Model performance was evaluated by comparing estimates with the ground-truth provided by Monte Carlo simulations.

Model degeneracy was addressed by introducing Laplacian regularization, which was shown to provide better ADD estimates when considering the intra-axonal signal only. Sensitivity to small diameters was improved by using a richer diffusion protocol designed to maximize sensitivity to a set of diameters, which was shown to provide reconstruction of unimodal and bimodal distributions, with sensitivity to population specific changes.

Regarding the extra-axonal space, using a mixture of higher order tensors improved reconstruction of the signal compared to standard models. The proposed model is flexible enough to adapt to a variety of simulated signals, outperforming current models of hindered diffusion.

Combining the results for both compartments slightly improved estimates for some of the simulated signals. We highlighted the similarity between the intra-axonal and extra-axonal signals, which might be the main limiting factor when using single Pulsed Gradient Spin Echo sequences.

Keywords: diffusion MRI; axon diameter distribution; inverse problems; microstructure imaging; Monte Carlo.

Contents

Acknowledgements	iii
Abstract (Français/English)	v
List of figures	xi
List of tables	xiv
1 Introduction	1
2 Theory and State-of-the-art	7
2.1 White matter	7
2.2 Diffusion weighted imaging (DWI)	9
2.3 Microstructure imaging	10
2.3.1 Signal models	11
2.3.2 Statistical models	13
2.3.3 Compartment models	14
2.4 Inverse problems	16
2.4.1 Microstructure imaging as an inverse problem	16
2.4.2 ActiveAx _{AMICO}	17
2.4.3 NODDI _{AMICO}	17
2.4.4 Non-parametric ADD estimation	18
2.5 Validation and model evaluation	20
2.5.1 Microscopy	20
2.5.2 Monte-Carlo simulations	22
2.5.3 Volume weighting	22
2.6 Conclusion	23
3 Effect of voxel size on the dMRI signal	25
3.1 Introduction	25
3.2 Methods	26
3.3 Results	27
3.4 Discussion	28
3.5 Conclusion	29

Contents

4	ADD estimation using ActiveAx_{ADD}	31
4.1	Introduction	31
4.2	Theory	32
4.3	Methods	33
4.3.1	Substrate design	33
4.3.2	Estimates from the IA compartment's signal	33
4.3.3	Influence of maximal gradient strength	35
4.3.4	Influence of the EA compartment	35
4.4	Results	35
4.4.1	Estimates from the IA compartment's signal	35
4.4.2	Influence of maximal gradient strength	36
4.4.3	Influence of the EA compartment	36
4.5	Discussion	38
4.6	Conclusion	42
5	Reconstruction of unimodal and multimodal distributions	43
5.1	Introduction	43
5.2	Methods	44
5.3	Results & Discussion	45
5.4	Conclusions	47
6	Modeling hindered diffusion using HOTmix	49
6.1	Introduction	49
6.2	Methods	50
6.2.1	Axi-symmetric HOT	50
6.2.2	Derivation of the HOTmix model	51
6.2.3	Link with a mixture of gaussians with time-dependent variance	52
6.2.4	Monte Carlo simulations	53
6.2.5	Fitting perpendicular signals	53
6.2.6	Fitting of 3D signals	56
6.2.7	HOTmix parameters and substrate properties	58
6.2.8	Dyneema phantom	58
6.2.9	MRI acquisition and processing	59
6.3	Results	61
6.3.1	Ex vivo WM signals	61
6.3.2	HOTmix parameters and substrate properties	63
6.3.3	In vivo WM signals	64
6.3.4	Dyneema phantom	67
6.4	Discussion	69
6.5	Conclusion	70

7	Joint model	71
7.1	Introduction	71
7.2	Methods	71
7.3	Results	72
7.4	Discussion	73
7.5	Conclusion	74
8	Conclusion	77
8.1	Perspectives	77
A	Appendix: Derivation of the axi-symmetric HOT model	81
	Bibliography	93
	Curriculum Vitae	95

List of Figures

2.1	Schematic of the brain's organization	7
2.2	Axon structure	8
2.3	EM section of axons showing the distribution of axon diameters	9
2.4	PGSE protocol showing the gradient amplitude G , duration δ and separation Δ	9
2.5	Number weighted and volume weighted ADD	19
2.6	AxCaliber estimates compared to Electron Microscopy	20
2.7	ActiveAx estimates compared to Electron Microscopy	21
2.8	ADD estimates compared to histology	22
2.9	Virtual WM structure used for MC simulations	23
3.1	Effect of voxel size on the MC signal for three different substrates.	28
3.2	Effect of voxel size on the mean radial MC signal and its anisotropy.	29
4.1	Properties of the substrates with smallest, medium and biggest mean diameter index used in the study	34
4.2	Estimated a' for different methods using the IA signal only	37
4.3	ADD estimates compared to the ground truth.	38
4.4	Effect of G_{\max} on the estimated ADD using ActiveAx _{ADD} on IA signals.	39
4.5	Influence of the EA compartment on the estimated ADD.	40
4.6	Hellinger distance between all reconstructed ADDs and the ground-truth.	40
4.7	Effect of the EA compartment on the estimated mean diameter index	41
5.1	Selected shells for increased diameter sensitivity	45
5.2	ADD and diameter index from optimized protocol and IA signal only	45
5.3	Estimated means for bimodal distributions	46
5.4	Sensitivity to population specific changes in bimodal distributions	47
6.1	Illustration of the pipeline used to generate EA dMRI signals for 2 different virtual samples	54
6.2	Dyneema phantoms in closed plastic tube before MRI acquisition.	60
6.3	High resolution T2 weighted scan of the dyneema phantoms.	61
6.4	Reconstructed signals using DT, KT, HOT and HOTmix	62
6.5	Fitting errors for DT, KT, HOT and HOTmix	63
6.6	HOTmix parameter values for two substrates	64

List of Figures

6.7	HOTmix features compared to substrate properties	65
6.8	Reconstructed signals for in vivo settings	66
6.9	Fitting error for in vivo signals	67
6.10	Reconstruction of MC simulated Dyneema phantom signals	68
6.11	Reconstruction of Dyneema phantom signals	68
7.1	Effect of using different EA models on the estimated ADD	75

List of Tables

4.1	Properties of ADD mapping methods	32
6.1	dMRI protocol for $\mathbf{D}_0 = 0.6 \times 10^{-3} \text{mm}^2/\text{s}$	55
6.2	dMRI protocol for $\mathbf{D}_0 = 2.0 \times 10^{-3} \text{mm}^2/\text{s}$	55
6.3	Composition of dyneema phantoms	59
6.4	Imaging parameters for MRI acquisitions	60

1 Introduction

This thesis focuses on the reconstruction of axon diameter distributions through diffusion Magnetic Resonance Imaging (dMRI). The work was conducted under supervision of Professor Thiran (École Polytechnique Fédérale de Lausanne (EPFL), Switzerland) and Professor Dyrby (Danish Research Center for Magnetic Resonance (DRCMR) and Danish Technical University (DTU), Denmark), from November 2014 to November 2018.

The Axon Diameter Distribution (ADD) is an important feature of White Matter (WM) fascicles, and is of interest in neuroscience and neurology. By exploiting the protons' response to varying magnetic fields, MRI scanners can be used to probe microstructural properties of the brain tissue non-invasively. ADD estimation is nevertheless a challenging problem. To recover the ADD (which is several order of magnitude smaller than the imaging resolution), a compartment model is fit to the signal. It appears that the problem is very ill-posed (different solutions can have similar signals). MRI hardware and diffusion protocols also control the diameter lower bound, which is the smallest diameter visible by the scanner. This lower bound can in some cases mask most of the diameters present in white matter fascicles. Currently, there's also a difficulty in modeling properly the extra-axonal (EA) signal, with residuals affecting the estimates of intra-axonal (IA) parameters.

To understand and push the limits of ADD reconstruction, we studied the IA and EA compartments using simulated data. Our simulations have the strong hypothesis that WM consists of impermeable and parallel cylinders, with a mean diameter varying between 0.6 and 3.2 μm . Such assumptions might deviate from real WM tissue, but the aim was to show that despite such a simplified picture of the WM, ADD estimation remained a challenging problem.

Content of the thesis

The content of the chapters presented in this thesis are the following:

1. Chapter 2: Summary of the state of the art and theory regarding WM tissue, microstruc-

ture imaging models and validation/evaluation methods.

2. Chapter 3: Effect of voxel size on the EA dMRI signals generated using Monte Carlo simulations. Voxel size should be considered to avoid bias when evaluating performance of the ADD reconstruction methods presented in the remaining chapters.
3. Chapter 4: Improved model for the IA compartment. The ActiveAx_{AMICO} model (designed for mean diameter mapping) is extended to ADD mapping. ADD estimation is shown to be reliable when considering only the IA signal. Addition of the EA signal results in lower reconstruction accuracy when using a standard model for the EA signal.
4. Chapter 5: Reconstruction of unimodal and bimodal ADDs using a protocol designed to maximize sensitivity to a set of diameters. Lower reconstruction accuracy was achieved for unimodal distributions when the EA compartment was added.
5. Chapter 6: Improved model for the EA compartment. We show that a mixture of higher order tensors better describes the EA signal compared to other models.
6. Chapter 7: Joint model. The last chapter presents preliminary work on a joint model for both compartments, as well as perspectives and future work in order to apply the proposed methods to real tissue samples.

Relevant publications

The contributions presented in this thesis have been (or will be) shared publicly as follows (corresponding chapters are in parenthesis):

1. **David Romascano**, Jonathan Rafael-Patino, Ileana Jelescu, Muhamed Barakovic, Tim B. Dyrby, Jean-Philippe Thiran and Alessandro Daducci, "Voxel size matters: big voxels are required to generate realistic extra-axonal dMRI signals from Monte Carlo simulations", 26th annual meeting of the International Society for Magnetic Resonance in Medicine (ISMRM), Paris, France, June 16-21, 2018 (Chapter 3).
2. Jonathan Rafael-Patino, **David Romascano**, Alonso Ramirez-Manzanares, Gabriel Girard, Erick Jorge Canales-Rodríguez, Alessandro Daducci, Jean-Philippe Thiran, "Towards Realistic and Robust Monte Carlo Simulations for Diffusion MRI", to be resubmitted to NeuroImage (Chapter 3).
3. **David Romascano**, Muhamed Barakovic, Anna Auría, Tim B. Dyrby, Jean-Philippe Thiran and Alessandro Daducci, "Is it Feasible to Estimate Rotation-Invariant Non-Parametric Axon Diameter Distributions from PGSE? Preliminary Insights from Regularized Discrete Linear Modeling and Simulated Intra-Axonal Signals", ISMRM Workshop on breaking the barriers of Diffusion MRI, Lisbon, Portugal, September 11-16, 2016 (Chapter 4).

4. **David Romascano**, Muhamed Barakovic, Anna Auría, Tim B. Dyrby, Jean-Philippe Thiran and Alessandro Daducci, "Orientation invariant and non-parametric Axon Diameter Distribution mapping using PGSE and regularized discrete linear modeling", 25th annual meeting of the International Society for Magnetic Resonance in Medicine (ISMRM), Honolulu, USA, April 22-27, 2017 (Chapter 4).
5. **David Romascano**, Muhamed Barakovic, Jonathan Rafael-Patino, Tim B. Dyrby, Jean-Philippe Thiran, Alessandro Daducci, "ActiveAx_{ADD}: towards non-parametric and orientationally invariant axon diameter distribution mapping using PGSE", submitted to MRM on the 17th of September 2018 (Chapter 4).
6. **David Romascano**, Erick J. Canales-Rodriguez, Jonathan Rafael-Patino, Marco Pizzolato, Gaëtan Rensonnet, Muhamed Barakovic, Gabriel Girard, Alessandro Daducci, Tim B. Dyrby and Jean-Philippe Thiran, "HOTmix: Characterizing hindered compartments in diffusion MRI using a mixture of higher order tensors", in preparation (Chapter 6).

Other publications

During my PhD, I also contributed to other publications whose content is not addressed in the thesis:

Journal papers

- Kurt G. Schilling et al. "Limits to anatomical accuracy of diffusion tractography using modern approaches", *NeuroImage*, 2018, doi:10.1101/392571
- Erick J. Canales-Rodríguez, Jon Haitz Legarreta, MarcoPizzolato, Gaëtan Rensonnet, Gabriel Girard, Jonathan Rafael-Patino, Muhamed Barakovic, **David Romascano**, Yasser Alemán-Gómez, Joaquim Radua, Edith Pomarol-Clotet, Raymond Salvador, Jean-Philippe Thiran, and Alessandro Daducci, "Sparse wars: A survey and comparative study of spherical deconvolution algorithms for diffusion MRI", *NeuroImage*, 2018
- Aline M. Studerus-Germann, Oliver P. Gautschi, Pietro Bontempi, Jean-Philippe Thiran, Alessandro Daducci, **David Romascano**, Dieter von Ow, Gerhard Hildebrandt, Alexander von Hessling, and Doortje C.Engel, "Central nervous system microbleeds in the acute phase are associated with structural integrity by DTI one year after mild traumatic brain injury: A longitudinal study", *Neurologia i Neurochirurgia Polska*, 2018
- Klaus Maier-Hein et al., "The challenge of mapping the human connectome based on diffusion tractography", *Nature Communications*, 2017, 8:1349
- Gaetano Perrotta, Guillaume Bonnier, Djalel-Eddine Meskaldji, **David Romascano**, Ruslan Aydarkhanov, Alessandro Daducci, Samanta Simioni, Matthias Cavassini, Melanie Metral, François Lazeyras, Reto Meuli, Gunnar Krueger, Renaud Du Pasquier, and

Chapter 1. Introduction

Cristina Granziera, "Rivastigmine decreases brain damage in HIV patients with mild cognitive deficits", *Annals of Clinical and Translational Neurology*, 2017, 4(12):915-920

- Guillaume Bonnier, Alexis Roche, **David Romascano**, Samanta Simioni, Djalel-Eddine Meskaldji, David Rotzinger, Ying-Chia Lin, Gloria Menegaz, Myriam Schluep, Renaud Du Pasquier, Tilman Sumpf, Jens Frahm, Jean-Philippe Thiran, Gunnar Krueger, and Cristina Granziera, "Multicontrast MRI Quantification of Focal Inflammation and Degeneration in Multiple Sclerosis", *BioMed research international*, 2015
- Cristina Granziera, Alessandro Daducci, A. Donati, Guillaume Bonnier, **David Romascano**, Alexis Roche, Meribell Bach Cuadra, Daniel Schmitter, S. Klöppel, Reto Meuli, A. von Gunten, and Gunnar Krueger, "A Multi-Contrast MRI Study of Microstructural Brain Damage in Patients with Mild Cognitive Impairment", *NeuroImage: Clinical*, 2015
- **David Romascano**, Djalel-Eddine Meskaldji, Guillaume Bonnier, Samanta Simioni, David Rotzinger, Ying-Chia Lin, Gloria Menegaz, Alexis Roche, Myriam Schluep, Renaud Du Pasquier, Jonas Richiardi, Dimitri Van De Ville, Alessandro Daducci, Tilman Sumpf, Jens Frahm, Jean-Philippe Thiran, Gunnar Krüger, and Cristina Granziera, "Multicontrast connectometry: A new tool to assess cerebellum alterations in early relapsing-remitting multiple sclerosis", *Human Brain Mapping*, 2015, 36:1609-1619
- Djalel-Eddine Meskaldji, Lana Vasung, **David Romascano**, Jean-Philippe Thiran, Patric Hagmann, Stephan Morgenthaler, and Dimitri Van De Ville, "Improved statistical evaluation of group differences in connectomes by screening-filtering strategy with application to study maturation of brain connections between childhood and adolescence", *NeuroImage*, 2015, 108:251-264

Conferences

- Jonathan Rafael-Patino, **David Romascano**, Gabriel Girard, Gaetan Rensonnet, Jean-Philippe Thiran, and Alessandro Daducci, "Realistic 3D Fiber Crossing Phantom Models for Monte Carlo Diffusion Simulations", 26th annual meeting of the International Society for Magnetic Resonance in Medicine (ISMRM), Paris, France, June 16-21, 2018
- Muhamed Barakovic, Gabriel Girard, **David Romascano**, Jonathan Rafael-Patino, Maxime Descoteaux, Giorgio Innocenti, Derek Jones, Jean-Philippe Thiran, and Alessandro Daducci, "Assessing feasibility and reproducibility of a bundle-specific framework on in vivo axon diameter estimates at 300mT/m", 26th annual meeting of the International Society for Magnetic Resonance in Medicine (ISMRM), Paris, France, June 16-21, 2018
- Elda Fischì Gomez, Guillaume Bonnier, Pavel Falkowskiy, **David Romascano**, Myriam Schluep, Renaud Du Pasquier, Alessandro Daducci, Jean-Philippe Thiran, Gunnar Krueger, and Cristina Granziera, "A Longitudinal Study of Neurite Orientation Dispersion and Density Imaging in Relapsing-Remitting Multiple Sclerosis", 25th annual meeting

of the International Society for Magnetic Resonance in Medicine (ISMRM), Honolulu, USA, April 22-27, 2017

- Muhamed Barakovic, **David Romascano**, Gabriel Girard, Maxime Descoteaux, Jean-Philippe Thiran, and Alessandro Daducci, "In-vivo Bundle-Specific Axon Diameter Distributions Estimation across the Corpus Callosum", 25th annual meeting of the International Society for Magnetic Resonance in Medicine (ISMRM), Honolulu, USA, April 22-27, 2017
- Muhamed Barakovic, **David Romascano**, Gabriel Girard, Maxime Descoteaux, Jean-Philippe Thiran, and Alessandro Daducci, "When does a volume of a bundle achieve saturation? A microstructure informed tractography study", 25th annual meeting of the International Society for Magnetic Resonance in Medicine (ISMRM), Honolulu, USA, April 22-27, 2017
- Muhamed Barakovic, **David Romascano**, Tim B. Dyrby, Daniel C. Alexander, Jean-Philippe Thiran, and Alessandro Daducci, "Assessment of bundle-specific axon diameter distributions using diffusion MRI tractography", 22nd Annual Meeting of the Organization for Human Brain Mapping, Geneva, Switzerland, June 26-30, 2016
- Anna Auría, **David Romascano**, Erick J. Canales-Rodriguez, Tim B. Dyrby, Daniel C. Alexander, Jean-Philippe Thiran, Yves Wiaux, and Alessandro Daducci, "Reducing acquisition time for microstructure imaging with spatially-regularized global optimization", 22nd Annual Meeting of the Organization for Human Brain Mapping, Geneva, Switzerland, June 26-30, 2016
- Anna Auría, **David Romascano**, Erick J. Canales-Rodriguez, Tim B. Dyrby, Daniel C. Alexander, Jean-Philippe Thiran, Yves Wiaux, and Alessandro Daducci, "Reducing acquisition time for axon diameter mapping using global optimization in the spatial-angular-microstructure space", 24th annual meeting of the International Society for Magnetic Resonance in Medicine (ISMRM), Singapore, Singapore, May 7-13, 2016
- Anna Auría, **David Romascano**, Erick J. Canales-Rodriguez, Yves Wiaux, Tim B. Dyrby, Daniel C. Alexander, Jean-Philippe Thiran, and Alessandro Daducci, "Accelerated Microstructure Imaging via Convex Optimisation for regions with multiple fibres (AMICOx)", IEEE International Conference on Image Processing 2015, Quebec City, Quebec, Canada, September, 27-30, 2015
- **David Romascano**, Alessandro Dal Palú, Jean-Philippe Thiran, and Alessandro Daducci, "On evaluating the accuracy and biological plausibility of diffusion MRI tractograms", 23rd annual meeting of the International Society for Magnetic Resonance in Medicine (ISMRM), Toronto, Canada, 30 May-June 05, 2015

2 Theory and State-of-the-art

2.1 White matter

The brain is the most complex organ in the human body. It is composed of two main tissues: the grey matter (GM) which contains neuron's cell bodies and their billions of synapses, and the white matter (WM) which contains the neuron's axons that relay the signals between the different GM regions (Figure 2.1).

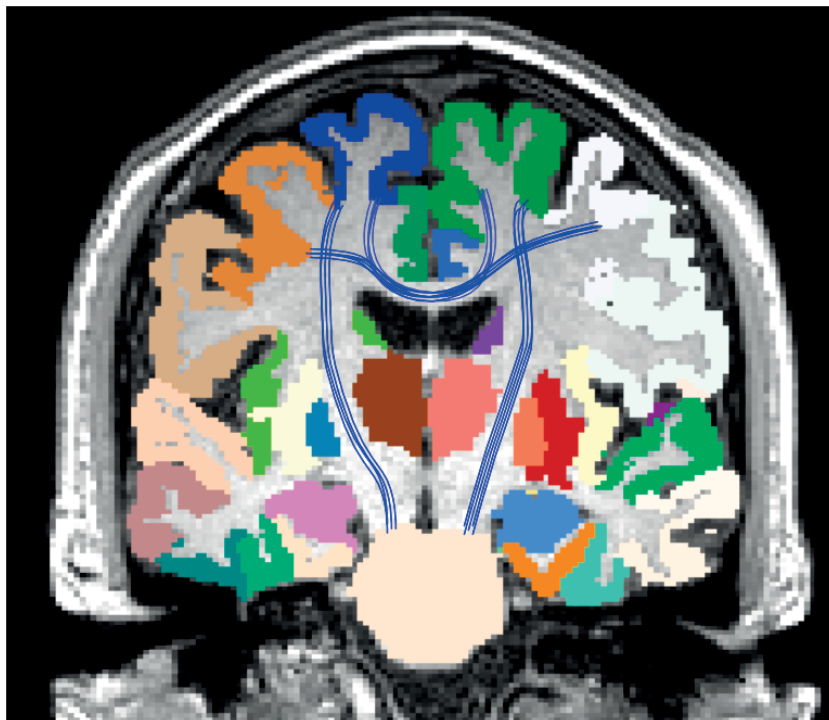


Figure 2.1 – Schematic of the brain's organization. Different GM regions are labeled in color. Some fascicles are illustrated with blue lines, going through the WM.

Neurons in the central nervous system take input signals from other neurons through their dendrites (Figure 2.2). Multiple excitatory or inhibitory inputs are transmitted to the body (or soma) where they are combined to eventually trigger an action potential at the base of the axon. The axonal membrane depolarizes, opening ion channels further away along the axon, propagating the action potential until the axon terminal. Signal transmission along axons is influenced by several microstructural properties like the internal axon diameter [92, 98] or the membrane permeability. Some neurons are myelinated by oligodendrocytes, accelerating signal transmission depending on myelin thickness and distance between Ranvier nodes. The integrity of WM microstructural properties therefore ensures the proper performance of the brain.

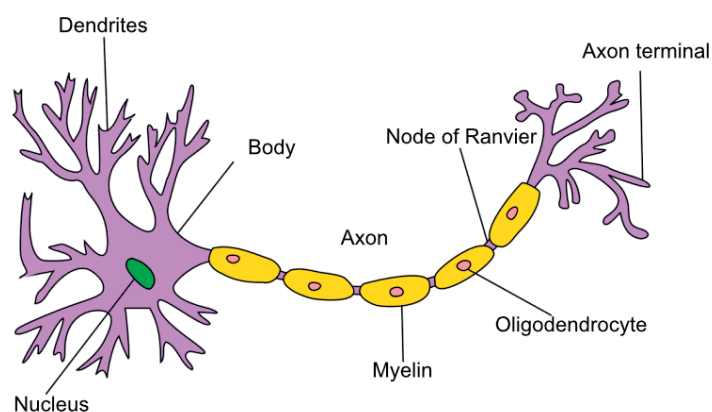


Figure 2.2 – Axon structure. Modified from Quasar Jarosz's illustration for Wikipedia (<https://en.wikipedia.org/wiki/Neuron>). CC BY-SA 3.0

It appears that WM fascicles are composed by axons with different diameters (Figure 2.3) [59, 1]. A broad spectrum of neurological disorders is linked to alterations of the WM tissue microstructure, disrupting or altering communication between brain regions and leading to various neurological and/or motor symptoms. In particular, the Axon Diameter Distribution (ADD) has been shown to change during normal development [23], but also during pathological events involving axonal degeneration and/or injury, like multiple sclerosis [94, 65, 34, 28], amyotrophic lateral sclerosis [21, 61], alzheimer [9], traumatic brain injury [29], or stroke [17]. Changes in the ADD have also been reported in psychiatric diseases like autism [78, 48], dyslexia [71], and schizophrenia [82, 84].

Characterizing WM tissue microstructure can thus help researchers and medical doctors to better understand and diagnose such diseases, as well as monitoring and adapting therapy to improve patient outcome.

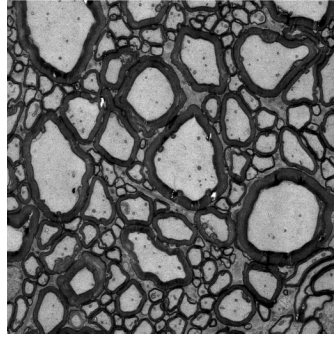


Figure 2.3 – EM section of axons showing the distribution of axon diameters. Image kindly provided by Professor Innocenti.

2.2 Diffusion weighted imaging (DWI)

Diffusion weighted Imaging (DWI) or dMRI provides a unique way to probe WM organization non-invasively. Indeed, the dMRI contrast is sensitive to water diffusion due to thermal motion (*i.e.* Brownian motion), and can be measured along a given direction using an MRI scanner. This is achieved using the well known Pulsed Gradient Spin Echo (PGSE) sequence [89], whose diagram is shown in Figure 2.4 The radio frequency (RF) pulses have the same effect as for a

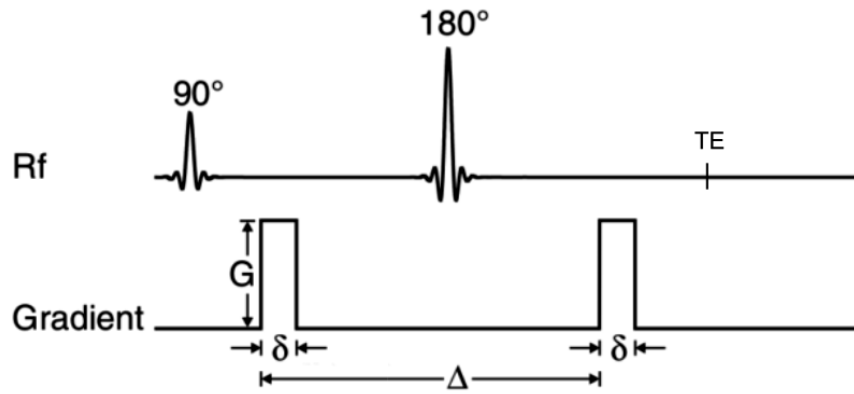


Figure 2.4 – PGSE protocol showing the gradient amplitude G , duration δ and separation Δ . Modified from [54]

standard spin echo sequence, where the measured signal S_0 corresponds to

$$S_0 = M_0(1 - e^{-\frac{TR}{T_1}})e^{-\frac{TE}{T_2}}. \quad (2.1)$$

M_0 is the initial magnetization or proton density, T_1 and T_2 are the longitudinal and transverse relaxation times, and TR and TE are the repetition time and echo time, respectively.

The PGSE sequence includes two diffusion gradients of amplitude G , duration δ and separation Δ , applied in a direction \mathbf{g} . The first gradient adds a phase to the spins. If the spins do not move during the time Δ , the additional phases get cancelled by the second gradient, and the measured signal is the same as obtained with a standard spin echo sequence. If the spins do move along the direction of the diffusion gradient, then the measured signal S has a decreased amplitude compared to the spin-echo signal S_0 . The decrease in amplitude depends on how far spins move on average and on the gradient's amplitude, duration and separation.

Water molecules are always moving randomly (*i.e.* diffusing) due to thermal energy. In the case of free diffusion, Einstein [33] showed that the averaged squared displacement of an ensemble of spins between two time points can be described using the following equation:

$$\langle d^2 \rangle = 6Dt, \quad (2.2)$$

where d is the displacement of a spin during time t , and D is the sample's *diffusivity*. In standard units, diffusivity is expressed in m^2/s . In the case of free diffusion, and by summarizing the sequence parameters into the so-called b-value $b = (\gamma G \delta)^2 (\Delta - \delta/3)$ [89], the measured signal can be expressed as:

$$\frac{S}{S_0} = e^{-bD}. \quad (2.3)$$

The apparent diffusion coefficient (ADC) along a given direction can thus be estimated by applying the diffusion gradients in said direction, and solving for $\text{ADC} = \frac{-\log(S/S_0)}{b}$. For free diffusion, the ADC is the same in any direction, and the ADC profile is said to be isotropic.

2.3 Microstructure imaging

Cell membranes hinder and restrict the motion of water molecules located between and within cells. Deviation from free diffusion therefore provides information on the local microenvironment sampled by water molecules during the diffusion time. The ADC *per se* was shown to be useful for the early detection of ischemic stroke [67]. The ADC decreases immediately in regions affected by an ischemic stroke. The explanation for the decrease in MD is thought to be mainly linked to cell swelling, and might be related to lower intracellular diffusion, but also to alteration of diffusion properties in the extra-cellular space [16, 19, 26, 43, 44, 95]. The main contribution of DWI has been the early diagnostic of ischemic stroke, which accelerates the initiation of necessary health-care procedures that are required for a better prognosis for the patient [39].

Microstructure imaging aims at extracting useful information about the tissue microstructure using the dMRI signal [3]. Not any information can be extracted though, as the dMRI sensitivity to specific microstructural features depends on the parameters of the PGSE sequence (namely gradient amplitude G , duration δ and separation Δ) and the models used for the reconstruction.

Models can be separated into two categories: signal models and compartment models.

2.3.1 Signal models

Five different signal models are presented hereafter: the Diffusion Tensor model (DT) [11] that represents the signal assuming gaussian diffusion, and the Higher Order Tensor (HOT) [64] and Diffusion Kurtosis (DK) [52] models which are used to characterize non-gaussian diffusion.

Diffusion Tensor

WM being composed of axons, spins trajectories are interfered preferentially along the perpendicular direction. The ADC profile is said to be anisotropic, with spins moving a longer distance along the axons, and less in the direction perpendicular to them. A set of dMRI signals can be acquired with the same b-value over different directions, forming what is referred to as a "shell". The b-value can also be expressed as a 2nd-order tensor (*i.e.* a 3×3 matrix) $b^{(2)}$:

$$b^{(2)} = \begin{bmatrix} b_{11}^{(2)} & b_{12}^{(2)} & b_{13}^{(2)} \\ b_{21}^{(2)} & b_{22}^{(2)} & b_{23}^{(2)} \\ b_{31}^{(2)} & b_{32}^{(2)} & b_{33}^{(2)} \end{bmatrix} \quad (2.4)$$

where $b_{i_1 i_2}^{(2)} = (\gamma \delta)^2 g_{i_1} g_{i_2} (\Delta - \delta/3)$. Here, the subscripts represent the dimensions of the frame of reference (*i.e.* 1, 2 and 3 represent the 1st, 2nd and 3rd component of a 3D vector), such that a diffusion gradient has a magnitude G that depends on the gradient components g_1 , g_2 and g_3 according to $G = \| [g_1, g_2, g_3]^T \|_2$ for a PGSE protocol. As $b_{i_1 i_2}^{(2)} = b_{i_2 i_1}^{(2)}$, $b^{(2)}$ can be summarized to a 6-element vector for each PGSE sample. Concatenating the $b^{(2)}$ for all measurements in a diffusion protocol is referred to as the b-matrix [57].

Assuming Gaussian diffusion and the presence of a single main fiber orientation allows expressing the dMRI signal as a second order DT [11]. In Diffusion Tensor Imaging (DTI), the signal is approximated by a 2nd order tensor in 3 dimensions, given by the following expression:

$$\log\left(\frac{S}{S_0}\right) = -b_{i_1 i_2}^{(2)} D_{i_1 i_2}^{(2)}, \quad (2.5)$$

following Einstein's summation rule and using the b-matrix elements $b_{i_1 i_2}$. By exploiting the symmetries of the tensor (*e.g.* $D_{12}^{(2)} = D_{21}^{(2)}$ and $b_{12}^{(2)} = b_{21}^{(2)}$), the summation simplifies to

$$\log\left(\frac{S}{S_0}\right) = -b_{11}^{(2)} D_{11}^{(2)} - 2b_{12}^{(2)} D_{12}^{(2)} - 2b_{13}^{(2)} D_{13}^{(2)} - b_{22}^{(2)} D_{22}^{(2)} - 2b_{23}^{(2)} D_{23}^{(2)} - b_{33}^{(2)} D_{33}^{(2)}. \quad (2.6)$$

The 6 variables $D_{i_1 i_2}^{(2)}$ can therefore be solved by acquiring $N \geq 6$ dMRI samples in 6 or more non collinear directions. If $Y \in \mathbb{R}^{N \times 1}$ is the log-transformed normalized signal, $B \in \mathbb{R}^{N \times 6}$ is the b-matrix, and D is the linearized 6-elements of $D^{(2)}$, then the signal is equal to $Y = BD$ and D

can be reconstructed by solving the equation using ordinary least-squares:

$$D = (B^T B)^{-1} B^T Y. \quad (2.7)$$

The reconstructed tensor $D^{(2)}$ can be used to extract properties which characterize the underlying tissue. For example, it's first eigenvector can be thought to provide the main orientation of the axons in the voxel; it's first eigenvalue to provide the ADC along the axons; the mean of the second and third eigenvalues to provide the ADC perpendicular to the axons; it's normalized trace (mean of all eigenvalues) to provide the bulk ADC, discarding orientation information; the Fractional Anisotropy (FA) [12] combines the bulk ADC $\langle \lambda \rangle$ with the eigenvalues λ_i into the following expression

$$FA = \sqrt{\frac{3}{2} \frac{\sqrt{\sum_{i=1}^3 (\lambda_i - \langle \lambda \rangle)^2}}{\sqrt{\sum_{i=1}^3 \lambda_i}}}, \quad (2.8)$$

to provide the degree of anisotropy, ranging from 0 (completely isotropic) to 1 (completely anisotropic).

The main pitfall of DTI is that it assumes that the diffusion process in the brain is gaussian. Diffusion in the brain is never gaussian, but it can be approximated as such for low b-values.

Higher Order Tensors

At higher b-values, non-gaussianity cannot be ignored. To cope with non-gaussian diffusion, higher order tensors can be used, as proposed by Liu [64]. The complex dMRI signal is expressed as a truncated series of Higher Order Tensors (HOT):

$$\ln\left(\frac{S}{S_0}\right) = -b_{i_1 i_2}^{(2)} D_{i_1 i_2}^{(2)} + b_{i_1 i_2 i_3 i_4}^{(4)} D_{i_1 i_2 i_3 i_4}^{(4)} - \dots + (-1)^n b_{i_1 i_2 \dots i_{2n}}^{(2n)} D_{i_1 i_2 \dots i_{2n}}^{(2n)} + j(-b_{i_1 i_2 i_3}^{(3)} D_{i_1 i_2 i_3}^{(3)} + b_{i_1 i_2 i_3 i_4 i_5}^{(5)} D_{i_1 i_2 i_3 i_4 i_5}^{(5)} - \dots + (-1)^n b_{i_1 i_2 \dots i_{2n+1}}^{(2n+1)} D_{i_1 i_2 \dots i_{2n+1}}^{(2n+1)}), \quad (2.9)$$

where $j = \sqrt{-1} \in \mathbb{C}$. Exploiting the symmetries of the tensors, and expressing the previous equation as a linear system, the signal's real component can be expressed as $\mathbf{Y}_r = \mathbf{B}_r \mathbf{X}_r$, where:

$$\mathbf{Y}_r = [\text{real}(\ln(S_1/S_0)), \text{real}(\ln(S_2/S_0)), \dots, \text{real}(\ln(S_m/S_0))]^T \quad (2.10)$$

$$\mathbf{X}_r = [D_{11}^{(2)}, D_{12}^{(2)}, \dots, D_{33}^{(2)}, D_{1111}^{(4)}, D_{1112}^{(4)}, \dots, D_{3333}^{(4)}, \dots]^T \quad (2.11)$$

$$\mathbf{B}_r = \begin{bmatrix} -b_{11}^{(2),1} & -2b_{12}^{(2),1} & \dots & -b_{33}^{(2),1} & b_{1111}^{(4),1} & 4b_{1112}^{(4),1} & \dots & b_{3333}^{(4),1} & \dots \\ -b_{11}^{(2),2} & -2b_{12}^{(2),2} & \dots & -b_{33}^{(2),2} & b_{1111}^{(4),2} & 4b_{1112}^{(4),2} & \dots & b_{3333}^{(4),2} & \dots \\ \dots & \dots & \dots & \dots & \dots & \dots & \dots & \dots & \dots \\ -b_{11}^{(2),m} & -2b_{12}^{(2),m} & \dots & -b_{33}^{(2),m} & b_{1111}^{(4),m} & 4b_{1112}^{(4),m} & \dots & b_{3333}^{(4),m} & \dots \end{bmatrix}, \quad (2.12)$$

where m samples of the signal S have been acquired using different gradient directions and

strengths. Here, the b-matrix elements are given by:

$$b_{i_1 i_2 \dots i_n}^{(n)} = (\gamma\delta)^n g_{i_1} g_{i_2} \dots g_{i_n} (\Delta - \frac{n-1}{n+1}\delta). \quad (2.13)$$

Using a similar expression for the imaginary part of the signal, Liu et al. [64] showed that the signals from various closed pores could be reconstructed, along with their spins' Probability Density Function (PDF). The pore shapes included an isotropic sphere, a single tube, a crossing of tubes and a Y-shaped tube.

Diffusion Kurtosis

Non-gaussian diffusion can also be characterized by measuring the kurtosis tensor (KT) [52]. In Diffusion Kurtosis Imaging (DKI), the dMRI signal is expressed as:

$$\ln\left(\frac{S}{S_0}\right) = -bD_{\text{app}} + \frac{1}{6}b^2 D_{\text{app}}^2 K_{\text{app}} + \mathcal{O}(b^3), \quad (2.14)$$

where b is here the 2nd-order b-value $b = b^{(2)} = (\gamma G\delta)^2(\Delta - \delta/3)$. Similarly to the DT and HOT, kurtosis can be anisotropic and its 3D profile estimated by reconstructing the kurtosis tensor $W_{i_1 i_2 i_3 i_4}$:

$$\ln\left(\frac{S}{S_0}\right) = -b_{i_1 i_2}^{(2)} D_{i_1 i_2}^{(2)} + \frac{1}{6}(b_{i_1 i_2}^{(2)})^2 \left(\frac{1}{3}\text{tr}(D_{i_1 i_2}^{(2)})\right) W_{i_1 i_2 i_3 i_4}. \quad (2.15)$$

2.3.2 Statistical models

Statistical models assume that the perpendicular signal arises from a distribution of diffusivities, motivated by the assumption that different spin "packets" will sense different local micro-environments during the diffusion experiment. In general, the diffusion signal is assumed to be given by the following equation:

$$\frac{S_{\perp}}{S_0} = \int P(D_{\perp}^{(2)}) e^{-b^{(2)} D_{\perp}^{(2)}} dD_{\perp}^{(2)}, \quad (2.16)$$

where $b^{(2)}$ and $D_{\perp}^{(2)}$ are the 2nd-order b-value and perpendicular diffusivity, and $P(D_{\perp}^{(2)})$ is the distribution of perpendicular diffusivities in the voxel of interest. Yablonskiy et al. [100] proposed to model the distribution as a gaussian distribution, deriving a general expression for a truncated gaussian in case of high variance with respect to the mean, as well as a simplified expression in the case of a narrow distribution. Scherrer et al. [86] extended the expression to a distribution of diffusion tensors:

$$\frac{S}{S_0} = \int_{D^{(2)} \in \text{Sym}^+(3)} P(D^{(2)}) e^{-b^{(2)} D^{(2)}} dD^{(2)}, \quad (2.17)$$

where $D^{(2)} \in \text{Sym}^+(3)$ are symmetric positive-definite 2nd-order tensors. The authors further derive the expression for a distribution consisting of a mixture of populations, each following a

matrix-variate Gamma distribution [86]. The model was shown to efficiently capture mixtures of restricted, hindered and isotropic diffusion, providing information on the heterogeneity of diffusion coefficients present in each population. The model was coined DIAMOND, standing for DIstribution of 3D Anisotropic MicrOstructural eNvironments in Diffusion-compartment imaging.

In overall, the signal and statistical models presented earlier do not provide metrics that are specific enough on their own, as many tissue features can influence them similarly (*e.g.* fiber crossings, exchange, dispersion, axonal loss, demyelination, etc...). Higher specificity can be achieved by using compartment models. Specific microstructure properties include features like the mean axon diameter [4], or axon diameter distributions [6, 15], as well as intra-axonal and extra-axonal volume fractions or neurite dispersion [102].

2.3.3 Compartment models

WM is usually considered to be made of infinite impermeable cylinders [3]. Under such assumption, the WM dMRI signal can thus be decomposed into two compartments. On one hand, the Intra Axonal (IA) compartment represents the signal from water molecules trapped inside the axons and whose trajectory is *restricted* by axonal membranes. On the other hand, the Extra Axonal (EA) compartment represents the signal from water molecules that are moving in the space between axons, and whose trajectory is *hindered* by the axonal membranes.

The WM tissue signal \mathbf{y} is therefore expressed as a mixture of compartments, using the following equation:

$$\mathbf{y} = \sum f_i \mathbf{y}_i \text{ s.t. } \sum f_i = 1, \quad (2.18)$$

where f_i are the compartment volume fractions and \mathbf{y}_i are the normalized compartment signals. Compartment models usually include a free-water component signal \mathbf{y}_{free} , featuring isotropic diffusion and therefore modeled as a perfect sphere, a restricted signal \mathbf{y}_r and a hindered signal \mathbf{y}_h whose formulations depend on the tissue model. Different compartment models are presented hereafter.

CHARMED

The Composite Hindered And Restricted Model of Diffusion (CHARMED) was proposed by Assaf et al. [7] in 2004. The model consists of a mixture of M hindered and N restricted compartments:

$$E(q, \Delta) = \sum_{i=1}^M f_h^i E_h^i(q, \Delta) + \sum_{j=1}^N f_r^j E_r^j(q, \Delta) \quad (2.19)$$

where f_h^i and f_r^j are the signal volume fractions of the hindered and restricted compartments;

$E_h^i(q, \Delta)$ is the signal of the hindered compartment, given by an axi-symmetric DT; and $E_r^j(q, \Delta)$ is the signal of the restricted compartment, given by the signal of a cylinder with radius R (fixed to typical values in the spinal cord) as derived by Neuman [68]. The q -value is given by $q = \frac{1}{2\pi} \gamma \delta g$, with γ the gyromagnetic ratio and g the gradient amplitude. Having several restricted compartments allows the model to handle fiber crossings, as shown experimentally by the authors [7, 5]. The model uses a fixed expression for the diameter of the cylinder(s).

AxCaliber

The AxCaliber model aims at estimating the distribution of axon diameters, and was proposed by Assaf et al. in 2008 [6]. It simplifies the WM structure to a single population, and therefore expresses the diffusion signal as one restricted and one hindered compartment:

$$E(q, \Delta) = f_h E_h(q, \Delta) + f_r E_r(q, \Delta). \quad (2.20)$$

The hindered compartment remains modeled by an axi-symmetric DT, as for the CHARMED model. The restricted compartment on the other hand is now modeled a set of parallel cylinders with radii sampled from a gamma distribution. The parameters of the model are the two parameters of the gamma distribution (α and β), the perpendicular diffusivity in the hindered compartment, and the compartment volume fractions, which are obtained through a non-linear least-squares (LS) routine using Levenberg–Marquardt minimization. AxCaliber analysis was initially based on NMR diffusion data with fixed gradient duration $\delta = 2.5$ ms, 5 different diffusion times $\Delta = [10, 15, 20, 30, 40, 50, 60, \text{ and } 80]$ ms and 16 gradient strengths per diffusion time ($G_{\max} = 1200$ mT/m) [6]. In vivo measurements were subsequently performed with a protocol using a fixed gradient duration of $\delta = 3.2$ ms, 5 diffusion times $\Delta = [11, 20, 30, 60, \text{ and } 100]$ ms and 16 gradient strenghts varying between 0 and 282mT/m [10]. The AxCaliber model assumes diffusion gradients to be applied perpendicularly to the axons' main axis, which limits the method to samples with known orientation prior to scanning.

ActiveAx

The ActiveAx framework proposed by Alexander et al. in 2010 [4] includes a tissue model and an optimization framework to design ad-hoc PGSE protocols for mean diameter estimation [2]. The optimization framework can be adapted to provide protocols for either in vivo or ex vivo dMRI data [2]. The WM tissue model is coined the minimal model for white matter diffusion (MMWMD), as it describes the restricted signal as a perfectly parallel cylinder of radius a' and the hindered compartment as an axi-symmetric tensor. As dMRI is sensitive to the volume of spins sampling a given microstructural environment, the radius a' is coined the mean volume weighted diameter, or diameter index [4]. It is related to the distribution of radii by $a' = \sum r_i^3 / \sum r_i^2$ [4], although more recent work relate then by $a'^2 \approx \langle r^4 \rangle / \langle r^2 \rangle$ for PGSE protocols with short gradient duration and $a'^4 \approx \langle r^6 \rangle / \langle r^2 \rangle$ for long gradient durations [18]. The parameters of the hindered signal are coupled to the intra-cellular volume fraction using the tortuosity model proposed by [90] to reduce the degrees of freedom. The model parameters include the diameter index a' and the compartment volume fractions, which are estimated using a non-linear optimization coupled to a Markov Chain Monte

Carlo (MCMC) procedure. The posterior distribution of the estimated parameters can be plotted, showing their confidence level. The mean diameter index is however a limited information compared to the whole ADD.

NODDI

The neurite orientation dispersion and density imaging (NODDI) model does not suppose that the restricted signal comes from perfectly parallel cylinders. It introduces a parameter for dispersion, and discards the information regarding axonal diameter for the problem to remain tractable [102]. The restricted signal is thus modeled as a set of dispersed sticks (cylinders of zero radius) and the hindered compartment as a dispersed axi-symmetric tensor. The parameters to estimate are the compartment volume fractions and the dispersion, which are obtained through a Gauss-Newton non-linear optimization. The NODDI model is such that a protocol can be optimized to provide the dMRI signal required to extract the information of interest, using clinical scanners.

Such methods have revealed promising pre-clinical and clinical applications, although their reconstruction requires long computation time and computational power [25].

2.4 Inverse problems

As mentioned above, microstructure imaging methods are based on non-linear optimization algorithms, and are thus subject to some pitfalls, like local minima, long computation time and computational power [25].

2.4.1 Microstructure imaging as an inverse problem

Efficient microstructure estimation can be achieved by linearizing the microstructure problem. A framework called AMICO (Accelerated Microstructure Imaging using Convex Optimization) was proposed by Daducci et al. [25], in which WM microstructure problems can be reformulated as a discrete linear inverse problem, solvable using dedicated solvers that yields a global solution thousands of times faster than conventional non-linear methods [25]. The dMRI signal \mathbf{y} is formulated using the following linear equation:

$$\mathbf{y} = \mathbf{D}\mathbf{x} + \boldsymbol{\eta}, \quad (2.21)$$

in which \mathbf{D} is a matrix encoding the forward model (e.g. MMWMD, NODDI, etc...) that depends on the microstructure model, \mathbf{x} are the volume fractions to be estimated for each of the atoms (i.e. columns of the matrix) present in \mathbf{D} and $\boldsymbol{\epsilon}$ represents the noise in the dMRI signal. The matrix \mathbf{D} is also called a convolution operator or a dictionary. A unique and global solution can be obtained by solving the following convex problem:

$$\underset{\mathbf{x} \geq 0}{\operatorname{argmin}} \|\mathbf{D}\mathbf{x} - \mathbf{y}\|_2^2 + \lambda \mathcal{F}_r(\mathbf{x}), \quad (2.22)$$

in which $\mathcal{F}_r(\cdot)$ regularizes the solution \mathbf{x} and depends on the tissue model. AMICO was first used to linearize the ActiveAx [4] and NODDI [102] models.

2.4.2 ActiveAx_{AMICO}

Following the ActiveAx model [4], the dictionary \mathbf{D} is split into a set of N_r atoms modeling the restricted compartment \mathbf{D}_r , a set of N_h atoms to model the hindered compartment \mathbf{D}_h and an isotropic atom \mathbf{D}_{ISO} such that: $\mathbf{D} = [\mathbf{D}_r, \mathbf{D}_h, \mathbf{D}_{ISO}]$. The N_r restricted dMRI signals are computed using the forward model for the parallel cylinders derived by [96], using a set of N_r radii R_i equally spaced between $0.5 \mu\text{m}$ and $10 \mu\text{m}$. The N_h hindered dMRI signals are computed using the zeppelin analytical model, which corresponds to an axi-symmetric tensor with perpendicular diffusivity expressed as a function of the axonal density as in [4, 77], with densities varying between 0.3 and 0.9. In the case of the ActiveAx model [4], the regularizer $\mathcal{F}_r(\cdot)$ is set as a simple Tikhonov regularization $\mathcal{F}_r(\mathbf{x}) = \|\mathbf{x}\|_2^2$. The objective function (2.22) to linearize the ActiveAx model is then:

$$\underset{\mathbf{x} \geq \mathbf{0}}{\operatorname{argmin}} \|\mathbf{D}\mathbf{x} - \mathbf{y}\|_2^2 + \lambda \|\mathbf{x}\|_2^2. \quad (2.23)$$

As each atom corresponds to a given diameter or perpendicular diffusivity, tissue microstructural features can be recovered from the solution \mathbf{x} . The intra-axonal volume fraction corresponds to the sum of the cylinders' weights: $icvf = \sum_{i=1}^{N_r} x_i$. The mean diameter index a' [4] can be recovered using the cylinders radii R_i and the following expression:

$$a' = \frac{\sum_{i=1}^{N_r} 2R_i x_i}{\sum_{i=1}^{N_r} x_i}. \quad (2.24)$$

2.4.3 NODDI_{AMICO}

In the case of the NODDI model [102], the axons are not considered as necessarily perfectly parallel anymore. To solve the problem using the linear inverse formulation (2.22), the dictionary \mathbf{D} is split into anisotropic and isotropic compartments. The anisotropic compartment is made of atoms representing every combination of dispersion and axon packing densities, as derived from the NODDI model [102]. The isotropic compartment \mathbf{D}_{ISO} is the same as for the ActiveAx model. As a single combination of dispersion and axonal packing density is expected to model the dMRI signal, the regularization is set to impose the elastic-net penalty: $\mathcal{F}_r = \lambda_1 \|\mathbf{x}\|_2^2 + \lambda_2 \|\mathbf{x}\|_1$. The objective function (2.22) to linearize the NODDI model then becomes:

$$\underset{\mathbf{x} \geq \mathbf{0}}{\operatorname{argmin}} \|\mathbf{D}\mathbf{x} - \mathbf{y}\|_2^2 + \lambda_1 \|\mathbf{x}\|_2^2 + \lambda_2 \|\mathbf{x}\|_1. \quad (2.25)$$

As for the ActiveAx model, tissue microstructural features can be extracted from the solution \mathbf{x} . The AMICO framework proved to yield microstructure estimates close to the original implementations and several orders of magnitude faster [25].

2.4.4 Non-parametric ADD estimation

In ADD estimation, axons are usually modeled as impermeable cylinders [6, 4, 15, 3]. The WM dMRI signal S is expressed as a weighted contribution of IA and EA dMRI signals [7]:

$$S = S_0 * [f_{IA} S_{IA} + (1 - f_{IA}) S_{EA}] + \epsilon. \quad (2.26)$$

The IA dMRI signal $f_{IA} S_{IA}$ can further be considered as the weighted contribution of the water within a set of N_d cylinders with different radii:

$$f_{IA} S_{IA} = \sum_{d=1}^{N_d} w_d S_{cyl}(R_d, D^{\parallel}, \Omega), \quad (2.27)$$

where w_d are the volume fractions of each cylinder, and S_{cyl} is the dMRI signal for a cylinder with radius R_d , parallel diffusivity D^{\parallel} and dMRI protocol parameters Ω [96]. Clustering the cylinders into N_A bins gives:

$$f_{IA} S_{IA} = \sum_{\text{bin}=1}^{N_A} \Psi_{\text{bin}} S_{cyl}(R_{\text{bin}}, D^{\parallel}, \Omega), \quad (2.28)$$

where Ψ_{bin} is the volume fraction occupied by cylinders belonging to each bin, and R_{bin} is the characteristic radius of the bin (taken to be the center of the bin).

In Eq. 2.28, the coefficients Ψ are analytically related to the ADD and a direct mapping between the two is possible [15]. An important aspect of ADD mapping is that the formulation presented previously reconstructs the volume weighted ADD, similarly to the relationship between the mean diameter index and the distribution of radii presented by Alexander et al. for the MMWMD [4]. If the number weighted ADD represents the relative number of cylinders with diameter within a given range (i.e. the normalized diameter histogram), then the coefficients Ψ represent the volume fraction occupied by those same cylinders, with respect to the total IA volume. Benjamini et al. nicely illustrate the concept in Figure 2.5.

In this schematic illustration, the distribution is made of 15 axons with diameter of $1 \mu\text{m}$, 4 axons with diameter of $4 \mu\text{m}$ and 1 axon with diameter of $7 \mu\text{m}$. If the ADD is assumed to be discretized with 3 bins with ranges 0-2.5, 2.5-5 and 5-7.5 μm . The number weighted ADD is therefore $\Psi = [0.75, 0.2, 0.05]$. The volume weighted ADD on the other hand is given by $[0.12, 0.50, 0.38]$. As mentioned by Benjamini et al. [15], a mapping between the volume weighted ADD $\Psi(a)$ and number weighted ADD is possible by dividing the values of $\Psi(a)$ by the diameter squared of the respective bin, and then normalizing the distribution such that it sums up to 1. All mentions of the ADD in the rest of this article will be referring to the

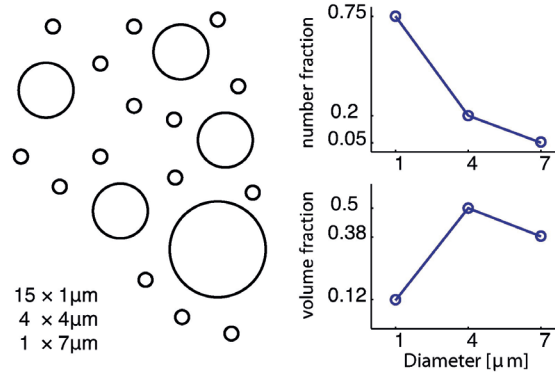


Figure 2.5 – Number weighted and volume weighted ADD. Reprinted from [15], Copyright 2016, with permission from Elsevier Inc.

coefficients Ψ (ie: the volume weighted ADD).

Similarly to ActiveAx_{AMICO}, Eqs. 2.26 and 2.28 can be combined and reformulated as a linear inverse-problem [15, 25, 45]:

$$y = Dx + \epsilon, \quad (2.29)$$

where D is a dictionary encoding the IA and EA signal using a mixture of cylinders and zeppelins, as done for ActiveAx_{AMICO}.

As the problem is ill-posed, the solution vector x can be estimated by minimizing the following penalty function:

$$\operatorname{argmin}_{x \geq 0} \|Dx - y\|_2^2 + \lambda \|\Gamma x\|_2^2, \quad (2.30)$$

where the role of the regularization term $\lambda \|\Gamma x\|_2^2$ is to stabilize the solution. Using a matrix D as described previously, x is a vector that contains the estimated volume fractions of each column, and can be split as $x = [x_{IA} | x_{EA}]$. The normalized IA coefficients $\frac{x_{IA}}{\sum x_{IA}}$ therefore correspond to the estimated ADD. The estimated mean diameter index a' can be extracted from the vector x as in [25]:

$$a' = \frac{\sum_{i=1}^{N_A} 2R_i x_i}{\sum_{i=1}^{N_A} x_i} \quad (2.31)$$

where R_i is the radius corresponding to the i -th column of D . The estimated IA and EA volume fractions (IAVF and EAVF) can be computed as the sum of each compartment's coefficients, divided by the sum of all coefficients:

$$\text{IAVF} = \frac{\sum x_{IA}}{\sum x}, \quad \text{EAVF} = \frac{\sum x_{EA}}{\sum x}. \quad (2.32)$$

As cylinder signals can be quite similar, Benjamini et al. proposed to use an optimized Double Diffusion Encoding (DDE) protocol that minimizes the mutual coherence of the design matrix D [13, 14, 15]. This approach reduces the ill-posedness of the problem, providing more robust ADD estimates compared to single diffusion encoding sequences [14]. The method also provides non-parametric ADD estimates, as opposed to AxCaliber for example, which imposes the distribution to follow a parametric shape.

2.5 Validation and model evaluation

To validate that microstructure imaging does provide features that reflect real tissue properties, such features should be compared to a gold-standard. Finding an appropriate gold-standard is not an easy task [32]. Validation can be achieved by comparing dMRI estimates to tissue properties measured from microscopy, although such an approach is invasive and subject to some limitations. Another approach to evaluate the performance of dMRI methods is to use Monte Carlo simulations, where a virtual tissue sample is created to generate the dMRI signal, which is subsequently analysed with the method of interest, and the results compared to the parameters of the virtual tissue used in the first place.

2.5.1 Microscopy

Microscopy methods provide images of tissue at resolutions that are high enough to measure directly the features of interest. Electron microscopy (EM) has enough resolution to measure axon diameters for example, as shown in Figure 2.3. Assaf et al. showed good correspondence between the ADD estimated using AxCaliber and the ADD measured from EM (Figure 2.6).

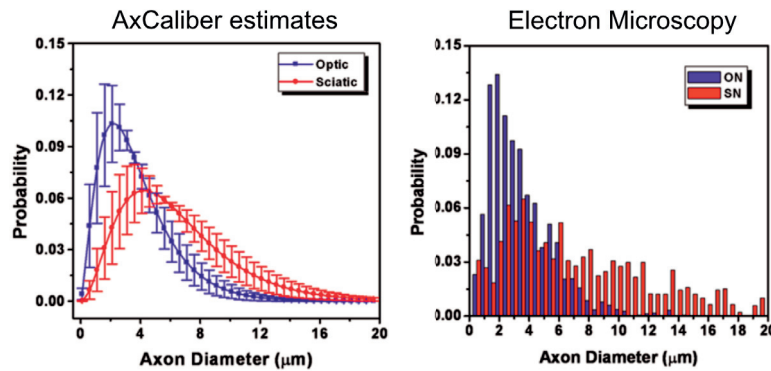


Figure 2.6 – AxCaliber estimates compared to Electron Microscopy, modified from [6], published by John Wiley and Sons, Copyright 2008, Wiley Liss Inc.

Lamantia and Rakic [59] have provided ADD estimates from EM section of rhesus monkey brains. Aboitiz et al. [1] provided similar data for the human corpus callosum. Such values have been used to compare estimates of the mean diameter index using the ActiveAx_{MMWMD}

model (Figure 2.7). Diameters estimated from MRI were consistently higher than the ones observed from histology. Such an overestimation can be explained to some degree by the "diameter lower bound" presented by Nilsson et al. [69], which describes the lowest diameter that can be statistically differentiated from a cylinder with zero radius. This lower bound is linked to the gradient strength used in the protocol, which was shown to influence diameter estimation, and therefore part of the mismatch between diameters estimated from MRI and from histology [31, 47, 87, 35]. Part of the overestimation of the mean diameter also rises from

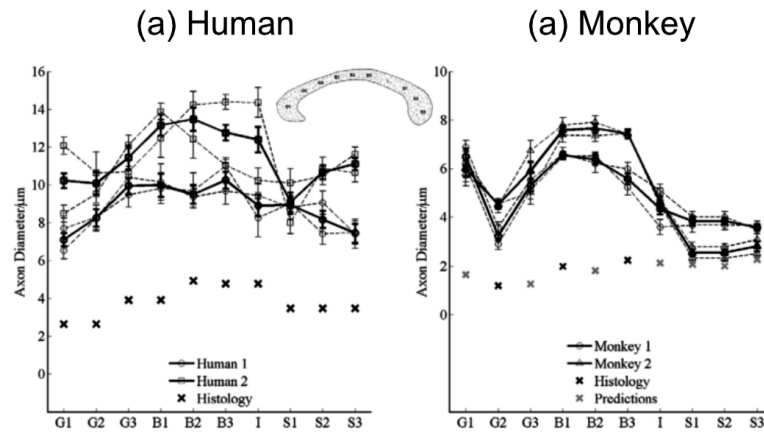


Figure 2.7 – ActiveAx estimates compared to Electron Microscopy measurements reported for (a) human subjects [1], and (b) monkeys [59]. Modified from [4], published by Elsevier Inc, Copyright 2010.

modeling approximations. For instance, the instantaneous diffusivity in the EA space was found to vary with diffusion time [18]. This time-varying behavior for the EA compartment was observed in vivo for the transverse component [36]. The EA compartment was also found contribute more to the overall time-varying perpendicular diffusivity compared to the IA compartment [62]. Modeling the EA compartment using a tensor (which is not time-dependent) leaves a residual that can be captured by the IA model, leading to diameter overestimation [27]. On the other hand, including time-dependence in the EA model reduces this overestimation [27].

Benjamini et al. [15] found good agreement between ADD estimates from dMRI and estimates from histology on a ferret spinal cord (Figure 2.8), although the histological ADD values have been questioned [49]. However, tissue samples have to undergo a series of preparation steps before EM imaging, like fixation, staining, and/or slicing, which might alter the structure of the sample before an image can be generated. The measured ADD might therefore not correspond to the ADD of fresh tissue.

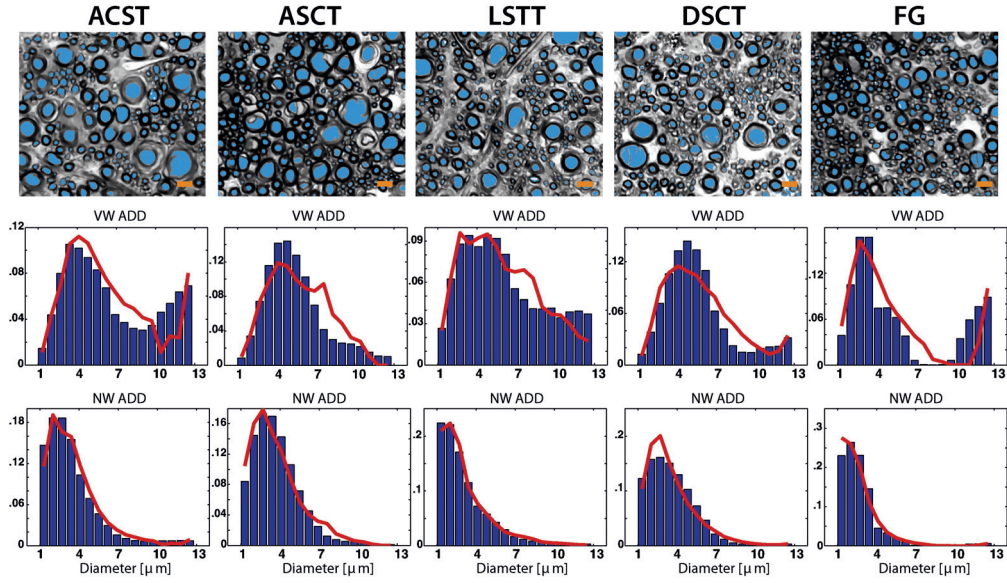


Figure 2.8 – ADD estimates using dMRI compared to estimates from EM. Reprinted from [15], Copyright 2016, with permission from Elsevier Inc.

2.5.2 Monte-Carlo simulations

Monte Carlo (MC) simulations provide a controlled environment where the user can fine tune the tissue properties. In MC simulations, a virtual tissue (or substrate) is created (Figure 2.9). Spins are modeled by dots that move randomly with a fixed step size computed according to their intrinsic diffusivity. If a spin encounters an "axon" membrane, it is elastically reflected. MC simulations can be used to compute the diffusion coefficient, using the average displacement of the spins during a given simulation time. Virtual diffusion gradients and inversion pulses can also be applied during the experiment, and the phase-shift of each spin computed at each timestep according to its displacement. The resulting DWI signal is then computed by taking the sum of all the spin's accumulated phase-shifts.

MC simulations have the advantage that the virtual tissue is exactly the same when generating the dMRI signal and when computing tissue properties for model evaluation. This advantage comes at the cost of computation time and power. Simple WM geometries that might deviate from real WM tissue (*e.g.* perfectly parallel and impermeable cylinders), are required in order to decrease the aforementioned computational burden.

2.5.3 Volume weighting

As mentioned earlier, dMRI measurements are weighted by volume fractions. Dyrby et al. [32] pointed out that dMRI was shown to have a diameter lower bound that is specific to protocol settings, and under which the mean diameter index cannot be reliably estimated [31, 69]. The

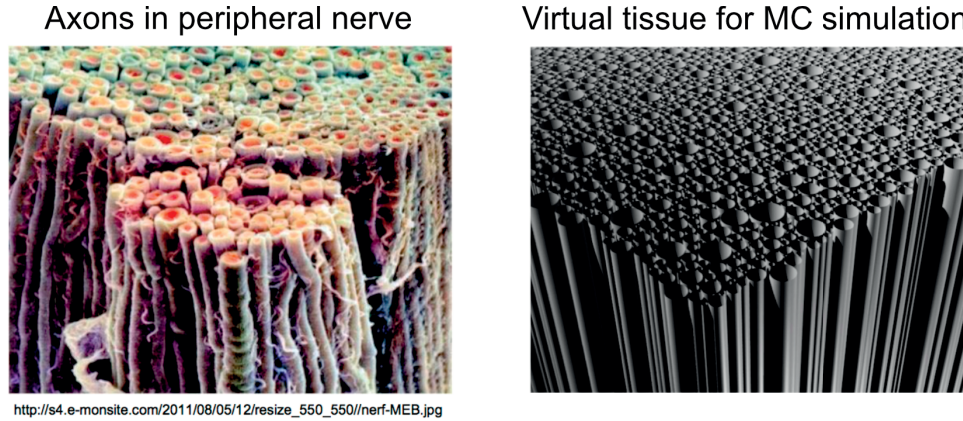


Figure 2.9 – Virtual WM structure used for MC simulations

diameter lower bound has been shown to be a function of acquisition noise, spin diffusivity, as well as pulse duration and amplitude [69]. Concerning simulation results for ActiveAx, a large proportion of cylinders used in the simulated substrates are above this lower bound, which might explain the overall good agreement between simulations and the estimated mean diameter index [4, 31]. However, most axonal population in the primate brain have a peak below $1\ \mu\text{m}$ [93, 63, 50], which is below the aforementioned lower bound. For microstructure models, such axons would appear as having a diameter of zero, and they would therefore not contribute to the estimated mean diameter index. Mean diameter index estimated from histology does take into account those small diameters. This might partially explain why the mean diameter index estimated using microstructure imaging is overestimated compared to observations from EM, even though they both follow the same trend (Figure 2.7) [32]. Discrepancies between microstructure imaging estimates and EM might also rise from the blunt approximations done in order for the problem to remain tractable, namely the hypothesis that axons are impermeable and parallel structures, while axons are known to undulate [70], have a dispersed geometry [102] and have some permeability to some extent [60].

2.6 Conclusion

Non-parametric ADD estimation has been shown to be feasible using DDE. In this thesis, non-parametric and orientationally invariant ADD estimation using PGSE is studied in detail. As the proposed models are evaluated using simulated dMRI signals, the importance of using realistic voxel sizes is first presented. Then focus is driven on the IA and EA compartments separately to understand the challenges at stake. The last chapter finally presents preliminary work showing improved ADD estimates from combined compartments.

3 Effect of voxel size on the dMRI signal

Overview

MC simulations are widely used to evaluate the performance of microstructure models or as input for such models [83]. In this chapter, we show the importance of considering the voxel size when generating dMRI signals using MC simulations. Results were presented at the 26th International Society for Magnetic Resonance in Medicine (ISMRM) Annual Meeting (Publication 1), as well as part of an article to be resubmitted for peer review to NeuroImage [81] (Publication 2). Our results motivate the use of realistic voxel sizes for the MC simulations used in the remaining chapters.

3.1 Introduction

Ex vivo and in vivo dMRI acquisitions involve in-plane voxel resolutions of the order of $500 \times 500 \mu\text{m}^2$ for animal imaging and $2.0 \times 2.0 \text{ mm}^2$ for humans. Given this voxel size, and keeping in mind our simplified model of WM, the hindered signal perpendicular to the axons should be isotropic and is therefore usually modeled as a axi-symmetric tensor [7, 2, 77]. While real WM might present non-symmetric fanning or dispersion [91], or also undulating patterns [70], we here focus on the assumption that WM can be approximated by perfectly parallel cylinders, whose hindered compartment can be assumed to be axi-symmetric. In order to evaluate the performance of such models, dMRI signals have been generated using MC simulations, and contaminated with rician noise before model fitting and comparison of estimates with ground-truth values [4, 31, 25]. Other approaches have also made use of MC simulations to fit dMRI signals and recover the underlying microstructure [83]. Simulating dMRI signals using realistic voxel sizes is demanding in terms of memory and computation time [40]. MC simulations are therefore usually performed in voxels of much smaller size, containing a few hundred cylinders [40, 4, 31]. Such an approach implicitly assumes that the substrate's geometry is complex enough to approximate the signal from voxels with realistic sizes. Such an approach has two limitations. First, concerning the IA signal, sampling a few

cylinders is unlikely to generate a representative set of the sampled distribution. The MR signal being volume weighted, over or under representation of big cylinders might heavily influence the MR signal. The restricted compartment in MC simulations using a few hundred cylinders is therefore unlikely to represent the restricted compartment arising from several thousand cylinders. Second, concerning the EA signal, sampling a few hundred cylinders might limit the number of micro-environments sensed by the spins during the diffusion experiment. If that's the case, increasing the number of spins would not improve the estimates, as that would not increase the number of local micro-environments. Small voxels might be representative of bigger ones for particular protocols (at low b-value for example), but there is no evidence of that hypothesis being valid in general. This chapter explores the validity of such hypothesis for a protocol with high gradient strength and various diffusion times, as might be achieved in high-end scanners.

3.2 Methods

The 1st substrate was generated by sampling 100 radii from a Gamma distribution with parameters $\Gamma(3.27, 4.91E - 7)$. Corresponding cylinders were then placed randomly in a voxel with side $40.5 \times 40.5 \mu\text{m}^2$, such that the IA volume fraction was 60%, and imposing periodicity at the voxel boundaries [40]. The sampled diameters were ordered from largest to smallest, and the position randomly chosen within the voxel. In case of overlap with previously positioned cylinders, a new position was sampled, until there was no overlap with any previously positioned cylinder. Cylinders were aligned with the z-axis. The dMRI signal was generated with an in-house MC simulator [79, 81]. The software was implemented in c++, and takes as input the position of cylinders (including mirrors for the periodicity at boundaries), the number of spins, their initial compartment, the intrinsic diffusivity and the diffusion protocol to simulate. It also takes the number of steps to compute. The duration of the experiment (the TE) is divided into the number of steps, giving a step duration. From the diffusivity, a step length is computed. Each spin takes a step with this given size in a random direction, and get elastically reflected by cylinder walls. The signal is computed by summing the dephasing of each spin due to their trajectories. The same simulator was used in all the simulations presented in the next chapters. For the current experiment, 1×10^6 spins were placed in the EA space with diffusivity of $1.7 \times 10^{-9} \text{ m}^2/\text{s}$, TE=75 ms and 5000 steps. With such setting, each time step was of $15 \mu\text{s}$, and each random step had a length of $0.32 \mu\text{m}$. Additional experiments with a diffusivity of $0.6 \times 10^{-9} \text{ m}^2/\text{s}$ and twice the number of steps showed similar results. The diffusion protocol was set with $G=300 \text{ mT/m}$, $\delta=10 \text{ ms}$ and Δ from 15 to 100 ms, acquired in 180 directions distributed in the perpendicular plane (xy-plane).

The remaining substrates were generated by replicating the initial list of 100 cylinders $N=2,3,\dots,100$ times, and the corresponding cylinders placed in voxels whose sizes were adapted such that the IA volume fraction was 60%. The generated substrates therefore all have the exact same IA volume fraction and normalized distribution of radii as the 1st substrate. The dMRI signals were generated using the same procedure as described above.

The capacity of the MC/DC Simulator [81] to accurately mimic the diffusion process of spins in the hindered compartment has been previously validated using a Finite Element Method (FEM) approach [80]. A set of spins was initialized in a few points and allowed to diffuse and interact with a set of cylinders. The density of spins at the end of the experiment was compared to the density obtained by solving for the diffusion equation over a tessellation of the hindered space using FEM. Results were similar for both the FEM and the MC/DC approaches. The dMRI signal obtained for a small substrate was compared to the signal generated using the MC simulator implemented in Camino, using the same set of cylinder position, substrate size, number of spins, intrinsic diffusivity and diffusion protocol. Both simulators provided signal samples that were identical up to the 4th decimal, making the MC/DC simulations trustworthy.

Additional experiments were carried using a distribution of cylinders with approximately half the diameter of the ones used at first.

3.3 Results

The radial signal was observed to be more and more anisotropic as the voxel size decreased. The anisotropy was also increased for longer diffusion times. Results for 3 substrates with cross-section sizes of 406×406 , 181×181 and $40.5 \times 40.5 \mu\text{m}^2$ are summarized in Figure 3.1. The first row shows the cylinder positions on cross-sections of the substrates. For visibility, the same scale was used on all sections, and the voxel boundaries marked with a dotted blue line. The periodicity of the cylinders is therefore visible for the voxel with size of $40.5 \times 40.5 \mu\text{m}^2$. The second row displays the substrates' corresponding radial EA signals.

Figure 3.2 shows the mean and normalized standard deviation of the EA signal as a function of substrate size. The normalized standard deviation was computed as:

$$\frac{\sum_i (\frac{S_i^\perp}{\bar{S}^\perp} - 1)^2}{N - 1}, \quad (3.1)$$

where \bar{S}^\perp was the mean radial signal and N was the number of samples, quantifying how much the signal deviates from a perfectly isotropic signal.

Isotropic EA signals could also be recovered by averaging many small substrates. The signals of 100 substrates of size $40.5 \times 40.5 \mu\text{m}^2$ (each with shuffled cylinder positions) were averaged. The resulting EA signal had a normalized standard deviation and amplitude that were equivalent to the signal obtained for a voxel of $406 \times 406 \mu\text{m}^2$.

Regarding the distribution of cylinders with half the diameter, results indicated that half the voxel size was required to obtain signals with satisfying isotropy.

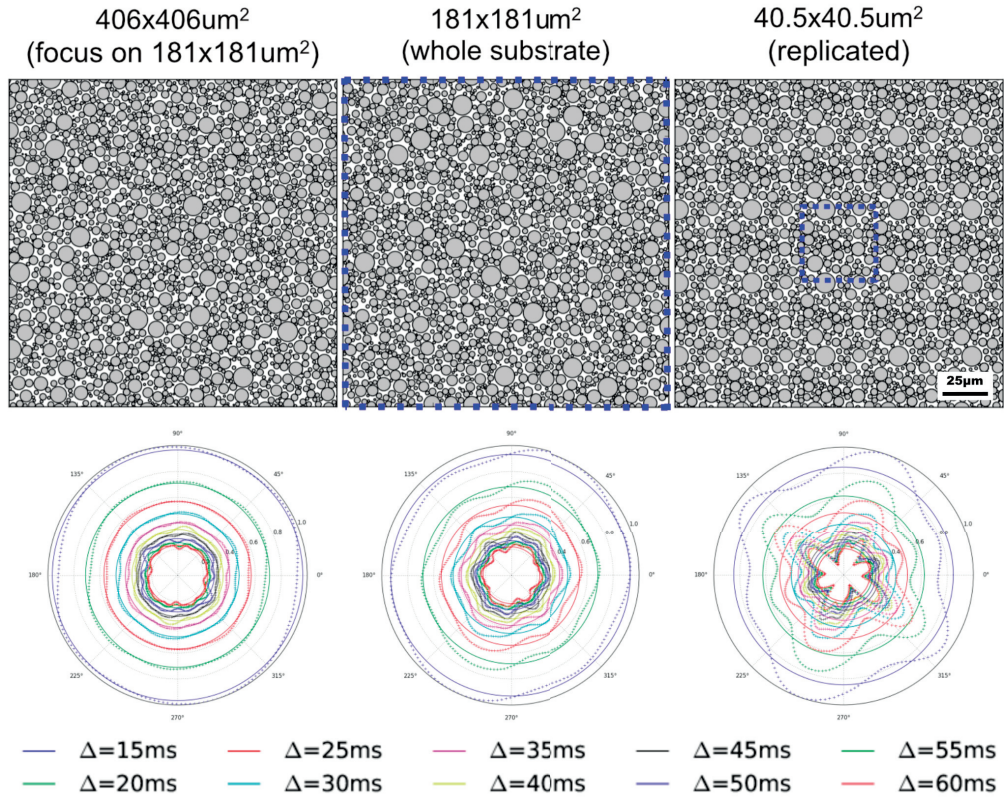


Figure 3.1 – Effect of voxel size on the MC signal for three different substrates.

3.4 Discussion

Although substrates were composed of perfectly parallel cylinders, results showed that the radial EA signal generated with MC simulations was highly anisotropic for small voxels, illustrating the influence of voxel size on the simulated signal. Small voxels showed anisotropic profiles over the perpendicular plane, while bigger voxels had more isotropic profiles. Our experiments therefore confirm the hypothesis that the EA signal is axi-symmetric in voxels with a size of the order of millimetres, but reject the hypothesis that the signal of big voxels can be approximated by MC simulations in smaller ones.

The anisotropy observed in small voxels might arise from the fact that a reduced size limits the diversity of local environments explored by the spins during the diffusion time. Having "fewer" local microenvironments, it is more likely that spins diffuse faster in certain directions compared to bigger voxels where the diversity of microenvironments is higher.

Reshuffling cylinder positions creates new combinations of local microenvironments. Averaging the signals of several small substrates might therefore be equivalent to increasing the spectrum of environments sampled by the spins, which is why the resulting signal looks similar to the signal of a bigger voxel.

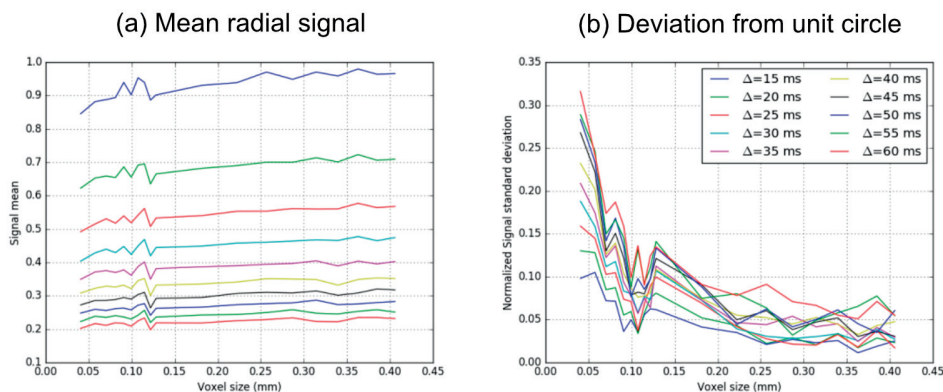


Figure 3.2 – Effect of voxel size on the mean radial MC signal and its anisotropy.

In practice, dMRI signals from voxel sizes of the order of millimetres cannot be approximated by using MC simulations in a single small voxel. When using MC simulations to evaluate microstructure models, voxel sizes of the order of $400 \times 400 \mu\text{m}^2$ should be used to avoid biasing estimates when using a distribution similar to the one used in our experiments. In general, more than 5'000 cylinders seem to be required in order to have a hindered compartment that is "rich" enough for the molecules' radial mean squared displacement to be independent on the orientation.

Anisotropic profiles might be observable in large voxels containing cylinders fanning non-symmetrically. The Bingham distribution (which is not symmetric), has been proposed to improve the fitting of dMRI signals acquired on real data [91]. If such a model was to be evaluated using MC simulations, our results indicate that experiments should be carried on large voxel sizes in order to avoid introducing anisotropic profiles due to the limited number of micro-environments instead of the non-symmetric bending of cylinders.

Implementation of MC simulators that are able to cope with the computational cost of such simulations is therefore important [81]. Researchers without access to such simulators still have the option to average the signal of many small substrates in order to reduce the bias. The MC simulator implemented in Camino has recently been updated to be able to cope with larger structures [41], and the use of this feature should be promoted to avoid biasing results for simulations using high gradient strengths.

3.5 Conclusion

As voxel size has an effect on the radial dMRI signal of the EA compartment generated with MC simulations, all the simulations used in the remaining chapters were conducted using a fixed voxel size of $500 \times 500 \times 500 \mu\text{m}^3$.

4 ADD estimation using ActiveAx_{ADD}

Overview

The following chapter extends the ActiveAx_{AMICO} model from a single diameter estimation method to a model for orientationally-invariant and non-parametric ADD estimation. Part of the work presented here was presented at the ISMRM workshop on Breaking the barriers of diffusion MRI in Lisbon (Publication 3) and at the 25th ISMRM annual meeting in Honolulu, USA, April 22-27, 2017 (Publication 4). The content of the whole chapter was submitted for peer-review to Magnetic Resonance in Medicine (MRM) [85] (Publication 5).

4.1 Introduction

ADD estimation using dMRI data remains challenging, mainly due to the similarity between the dMRI signals of cylinders with close diameters [13]. The problem is degenerate (or ill-posed), in the sense that very different ADDs have very similar dMRI signals. A small variation in the signal (e.g. due to noise) can thus drastically change the solution, providing microstructural estimates that do not reflect the underlying tissue microstructure. Several approaches have been proposed to address this ill-posedness, as presented hereafter.

The AxCaliber method proposed by Assaf et al. [6] recovers ADDs that are constrained to follow a given parametric distribution [10, 46, 27], in order to reduce the number of parameters to estimate. This forces the ADD to follow a specific shape, which might not always be appropriate. AxCaliber relies on the Pulsed Gradient Spin Echo (PGSE) sequence [89]. Benjamini et al. [15] proposed to estimate the ADD using a discrete linear model, thus providing non-parametric ADD estimates, but using a Double Diffusion Encoding (DDE) acquisition. Both methods require the orientation of the axons to be known prior to the acquisition, which limits these methods to well oriented structures like the corpus callosum or the spinal cord. Indeed, the required number of diffusion samples is such that it would be infeasible to acquire them using a High Angular Resolution Diffusion Imaging (HARDI) protocol (i.e. a protocol where each diffusion samples is acquired densely over the unit sphere, which allows the orientation of the

fibers to be estimated a posteriori, providing orientationally invariant estimates). To provide orientationally invariant metrics, Alexander et al. proposed the ActiveAx framework [4]. The framework includes an optimization algorithm that designs an ad hoc multi-shell (i.e. multiple b-values) HARDI protocol (allowing orientationally invariant estimates) for estimating the mean diameter. The framework can be adapted for ex vivo or in vivo samples, monkey or human subjects, as well as to the scanner hardware limitations [4, 31]. The ActiveAx framework relies on the Minimal Model for white matter diffusion (ActiveAx_{MMWMD}) which fits a single cylinder to the IA signal, thus reducing the number of parameters to one but losing information regarding the shape of the ADD.

All these approaches trade the robustness of estimates for other aspects. Ideally, an ADD reconstruction method should provide the whole non-parametric ADD without requiring prior knowledge on the orientation of the fibers (Table 4.1).

	Whole ADD	Non-parametric	Orientationally-invariant	PGSE
Assaf et al. [6] (AxCaliber)	✓	✗	✗	✓
Benjamini et al. [15]	✓	✓	✗	✗
Alexander et al. [4] (ActiveAx _{MMWMD})	✗	✓	✓	✓
Proposed method (ActiveAx _{ADD})	✓	✓	✓	✓

Table 4.1 – Properties of ADD mapping methods

On one hand, Daducci et al. [25] showed that the AMICO framework (Accelerated Microstructure Imaging using Convex Optimization) could be used to linearize the ActiveAx_{MMWMD} model. On the other hand, Hollingsworth and Johns [45] showed that non-parametric distributions of droplet sizes can be estimated from NMR signals by using Laplacian regularization. Here, the discrete linear framework provided by AMICO is combined with Laplacian regularization to estimate the full non-parametric ADD using data acquired with the ActiveAx protocol. The proposed method is coined ActiveAx_{ADD}, as it extends the use of ActiveAx to the estimation of the whole ADD. Performance is assessed using simulations with ex vivo parameters. Experiments first focus on the IA signal only, to compare performance between standard Tikhonov regularization and Laplacian regularization, and then explore the performance of the proposed method on the whole dMRI signal (mixture of IA and EA components).

4.2 Theory

The dictionary formulation presented in Chapter 1 is used:

$$\mathbf{y} = \mathbf{D}\mathbf{x} + \boldsymbol{\eta}, \quad (4.1)$$

where microstructure estimates can be extracted from the coefficients x obtained by solving:

$$\operatorname{argmin}_{x \geq 0} \|D\mathbf{x} - \mathbf{y}\|_2^2 + \lambda \mathcal{F}_r(\mathbf{x}). \quad (4.2)$$

When estimating the mean diameter index using ActiveAx_{AMICO}, standard Tikhonov regularization is used, where $\mathcal{F}_r(\mathbf{x}) = \|\Gamma \mathbf{x}\|_2$ and $\Gamma = I$ [15, 25]. The aim of the current chapter is to explore the benefits of using Laplacian regularization to provide non-parametric estimated of the ADD, as suggested by Hollingsworth et al. [45]. When using Laplacian regularization, $\Gamma = L_2^z$, where L_2^z is the 2nd order finite difference operator with zero boundary conditions [42]. The proposed formulation is coined ActiveAx_{ADD}.

4.3 Methods

4.3.1 Substrate design

Cylinder diameters were sampled from 22 different gamma distributions corresponding to histological samples [4, 59, 1] and randomly placed into isotropic voxels of 0.5x0.5x0.5mm³ to create 22 different substrates. All cylinders were aligned with the z-axis. The number of cylinders N_d was adapted in order to get IA volume fractions of 0.7 for each substrate. Cylinders were placed to ensure periodicity at the voxel boundaries [40]. Cylinder positions for the substrate with the lowest mean diameter could not be generated due to the high packing density and size of the voxel, and thus only appears in the IA experiments described hereafter. For illustrative purposes, properties of three of the generated substrates used in the current study are shown in Figure 4.1 (substrates with smallest, medium and biggest mean diameter index).

4.3.2 Estimates from the IA compartment's signal

Unless otherwise stated, all simulated signals in this chapter were computed using the 3-shell HARDI protocol with $G_{\max}=300\text{mT/m}$ optimized for mean diameter mapping using ActiveAx [31]: $G = 300, 219, 300 \text{ mT/m}$, $\Delta = 12.1, 20.4, 16.9 \text{ ms}$ and $\delta = 5.6, 7.0, 10.5 \text{ ms}$. Each of the 3 shells was acquired along 60 directions homogeneously distributed on the unit sphere [20]. By acquiring the signal homogeneously on a sphere, the orientation of the cylinders can be estimated from the data, and the dictionary build in the corresponding direction to estimate microstructural properties. The method is therefore orientationally invariant, in the sense that microstructural estimates do not vary with the orientation of the cylinders (which would be the case if the signal was acquired along a single direction for example).

Experiments were first focused on estimating Ψ from the IA signal. The IA signal y_{IA} was computed as $y_{\text{IA}} = \sum_{i=1}^{N_d} w_i S_{\text{IA}}(R_i, D^{\parallel}, \Omega)$ where w_i was the volume weighted fraction of each cylinder with respect to the total IA volume ($w_i = \frac{R_i^2}{\sum R_i^2}$). S_{IA} was computed using Van Gelderen's formula, based on the Gaussian Phase Approximation [96]. MC simulations for spins inside a

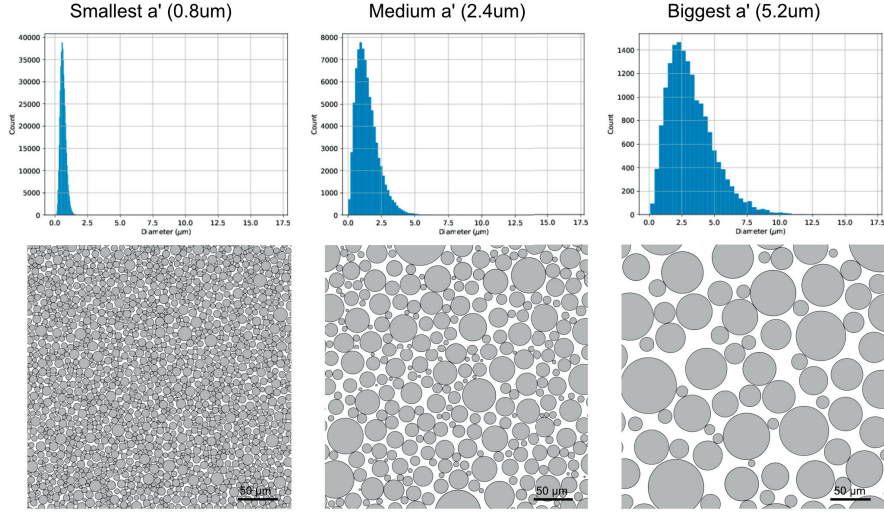


Figure 4.1 – Properties of the substrates with smallest, medium and biggest mean diameter index: diameter histogram and partial cross-section of the substrates showing some of the cylinder's positions.

cylinder of $10\mu\text{m}$ provided a signal almost identical to the analytical expression, when using the previously mentioned ActiveAx protocol. Diffusivity was set to reported values for ex vivo samples [4]: $D^{\parallel} = 0.6 \times 10^{-9} \text{m}^2/\text{s}$. The signal y_{IA} was computed for each substrate and contaminated with 50 different Rician noise realizations such that the noisy signals \hat{y}_{IA} had an SNR of 30 in the S_0 volumes.

The ActiveAx_{MMWMD} model proposed by Alexander et al. approximates the IA compartment using the signal of a single cylinder [4, 31]. To understand the validity of this model concerning the IA compartment, the diameter of the cylinder whose signal was the closest to the noiseless IA signal was reported. For the noisy signals \hat{y}_{IA} , the diameter index a' was estimated by performing MCMC sampling on the posterior probability of a single cylinder fitted to \hat{y}_{IA} , similarly to the implementation of the ActiveAx_{MMWMD} basic model in Camino [24].

To test the effect of regularization on the ADD estimation, x_{IA} was estimated from \hat{y}_{IA} by solving $\arg\min_{x_{\text{IA}} \geq 0} \|A_{\text{IA}}x_{\text{IA}} - \hat{y}_{\text{IA}}\|_2^2 + \lambda \|x_{\text{IA}}\|_2^2$ with either standard Tikhonov regularization (ActiveAx_{AMICO}) or Laplacian regularization (ActiveAx_{ADD}). No EA compartment was included in the model. The dictionary A_{IA} consisting of $N_A = 30$ cylinders was build with diameters equally spread between $0.5 \times 10^{-6} \text{m}$ and $20 \times 10^{-6} \text{m}$. λ controls how much the regularization penalty weights with respect to the data fidelity term. Higher weighting will thus provide smoother solutions. Different values for λ were tested, between 0.001 and 10, and was fixed to 0.2 for all experiments as this value provided the most accurate ADD reconstruction for a wide range of substrates. The estimated ADD was compared to the corresponding ground-truth by computing the Hellinger distance $H(P, Q)$: $H(P, Q) = 1/\sqrt{2} \|\sqrt{P} - \sqrt{Q}\|_2$ where P was the estimated ADD and Q was the ground-truth. For comparison with results of Benjamini et

al. [15], the Jensen distance was also computed, given by $JSD(P, Q) = \sum_i \frac{P_i \log(P_i) + Q_i \log(Q_i)}{2} - \frac{P_i + Q_i}{2} \log\left(\frac{P_i + Q_i}{2}\right)$, where P was the mean ADD estimated over different noise realisations and Q was the ground-truth. A small $\epsilon=1e-16$ was added to P_i and Q_i for the JSD to be valid even in the presence of zeros. Results were similar when ignoring terms i where P_i or $Q_i = 0$.

4.3.3 Influence of maximal gradient strength

As described in Dyrby et al. [31], the maximum gradient strength drives the sensitivity to the smallest axon size detectable by the ActiveAx_{MMWMD} model. The IA experiments were repeated for the different protocols proposed in Dyrby et al. [31], with G_{\max} of 140 and 60 mT/m respectively, exploring how robust the proposed method was to lower gradient strengths.

4.3.4 Influence of the EA compartment

The performance of the proposed method was then assessed on a more realistic dMRI signal, containing contributions from both the IA and EA compartments. The EA signal y_{EA} was computed from Monte-Carlo simulations, using an in-house software compiled on a Intel Xeon E5-2650 v2 cluster. One million spins with a diffusivity of $0.6 \times 10^{-9} \text{ m}^2/\text{s}$ were placed in the EA compartment and allowed to interact with the cylinders during $TE = 44 \text{ ms}$, divided in 5000 steps, while running the ActiveAx diffusion protocol with $G_{\max}=300 \text{ mT/m}$ presented above. The total signal was computed as $y = f_{IA} * y_{IA} + (1 - f_{IA}) * y_{EA}$, where f_{IA} was the IA volume fraction (set to 70%). 50 different noisy signals \hat{y} were generated for each substrate by adding Rician noise such that the SNR was 30 in the S0 volumes.

To take into account the EA space in our approach, the EA compartment was modeled by adding the EA dictionary A_{EA} , built using 7 EA atoms corresponding to 7 axi-symmetric tensors with perpendicular diffusivities uniformly sampled between $0.06 \times 10^{-9} \text{ m}^2/\text{s}$ and $0.42 \times 10^{-9} \text{ m}^2/\text{s}$ [4, 25]. The coefficient vector x was fit to the noisy data \hat{y} using Eq. 2.30 with Laplacian regularization. The smoothness penalty was only applied to the IA coefficients, as there was no evidence that smoothness should be promoted for the EA coefficients [15].

For completeness, the basic ActiveAx_{MMWMD} model (a single cylinder and an axi-symmetric tensor) was fit to the noisy signals \hat{y} using the Camino software. Camino implements a tortuosity constrain, in which the perpendicular diffusivity of the axi-symmetric tensor is set to be equal to the EA volume fraction times the parallel diffusivity.

4.4 Results

4.4.1 Estimates from the IA compartment's signal

When using only the IA signal, both ActiveAx_{AMICO} and ActiveAx_{ADD} provide robust estimates of the mean diameter index. Figure 4.2 shows the estimated diameter index a' for different

substrates, using the IA signals. Figure 4.2a and Figure 4.2b show the ActiveAx_{MMWMD} estimates when approximating the distribution by a single cylinder for the noiseless and noisy signals respectively. Even without noise, a slight overestimation was observable for diameters between 1.0 μm and 4.0 μm . Results for the noisy signals illustrate the ill-posedness of the problem, as small variations in the signal due to noise lead to a high range of estimated diameters for substrates with a' lower than 2.0 μm . The ActiveAx_{MMWMD} model was thus considered to have a lower bound around 2.0 μm , under which the mean diameter index could not be estimated robustly. This was in accordance with Eq. 15 in Nilsson et al. [69], for which the minimum diameter should be $d_{min}^{(SDE)} = (\frac{768}{7} \frac{\bar{\sigma} D_0}{\gamma^2 \delta g^2})^{1/4} = 2.7 \mu\text{m}$ (using the 3rd shell, an SNR of 30, significance level of 5% and 1 repetition). The observed lower bound for ActiveAx_{MMWMD} was likely decreased as the substrate is made of a mixture of diameters, and also because each sample on the sphere partially provided information on the perpendicular signal, which would mimic an increase in the number of repetitions. If the perpendicular signal had been acquired 60 times, $d_{min}^{(SDE)}$ would be 1.6 μm . The effective $d_{min}^{(SDE)}$ lies somewhere in between, which is what was observed. The mean diameter index was well estimated for bigger substrates. Figure 4.2c and Figure 4.2d show the mean diameter extracted using the ActiveAx_{AMICO} (Tikhonov regularization) and ActiveAx_{ADD} (Laplacian regularization) models respectively. Both methods performed similarly and showed accurate estimation of the diameter index a' , with a lower bound around $1.5 \times 10^{-6} \text{m}$. The absolute error between estimated diameter indexes and the ground truth had a mean of 0.25 μm and 0.21 μm for ActiveAx_{AMICO} and ActiveAx_{ADD} respectively (paired t-test $P < 0.001$). The use of Laplacian regularization improved ADD estimates compared to Tikhonov regularization, when using the IA signal. Figure 4.3 shows the ADD (mean and standard deviation) estimated from \hat{y}_{IA} using ActiveAx_{AMICO} or ActiveAx_{ADD}, for the three substrates shown in Figure 4.1. Estimates were overlapped with the ground-truth ADD. ActiveAx_{AMICO} overestimated the contribution of small diameters in Ψ , although the mean axon diameter index was properly estimated (Figure 4.2c). ActiveAx_{ADD} provided better reconstruction of the ADD, in particular regarding the contribution of small diameters. Over the set of all substrates, the ActiveAx_{AMICO} model had a mean Hellinger distance of 0.28 ± 0.06 between the estimated ADD and the ground-truth, while this values went down to 0.24 ± 0.09 for the ActiveAx_{ADD} model (paired t-test $P < 0.001$).

4.4.2 Influence of maximal gradient strength

Robust ADD estimation with ActiveAx_{ADD} required protocols with high gradient strengths. As shown in Figure 4.4, ADD estimates from IA signals using ActiveAx_{ADD} were less accurate for gradient strengths of 60 and 140 mT/m as compared to estimates from acquisitions with a gradient strength of 300 mT/m, in particular for substrates with small or big diameter indices.

4.4.3 Influence of the EA compartment

ADD estimates using ActiveAx_{ADD} were influenced by the addition of the EA compartment. Figure 4.5 shows the ADD estimates when the EA compartment was included in the signal

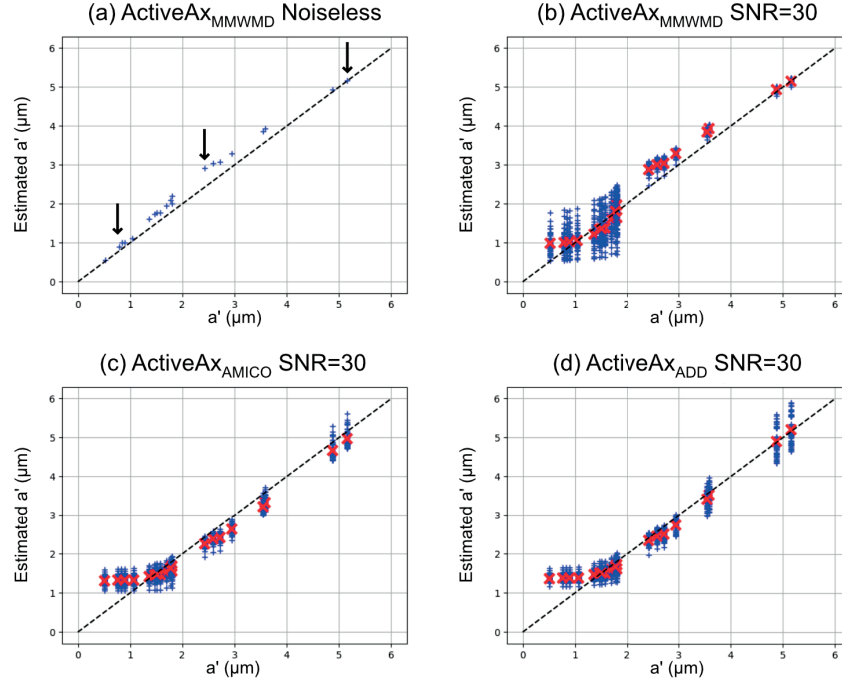


Figure 4.2 – Estimated a' for different methods using the IA signal only. (a) Fitting a single cylinder to the noiseless IA signal. Black arrows indicate the substrates reported in Figure 4.1; (b) Fitting a single cylinder using MCMC on the noisy IA signal; (c) a' extracted from Ψ estimated using ActiveAx_{AMICO}; (d) same as (c) with ActiveAx_{ADD}. Estimates of a' for each noise realisation is shown with a blue cross, while the mean over all realisations corresponds to the red cross. The ground truth lies over the dotted black line.

\hat{y} . A longer tail was observable (higher contributions for cylinders around 5 μm for the small substrate, and cylinders around 10 μm and 20 μm for the medium and large substrates). Overestimation of the contributions for the cylinders with diameter higher than 10 μm could indicate that the IA model was capturing part of the EA signal. However, the estimated IA volume fractions ranged from 0.5 to 1.0, when the ground-truth was 0.70. If only the EA compartment was being captured by the IA model, the estimated IA volume fractions would have been lower than 0.70. This indicated that the EA model was also capturing part of the IA signal (i.e. cross talk between compartment signals and models).

Boxplots summarizing the Hellinger distance between all reconstructed ADDs and their corresponding ground-truth are shown in Figure 4.6, for the different models presented earlier. When considering only the IA signal, Laplacian regularization decreased the median of the reconstruction error. Adding the EA signal increased the error in ADD estimation. Jensen distances for the mean ADD estimated from the IA signal only using ActiveAx_{ADD} varied between 0.016 and 0.172 over the different substrates (mean JSD and standard deviation were 0.048+/-0.046). When adding the EA compartment, Jensen distances varied between 0.018 and 0.282 (mean and standard deviation of 0.091+/-0.08). The ActiveAx_{MMWMD} model was also

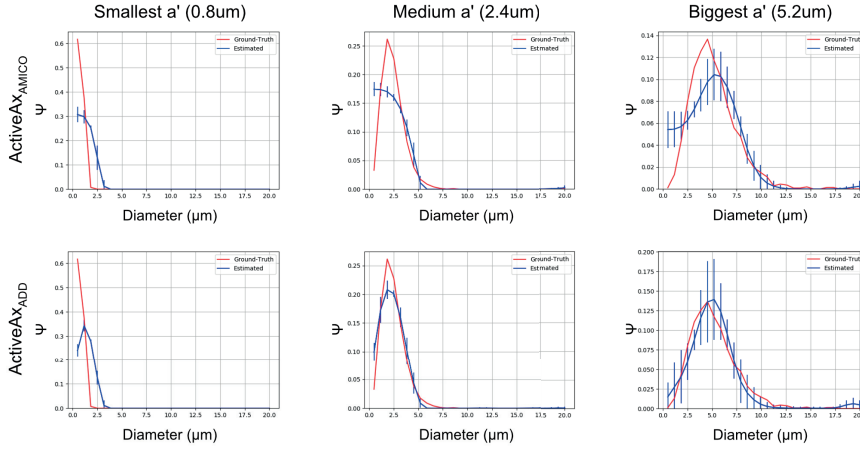


Figure 4.3 – ADD estimates compared to the ground truth, using either ActiveAx_{AMICO} or ActiveAx_{ADD}. The estimated ADD (mean and standard deviation) is shown in blue, while the ground truth is in red.

affected by the inclusion of the EA compartment (Figure 4.7). The ActiveAx_{MMWMD} model was not able to provide reliable estimates of the mean diameter index (mean absolute error $0.823 \pm 0.47 \mu\text{m}$). The discrete linear models performed better, with ActiveAx_{ADD} yielding estimates that were the closest to the ground truth. Results for ActiveAx_{ADD} were similar to estimates from the IA signal only (Figure 4.2d), although the absolute error between the estimated and the ground truth diameter index significantly increased (from an average of $0.21 \pm 0.18 \mu\text{m}$ when using the IA signal only to $0.65 \pm 0.53 \mu\text{m}$ when including the EA compartment, paired t-test $P < 0.001$). The lower bound in the estimation of the mean diameter increased to more than $2 \times 10^{-6} \text{m}$.

4.5 Discussion

Overall, by assuming that a mixture of cylinders can approximate the WM tissue, our results indicate that ActiveAx_{ADD} has the potential to provide precise non-parametric and orientationally invariant ADD estimates from a simple 3-shell PGSE protocol and for a wide variety of samples mimicking WM. The use of Laplacian regularization significantly improved ADD estimates when compared to standard Tikhonov regularization. The mean of the Jensen distance between the average ADD over 50 noise repetitions and the ground-truth ADD was of 0.048. Benjamini et al. reported Jensen distances varying between 0.007 and 0.062 regarding the volume weighted ADD [15]. When considering only the IA compartment, ActiveAx_{ADD} therefore provides ADD estimates from PGSE data that are as robust as using DDE, with the added value of parameters being orientationally invariant. Orientationally invariant ADD estimation using DDE might be feasible using the 5-design protocol proposed by Jespersen et al. [53], but to our knowledge no study so far has reported stable ADD estimates using this approach. Improved ADD reconstruction is related to the zero-boundary condition, which

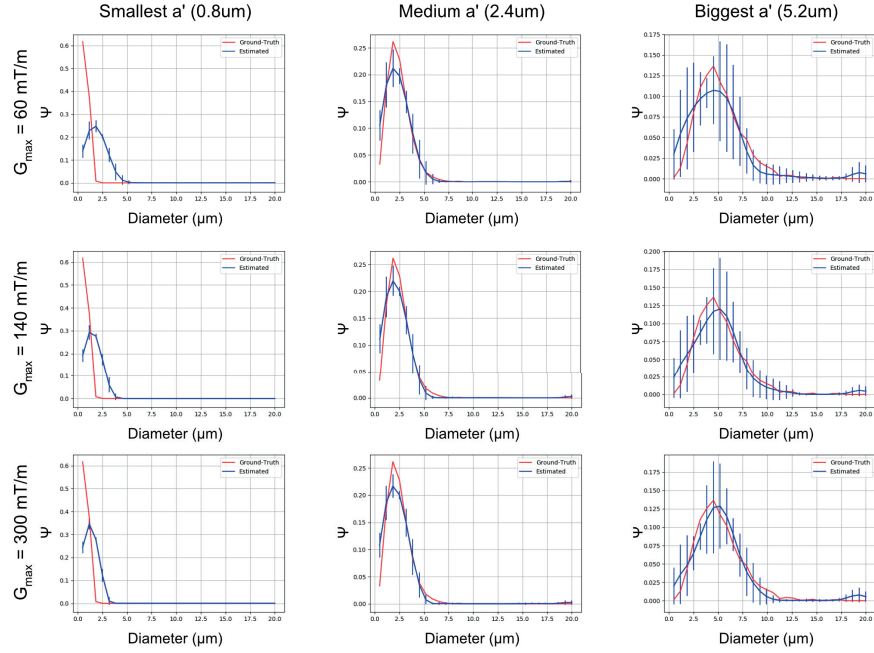


Figure 4.4 – Effect of G_{\max} on the estimated ADD using ActiveAx_{ADD} on IA signals.

promotes solutions with a small weight at the boundaries. Promoting such solutions goes in line with what has been observed in histology [59, 1, 10, 63]. Laplacian regularization might have an extrapolation effect, extending the ADD below the diameter lower bound by smoothly prolonging the trend in the weights of the diameters the protocol is sensitive to. Laplacian regularization also has a direct impact on the estimated diameter index a' . ActiveAx_{ADD} provides estimates with lower absolute error as well as a decreased lower bound compared to ActiveAx_{MMWMD}. The lower bound for ActiveAx_{MMWMD} was considered to be of the order of $2.0\mu\text{m}$, as the standard deviation of the estimated mean diameter significantly increased below this value (*e.g.* a substrate with diameter $1.8\mu\text{m}$ could be estimated to have a diameter between 0.8 and $2.5\mu\text{m}$ due to noise only).

However, ActiveAx_{ADD} inherits one of the main limitations in biophysical models, namely the similarity between the IA and EA signals. Biophysical models do not form an orthogonal basis for the dMRI signal. Part of the IA signal can therefore be captured by the EA model, and vice versa, which is what was observed in our experiments. This goes in line with results from Jelescu et al. [51], which show the degeneracy of compartment models. The use of other dMRI sequences like oscillating gradients or DDE [22] might increase the difference between the signals of the two compartments, making it easier for the reconstruction method to disentangle them, but careful experiments should be carried on in order to verify this.

In real WM tissue, the spins in the IA space might have higher diffusivity than the spins in the EA compartment [58]. Although having different diffusivities might make it easier to distinguish the two compartments, the formulation used in ActiveAx_{ADD} requires an estimate

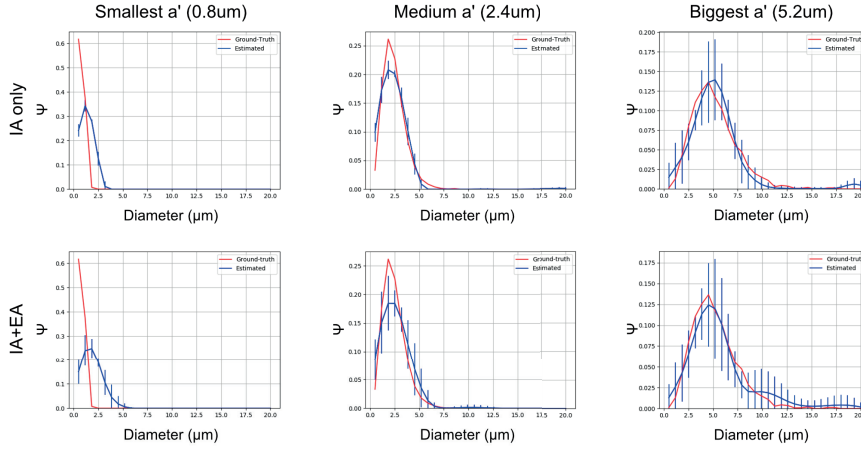


Figure 4.5 – Influence of the EA compartment on the estimated Ψ from pure IA signals and IA+EA signals. Estimates are shown in blue and the ground-truth ADD is shown in red.

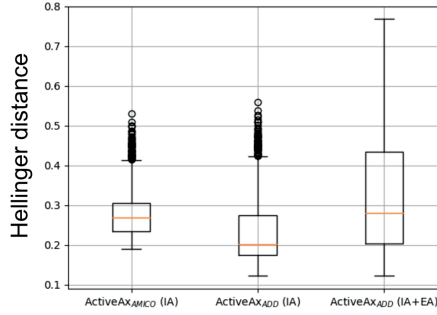


Figure 4.6 – Hellinger distance between all reconstructed ADDs and their corresponding ground-truth, for the ActiveAx_{AMICO} using IA signals (left), ActiveAx_{ADD} using IA signals (middle) and ActiveAx_{ADD} using IA+EA signals (right).

of the compartment diffusivity. By assuming the same diffusivity in both compartments, it can be estimated from the dMRI signal using its tensor first eigenvalue, which corresponds to free diffusion. Estimating two diffusion coefficients is much less accurate, in particular because the volume fraction of each compartment needs to be estimated too, worsening the ill-posedness of the problem. Such a case was therefore not explored within the scope of this thesis.

Sources of cross-talk between signals and compartments might also include modeling inaccuracies. The appropriate model to be used for the EA compartment is still debated [18, 27]. Several methods assume it can be modeled using a gaussian and axi-symmetric tensor [5, 6, 10, 4, 31, 25, 15]. De Santis et al. proposed to include a time-dependent model for the EA dMRI signal, showing improvement in the estimation of the mean diameter index estimated from a parametric ADD reconstruction method [18, 27]. The improvement in the estimation of a' indicates that choosing an appropriate EA model might improve ADD estimates when

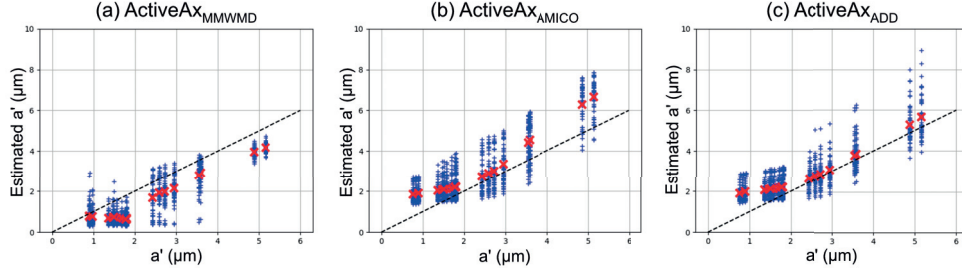


Figure 4.7 – Effect of the EA compartment on the estimated mean diameter index a' for different reconstruction models.

considering the IA and EA signal. A proper method should be proposed and validated before applying $\text{ActiveAx}_{\text{ADD}}$ to real data.

In terms of acquisition, our experiments are based on an ActiveAx protocol, consisting of only 3 shells [31], that is optimized for mean diameter mapping. Such a protocol can easily be implemented on a pre-clinical scanner with sufficiently strong diffusion gradients. Indeed, as shown by our experiments, a maximum gradient strength of 300 mT/m is required in order to obtain reliable ADD estimates as well as a decreased lower bound for the estimated mean diameter index [31]. Optimizing the HARDI protocol for ADD mapping, or using other sequences like oscillating gradients, might further improve the quality of the results [30].

Results regarding ADD estimates using only the IA dMRI signal are in accordance with the experimental observations of Hollingsworth and Johns [45]. Indeed, their work was demonstrated on an emulsion of oil in water, by following the attenuation in the aromatic peak in the NMR spectrum of the sample. The signal could therefore be assumed to be composed of a single restricted compartment, without the need to deal with other types of diffusion, like hindered diffusion. Our results are therefore promising for the field of microstructure spectroscopy. Indeed, diffusion Magnetic Resonance Spectroscopy (dMRS) sequences allow isolating the diffusion signal for very specific metabolites like N-acetyl-aspartate and glutamate, which are physically restrained to the IA space [76]. Acquiring data on ex vivo or in vivo samples using spectroscopy could provide isolated IA diffusion signals that are not influenced by the presence of the EA compartment. Furthermore, the diffusion coefficient of metabolites being smaller than the one of water [76], the diameter lower bound described by Nilsson et al. should in theory be smaller [69], allowing to estimate smaller diameters. The main drawback would nonetheless be the limited resolution provided by dMRS methods, which require voxel sizes of the order of centimeters in order to achieve a reasonable SNR, which could easily break the assumption of a single axonal orientation within the voxel. Results are also promising for acquisitions done at very high b-value, as made possible by recent high-end scanners like the Connectome Scanner. At such high b-values, the EA signal could be considered to be negligible, making it possible to focus on the IA compartment only. Careful experiments should also be performed in order to ensure that the EA compartment can be

effectively ignored (*e.g.* MC simulations).

Application to real data should also take into consideration the following. First, T1 and T2 relaxation effects should be taken into account, as there might be differences between compartments. This would affect the measured signal, and the estimates would then correspond to signal fractions instead of effective volume fractions. The IA and EA compartments might also have different parallel diffusivities, which are not easily determined [51]. The validity of the WM model should also be verified before. Indeed, if the axons are not perfectly parallel, estimates might be biased. This might be addressed by including dispersion in the proposed method, as done by Zhang et al. [101].

4.6 Conclusion

Non-parametric and orientationally invariant ADDs can be reliably reconstructed from PGSE data using ActiveAx_{ADD}, when considering only the IA compartment. ActiveAx_{ADD} is based on an optimized 3-shell ActiveAx protocol, and therefore doesn't require information on the orientation of the fibers before the acquisition. It provides better ADD reconstructions compared to ActiveAx_{AMICO}, which directly increases the accuracy of the estimation of the mean diameter index. The method inherits common limitations in microstructure models, in particular regarding the axon diameter lower bound and cross talk between IA and EA compartments and models. The cross talk between IA and EA compartments needs to be reduced before applying the method to real data. In Chapter 5, we explore the potential benefit of using a richer dMRI protocol optimized to increase the sensitivity to a set of diameters. Chapter 6 on the other hand proposes a new model that better captures the EA signal. Finally, Chapter 7 presents preliminary results showing improved ADD reconstruction when considering both the IA and EA compartments.

5 Reconstruction of unimodal and multimodal distributions

Overview

In the previous chapter, the use of Laplacian regularization was shown to improve ADD estimation. In this chapter, we explored whether changing the parameters of the PGSE sequence could improve ADD reconstruction, for both unimodal and bimodal distributions.

5.1 Introduction

As seen in the Chapter 2, ADD changes during development as well as in disease events. Some evidence seems to point out that certain neurodegenerative disease have different effects on axonal populations depending on their size [34]. ADD mapping not only has the added value to provide the whole ADD compared to mean axon diameter mapping, it could also provide information on population specific changes if the method is sensitive enough. Here, we present a method for non-parametric ADD reconstruction based on a PGSE sequence optimized to maximize sensitivity to a set of diameters, and study its performance using simulations. We first show that a 20-shell protocol allows robust unimodal and bimodal ADD reconstruction when using the IA signal only. To our knowledge, bimodal distribution have not been observed in histological studies of WM, as reported histograms are usually smooth and contain a single peak for the studied pathways. However, bimodal distributions might arise in large voxels, where two fascicles with different diameters might converge, as in the internal capsule for example. The effect might be even more pronounced when acquiring dMRI datasets using isotropic encoding. Crossing fascicles in the centrum semiovale for example will be "merged" into a single distribution, which would appear to be bi-modal. Nevertheless, results regarding multimodal ADD reconstructions showed that a minimum distance between underlying populations is required to detect population specific changes, namely a distance larger than most axons in WM. Results are however transferable to other cell types, like prostate cells, which have diameters that are an order of magnitude larger than axons.

5.2 Methods

Reconstruction framework

We assume the dMRI signal can be expressed as follows [15]:

$$y = \sum_{i=1}^{N_r} \Psi(d_i) S_1(d_i, d_{\parallel}, \Omega^*), \quad (5.1)$$

where $\Psi(r)$ is the volume weighted ADD, S_1 is the dMRI signal for a cylinder [96] of diameter d_i , parallel diffusivity d_{\parallel} and PGSE protocol settings Ω^* . The signal is acquired in 60 directions. We focus on ex-vivo imaging and IA signal only, and therefore ignored the EA compartment. Equation 1 can be expressed as a linear formulation $y = Dx$, where we build D and x can be recovered from the convex inverse problem [45, 25, 15]:

$$\underset{x \geq 0}{\operatorname{argmin}} \|Dx - y\|_2^2 + \lambda \|\Gamma x\|_2^2. \quad (5.2)$$

Ill-posedness can be reduced by decreasing the mutual coherence of D (using DDE [13] for example), by using regularization $\lambda \|\Gamma x\|_2^2$ [45], and/or by extracting the mean diameter index a' instead of Ψ [4, 25]. We proceeded as done in the previous chapter, that is using Laplacian regularization $\Gamma = L_z^2$ [45], but this time with a PGSE protocol designed to maximize sensitivity to a range of diameters matching our biophysical model.

Protocol design and ADD reconstructions

The PGSE parameter space was considered to be $\Omega = \{G, \delta, \Delta\}$. We performed a grid-search on Ω [30] in order to find a set of 20 shells Ω^* that maximized the sensitivity $S'(d_i)$ to a set of 20 diameters d_i : $S'(d_i) = \|S_1(d_i + \epsilon, \Omega_i) - S_1(d_i - \epsilon, \Omega_i)\|_2$. We bounded Ω to $G_{\max} = 550\text{mT/m}$, $2 < \delta \leq 70\text{ms}$ and $\delta + 6\text{ms} < \Delta$ for the protocol to be implementable on a preclinical scanner.

The IA signals were computed as in the previous chapter, using our proposed protocol and ADDs from histological samples [59, 1, 4], and reconstructed Ψ from 100 noisy realisations (Rician noise with SNR=30).

We then created bimodal ADDs with two gaussians: a first fixed population N_1 ($\mu_1 = 4.0\mu\text{m}$) and a second moving population N_2 with increasing mean μ_2 . We extracted two estimated means, $\hat{\mu}_1$ and $\hat{\mu}_2$ by fitting a gaussian mixture model to the estimated Ψ . A second experiment tested if the method is sensitive to a reduction of 50% in the amplitude of N_2 . Relative amplitudes were set to 1:1 and 1:0.5 in the mixture model.

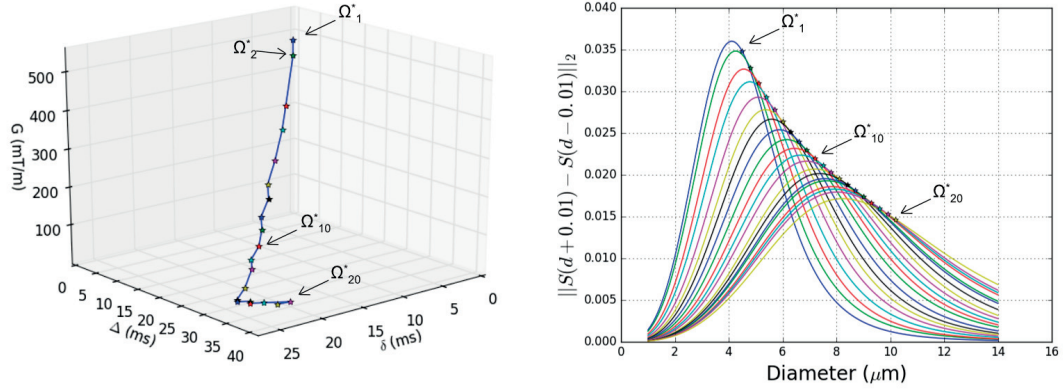


Figure 5.1 – Left: Positions of 20 selected shells Ω^* in the PGSE parameter space. Shells are ordered from Ω_1^* ($G=550\text{mT/m}, \delta=22\text{ms}, \Delta=28\text{ms}$) to Ω_{20}^* ($G=70\text{mT/m}, \delta=17\text{ms}, \Delta=52\text{ms}$). Right: sensitivity profile for each of the shells in Ω^* . Stars: sensitivity for the diameter Ω_i^* was selected for. Each color corresponds to a different shell.

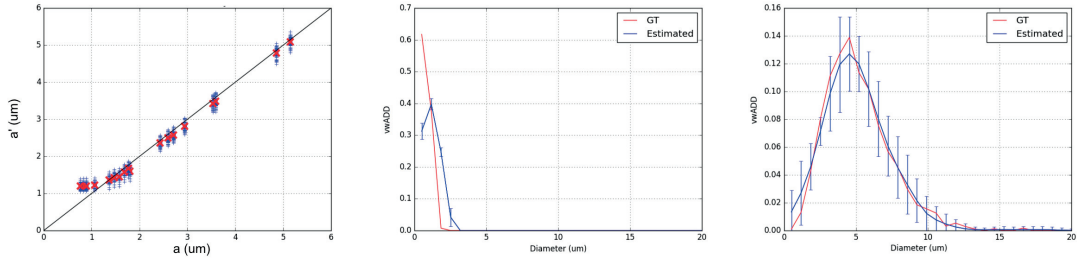


Figure 5.2 – Left: estimated a' compared to the ground-truth for different distributions. Middle: mean and standard deviation of the distribution coefficients estimated with our method, and compared to the ground-truth, for the distribution with a' below the diameter lower bound. Right: same as (middle) for the distribution with biggest diameter index.

5.3 Results & Discussion

The 20 selected shells maximized the sensitivity to diameters between $4.5\mu\text{m}$ and $10.0\mu\text{m}$ (Figure 5.1). Shells with maximum sensitivity for diameters lower than $4.5\mu\text{m}$ were beyond the limits of Ω . By maximizing sensitivity to a set of diameters, differences between columns of D was increased, reducing its mutual coherence.

Unimodal distributions

Unimodal distributions were reliably reconstructed for all simulations (Figure 5.2). The mean diameter index a' [4] was robustly estimated for values down to almost $1.0\mu\text{m}$, although the expected lower bound has previously been shown to be around $2\mu\text{m}$ [31]. As observed, in the

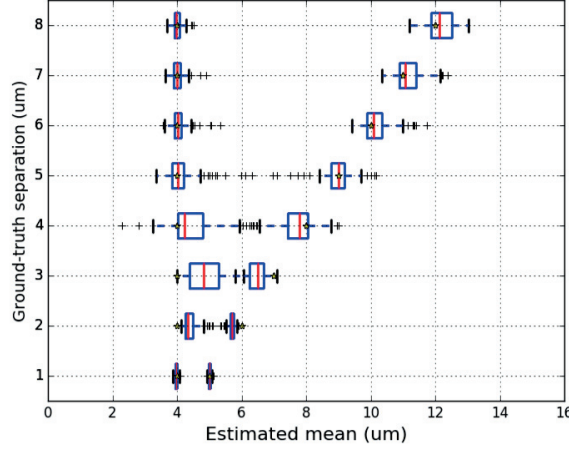


Figure 5.3 – Boxplots for the 100 estimated $\hat{\mu}_1$ and $\hat{\mu}_2$. Each line shows a boxplot summarizing the values of $\hat{\mu}_1$ (on the left) and $\hat{\mu}_2$ (on the right) extracted for a given separation between the two populations N_1 and N_2 . Ground-truth values μ_1 and μ_2 are shown by yellow stars ($\mu_1=4.0\mu\text{m}$ for all separation distances, while $\mu_2=[5.0\mu\text{m}, 6.0\mu\text{m}, 7.0\mu\text{m}, \text{etc..}]$). The 1st row mistakenly shows good performance for distances of $1.0\mu\text{m}$: N_1 and N_2 are collapsed into a single peak (wrong Ψ) but is then split into correct $\hat{\mu}_1$ and $\hat{\mu}_2$ by the mixture model (Figure 5.4).

previous chapter, the smaller lower bound might have been due to extrapolation properties of the regularization.

Resolving two axonal populations

As shown in Figure 5.3, N_1 and N_2 should be separated by at least $4.0\mu\text{m}$ for their respective means to be recovered (μ_1 and μ_2 are not within the 1st and 3rd quartiles of $\hat{\mu}_1$ and $\hat{\mu}_2$ for smaller separations). This minimal separation depends on the amplitude and variance of N_1 and N_2 . When N_1 and N_2 are far enough, $\hat{\mu}_1$ and $\hat{\mu}_2$ are well estimated, and population specific changes can be detected (Figure 5.4). Interestingly, preliminary results indicate that removing the last 10 shells of Ω^* compromised bimodal reconstructions while preserving robustness for unimodal distributions, showing that Ω_{10-20}^* provides information for bigger diameters.

Results presented here correspond to a proof-of-concept, showing the improvement of ADD reconstruction when designing the protocol to include sensitivity to a range of diameters. To our knowledge, bimodal distributions of axon diameters have not been observed within the same fascicle in histological studies. However, some fascicles "merge" in regions like the internal capsule, and this might result in bimodal distributions when measuring the dMRI signal on large voxels. Histological reports might not cover a field of view that is large enough to observe the multiple peaks. Bimodal distributions might also be observable when factoring out the macroscopic anisotropy (e.g. when using the Spherical Mean Technique or isotropic

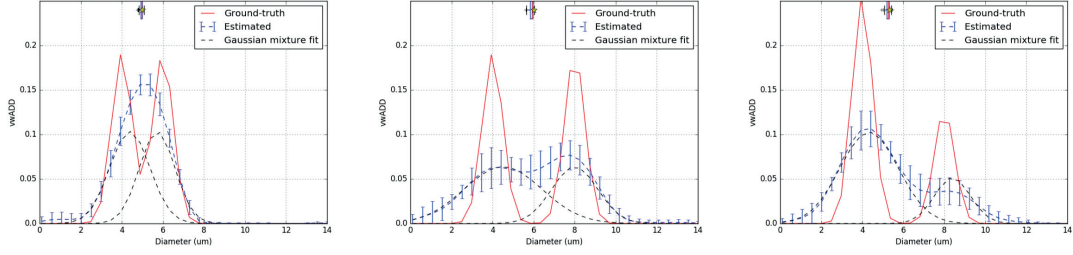


Figure 5.4 – Mean and variation of ADD coefficients obtained for bimodal distributions. Left: bimodal distribution with separation of $2\mu\text{m}$. Middle: bimodal distribution with separation of $4\mu\text{m}$. Right: bimodal distribution with separation of $4\mu\text{m}$ and decreased volume fraction for N_2 . All plots have a small boxplot on the top summarizing the estimated a' and the ground truth a (yellow star), illustrating the robustness of a' but also the gain of information provided by mapping the distribution instead of the mean diameter.

encoding). In the case of voxels containing crossing fascicles with different ADDs, the resulting measured distribution will be the weighted average of the two, which would be a bimodal distribution if the modes of the fascicles are separated enough.

In our experiments, bimodal reconstructions were distinguishable for sizes that were quite larger than the axon diameters observed in WM. Nevertheless, using such an approach for MRS might provide robust estimation of bimodal distribution for sizes comparable to the ones observed in WM, the diffusion coefficient of metabolites being smaller than the one of water (decreasing the diameter lower bound described by Nilsson et al. [69]). However, the protocol should be re-optimized for the corresponding diffusivity and the whole experiment conducted again in order to verify this.

5.4 Conclusions

Mapping ADD changes is challenging due to the ill-posedness of the problem [45, 13]. Our simulations show the feasibility of reconstructing non-parametric unimodal and bimodal distributions using a simple IA model based on PGSE. We showed the sensitivity of the method to population specific changes within bimodal distributions, as long as the two populations are separated by a minimal distance. Non-parametric and multi-modal ADD designs could therefore identify changes in ADD that are known to occur in development [23], and diseases like multiple sclerosis [28], providing specific characterization of neuronal tissue microstructure, which cannot be achieved by current mean diameter mapping techniques as ActiveAx_{MMWMD} [4] or parametric methods as AxCaliber [6]. Chapter 7 will explore whether the use of the protocol designed in this chapter improves robustness to the addition of the extra-axonal compartment (which might bias estimates and influence the diameter lower bound, as observed in Chapter 4).

6 Modeling hindered diffusion using HOTmix

Overview

In the previous two chapters, ADD estimates were shown to be less accurate when considering the EA compartment. In this chapter, we propose a new method to characterize the EA compartment, coined HOTmix, which we use to describe the EA signal for dMRI protocols at high b-values. A manuscript is in preparation to be submitted for peer-review to the Proceedings of the National Academy of Science (PNAS) (Publication 6).

6.1 Introduction

Models for axon diameter distribution like AxCaliber and ActiveAx_{MMWMD} assume that axons are perfectly parallel cylinders and take into account the diameter into their IA compartment, using a closed form solution [96, 38, 75]. Diffusion protocols with high gradient strengths, durations and separations are required in order to distinguish between different compositions of radii [30]. Unfortunately, there is no such closed form solution for the dMRI signal of the EA compartment. In fact, all WM tissue models cited above assume that the EA signal follows a gaussian diffusion model and that it can be characterized using a simple 2nd-order diffusion tensor.

Such a model is unlikely to be accurate for protocols that use various diffusion times and high b-values, as Burcaw et al. [18] showed that the EA space has time-dependent diffusivity and a non-gaussian behavior. If not modeled properly, this time dependence is thus likely to be captured by the IA model, biasing estimates. De Santis et al. [27] proposed to include time-dependence in the EA model and showed improved estimation of the mean diameter index, confirming the need to model correctly both compartments in order to recover meaningful estimates. The proposed model however has been designed for long diffusion times (ie. between 40 and 200 ms or more) only accessible through the use of STEAM dMRI sequences. Proper modeling of the EA time-dependence should be applied to shorter diffusion times in the case of the standard and widely used PGSE sequence. Other models for non-gaussian diffusion

include diffusion kurtosis imaging (DKI) [52, 66], as well as higher order tensors (HOT) [74, 64], but to our knowledge no study so far has reported benefits of using such models to model the EA space in particular.

The aim of this chapter is to propose a new model for the EA space, based on a mixture of higher order tensors (HOTmix). We present how the model is derived from the work of Liu et al. [64], and evaluate its performance to fit EA dMRI signals generated using MC simulations on a wide variety of virtual tissue samples. Fitting error is compared to the standard DT model as well as state-of-the-art non-gaussian models (KT and HOT). Correlation between estimated parameters and tissue properties are highlighted. The same procedure is then carried on using the dMRI signal acquired on a physical phantom composed of thick Dyneema fibers, mimicking the EA space.

6.2 Methods

6.2.1 Axi-symmetric HOT

Liu et al. [64] proposed the GDTI method, which approximates the dMRI signal as an expansion of 2nd and higher order tensors (HOT):

$$\begin{aligned} \ln(S/S_0) = & -b_{i_1 i_2}^{(2)} D_{i_1 i_2}^{(2)} + b_{i_1 i_2 i_3 i_4}^{(4)} D_{i_1 i_2 i_3 i_4}^{(4)} \\ & - \dots + (-1)^n b_{i_1 i_2 \dots i_{2n}}^{(2n)} D_{i_1 i_2 \dots i_{2n}}^{(2n)} \\ & + j(-b_{i_1 i_2 i_3}^{(3)} D_{i_1 i_2 i_3}^{(3)} + b_{i_1 i_2 i_3 i_4 i_5}^{(5)} D_{i_1 i_2 i_3 i_4 i_5}^{(5)} \\ & - \dots + (-1)^n b_{i_1 i_2 \dots i_{2n+1}}^{(2n+1)} D_{i_1 i_2 \dots i_{2n+1}}^{(2n+1)}), \end{aligned} \quad (6.1)$$

where the b-values are defined as:

$$b_{i_1 i_2 \dots i_n}^{(n)} = \gamma^n g_{i_1} g_{i_2} \dots g_{i_n} \delta^n \left(\Delta - \frac{n-1}{n+1} \delta \right),$$

and g_{i_n} is the component of the diffusion gradient along the i_n axis. The HOT model defined by Liu et al. uses a definition of the b-value which is different from the kurtosis model (and other higher tensor models in the literature). In diffusion kurtosis, the higher order b-value is the squared 2nd-order b-value, given by $b^2 = (\gamma G \delta)^4 (\Delta - \delta/3)^2$. The b-value proposed by Liu et al. adapts the expression of the term for diffusion time to each order. The HOT model has thus the potential to express both multi-exponential decay and time-dependent diffusion.

Truncating Equation 6.1 to order 2 gives the standard formula for DTI. Using the expansion up to the 4th order gives a model with 21 parameters to estimate: 6 for the 2nd order tensor and 15 for the 4th order tensor [64].

Before presenting the derivation of the HOTmix model, the expression given by Liu et al. was simplified by making a few assumptions. Considering the real part of a GDTI of order 4, the

signal is given by:

$$\ln(S/S_0) = -b_{i_1 i_2}^{(2)} D_{i_1 i_2}^{(2)} + b_{i_1 i_2 i_3 i_4}^{(4)} D_{i_1 i_2 i_3 i_4}^{(4)}. \quad (6.2)$$

By assuming that all cylinders are perfectly aligned along the z-axis (ie: the axial direction is $\mathbf{n} = \mathbf{e}_z$), the terms of the 2nd order tensor can be expressed as:

$$-b_{i_1 i_2}^{(2)} D_{i_1 i_2}^{(2)} = -b^{(2)} (D_{\parallel}^{(2)} \cos^2(\alpha) + D_{\perp}^{(2)} \sin^2(\alpha)),$$

where $b^{(2)} = \gamma^2 G^2 \delta^2 (\Delta - \delta/3)$ was the standard b-value, G the magnitude of the diffusion gradient and α the angle between \mathbf{n} and \mathbf{g} . Similarly, the terms of the 4th order tensor can be expressed as:

$$b_{i_1 i_2 i_3 i_4}^{(4)} D_{i_1 i_2 i_3 i_4}^{(4)} = b^{(4)} D_{\perp}^{(4)} \sin^4(\alpha),$$

where the 4th-order b-value is given by:

$$b_{i_1 i_2 i_3 i_4}^{(4)} = (\gamma G \delta)^4 (\Delta - \frac{3\delta}{5}).$$

Equation 6.2 then becomes:

$$\begin{aligned} \ln(S/S_0) = & -b^{(2)} D_{\parallel}^{(2)} \cos^2(\alpha) - b^{(2)} D_{\perp}^{(2)} \sin^2(\alpha) \\ & + b^{(4)} D_{\perp}^{(4)} \sin^4(\alpha). \end{aligned} \quad (6.3)$$

A detailed derivation is available in Appendix A.

6.2.2 Derivation of the HOTmix model

In addition to examining the benefits of using an axi-symmetric HOT model to characterize the EA compartment, a new model based on a mixture of axi-symmetric 4th order HOTs is considered. The model goes as follows:

$$S/S_0 = \sum_{i=1}^K w_i e^{-b^{(2)} D_{\parallel}^{(2)} \cos^2(\alpha) - b^{(2)} D_{\perp,i}^{(2)} \sin^2(\alpha) + b^{(4)} D_{\perp,i}^{(4)} \sin^4(\alpha)}. \quad (6.4)$$

Such a model is based on the assumption that a voxel is composed by a mixture of local microenvironments with different characteristics. Spins sample different microenvironments depending on their intrinsic diffusivity and their location in the voxel. Packets of spins sampling the same microenvironments will thus have an apparent $D_{\perp}^{(2)}$ and $D_{\perp}^{(4)}$ that is different from packets of spins sampling different microenvironments. Having an infinite number of possible $D_{\perp}^{(2)}$ and $D_{\perp}^{(4)}$, the dMRI signal can be expressed as:

$$S/S_0 = \iint P(D_{\perp}^{(2)}, D_{\perp}^{(4)}) e^{-b^{(2)} D_{\parallel}^{(2)} \cos^2(\alpha) - b^{(2)} D_{\perp}^{(2)} \sin^2(\alpha) + b^{(4)} D_{\perp}^{(4)} \sin^4(\alpha)} dD_{\perp}^{(2)} dD_{\perp}^{(4)}. \quad (6.5)$$

To estimate the distribution of $D_{\perp}^{(2)}$ and $D_{\perp}^{(4)}$ in the voxel, we discretized their values, which is equivalent to fit a discrete mixture of components, each one centered at a defined value of $D_{\perp}^{(2)}$ and $D_{\perp}^{(4)}$. The distribution of $D_{\perp}^{(2)}$ and $D_{\perp}^{(4)}$ is then estimated by recovering the weights w_i . Equation 6.4 can be linearized to:

$$Y = Dx \quad (6.6)$$

where Y is the normalized dMRI signal S/S_0 , $D \in \mathbb{R}^{m,k}$ is a dictionary or convolution operator with $M * N = K$ columns or atoms D_k encoding our forward-model and x are the weights w to be retrieved. The dictionary is build by sampling $M \times N$ combinations of $D_{\perp}^{(2)}$ and $D_{\perp}^{(4)}$. Results slightly improved when taking M linearly spaced samples of $D_{\perp}^{(2)}$ and $\sqrt{D_{\perp}^{(4)}}$. As shown after, the slight improvement provided by sampling $\sqrt{D_{\perp}^{(4)}}$ instead of $D_{\perp}^{(4)}$ might be due to the relationship between $D_{\perp}^{(4)}$ and the variance of the diffusivity pools.

6.2.3 Link with a mixture of gaussians with time-dependent variance

The HOT and HOTmix models use a 4th order b-value given by $b^{(4)} = (\gamma G \delta)^4 (\Delta - 3\delta/5)$ while other higher order tensors in the literature use powers of $b^{(4)}$ (e.g. the kurtosis tensor uses $(\gamma G \delta)^4 (\Delta - \delta/3)^2$). The perpendicular component of an axi-symmetric HOT is given by:

$$\ln(S_{\perp}/S_0) = -b^{(2)} D_{\perp}^{(2)} + b^{(4)} D_{\perp}^{(4)}. \quad (6.7)$$

Yablonskiy et al. [100] showed that the dMRI signal generated by a gaussian distribution of 2nd order tensors with mean diffusivity D_0 and variance σ^2 is given by:

$$\ln(S/S_0) = -b^{(2)} D_0 + \frac{1}{2} \sigma^2 b^{(2)2}, \quad (6.8)$$

when D_0 is much smaller than σ^2 . In this formulation, the 4th-order b-value is the squared 2nd-order b-value. By comparing Yablonskiy's formulation with the HOT tensor, a HOT tensor can be interpreted as being a gaussian distribution of radial diffusivities with mean μ and variance σ^2 equal to:

$$\mu = D_{\perp}^{(2)} \quad (6.9)$$

$$\sigma^2 = 2D_{\perp}^{(4)} \frac{(\Delta - \frac{3\delta}{5})}{(\Delta - \frac{\delta}{3})^2}. \quad (6.10)$$

The proposed HOTmix model being a mixture of HOT tensors, it can therefore be considered as a mixture model of such gaussians.

Westin et al. [99] show a relationship between the b-tensor used for encoding and the 4th and higher orders of the diffusion tensor. Acquiring the data using b-tensors might provide better estimates of the contribution of this higher order components.

In such statistical interpretation, the mean of the gaussian components does not vary with diffusion time. Time-dependent $D_{\perp}^{(2)}$ can be implemented by sampling different combinations of $D_{\infty}^{(2)}$ and A as formulated by De Santis et al. [18, 27]. Concerning WM substrates, adding time-dependence didn't improve significantly the reconstruction error, although a significant improvement was observed for substrates with an order of magnitude larger diameters, as shown hereafter.

6.2.4 Monte Carlo simulations

The radii of the cylinders used to create the virtual tissue samples were drawn from 22 gamma distributions corresponding to real WM samples [4, 1, 59]. For each gamma distribution, non-abutting cylinders were positioned randomly in three $500 \times 500 \times 500 \text{ um}^3$ voxels such that the intra-axonal volume fraction was 50%, 60% and 70% respectively, imposing periodicity at the voxel boundaries [40]. Our packing algorithm did not manage to achieve an IA volume fraction of 70% for 4 out of the 22 distributions (*i.e.* 22 different substrates with packing densities of 50% and 60% were generated while 18 substrates with packing densities of 70% were generated). The EA dMRI signal of each substrate was computed using an in-house dMRI MC Simulator [81]. One million spins were positioned in the EA space and let to diffuse in the synthetic tissue while running our dMRI experiments, with spins elastically reflected by the cylinder walls. Spin's intrinsic diffusivity was set to $0.6 \times 10^{-3} \text{ mm}^2/\text{s}$ to mimick ex vivo WM samples, and to $2.0 \times 10^{-3} \text{ mm}^2/\text{s}$ to mimick in vivo WM samples [4]. Figure 6.1 illustrates the process for 2 different virtual tissue samples.

For ex vivo signals, the diffusion protocol consisted of three different sets of b-values ranging from 1'000 to 16'000 s/mm^2 , with steps of 500 s/mm^2 . Each set of b-values was obtained by either varying the gradient amplitude G , the gradient separation Δ or the gradient duration δ , while keeping the other two parameters constant. The b-value set with varying Δ started at 2'500 s/mm^2 , as shorter diffusion times could not be implemented on the preclinical scanner (see section on MRI acquisition and processing). The Echo Time (TE) was fixed to 65ms. Models were fit using a selection of 9 shells, whose parameters are summarized in Table 6.1. For in vivo signals, the same protocol was used with b-values up to 6'000 s/mm^2 , as higher b-values led to signals with amplitude lower than $1\text{e-}4$. The 9 shells used for model fitting are summarized in Table 6.2.

6.2.5 Fitting perpendicular signals

Focus was first placed on the reconstruction of the perpendicular signal as a function of b-value. Models were fit using either the noiseless signal, or 50 noisy realisations with SNR=30. Rician bias was removed [55] and the signal denoised [97] before model fitting. When considering the perpendicular signal only, the different axi-symmetric tensor models that were used

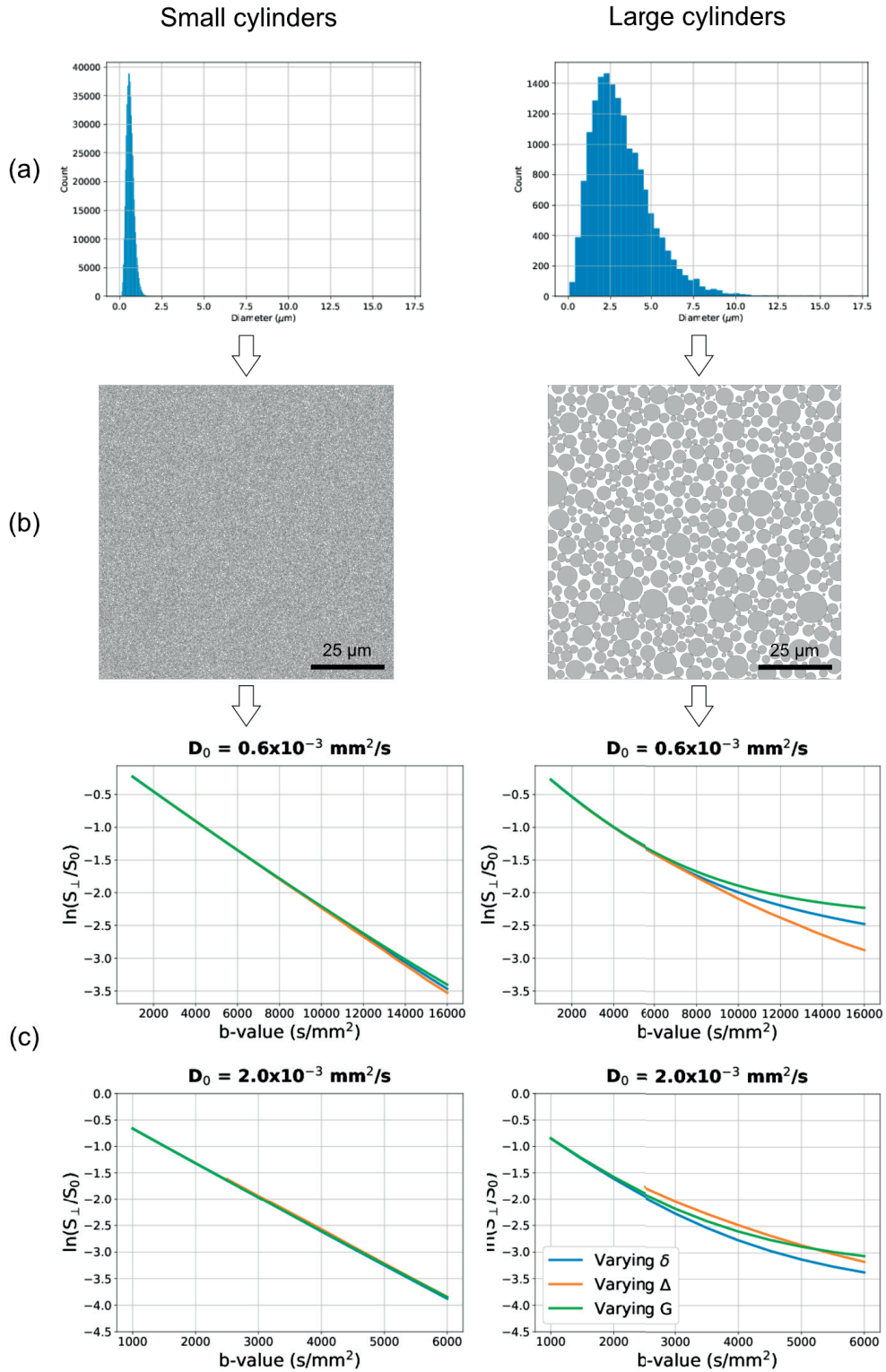


Figure 6.1 – Illustration of the pipeline used to generate EA dMRI signals for 2 different virtual samples with IA volume fractions of 0.7. (a) Cylinder diameter distribution; (b) cylinder positions (only a $100 \times 100 \mu\text{m}^2$ section is shown for visibility); (c) MC generated dMRI signals. Left: 489'691 radii $\in \Gamma(8.5, 3.7\text{E-}8)$. Right: 16'589 radii $\in \Gamma(3.2, 4.9\text{E-}7)$.

Table 6.1 – dMRI protocol for $D_0 = 0.6 \times 10^{-3} \text{mm}^2/\text{s}$

	G (mT/m)	Δ (ms)	δ (ms)	b-value (s/mm ²)
Varying G {	127.0	20.0	7.0	1'000
	359.3	20.0	7.0	8'000
	508.2	20.0	7.0	16'000
Varying Δ {	550.0	9.5	3.75	2'500
	550.0	27.5	3.75	8'000
	550.0	53.8	3.75	16'000
Varying δ {	114.4	32.4	5.9	1'000
	114.4	32.4	18.0	8'000
	114.4	32.4	27	16'000

Table 6.2 – dMRI protocol for $D_0 = 2.0 \times 10^{-3} \text{mm}^2/\text{s}$

	G (mT/m)	Δ (ms)	δ (ms)	b-value (s/mm ²)
Varying G {	127.0	20.0	7.0	1'000
	220.1	20.0	7.0	3'000
	311.2	20.0	7.0	6'000
Varying Δ {	550.0	11.1	3.75	3'000
	550.0	21.0	3.75	6'000
Varying δ {	114.4	32.4	5.9	1'000
	114.4	32.4	10.5	3'000
	114.4	32.4	15.3	6'000

(DT, KT and HOT) were simplified to the following linear expression:

$$\ln\left(\frac{S_{\perp}}{S_0}\right) = Bx, \quad (6.11)$$

where S_{\perp} is the perpendicular signal simulated for the different b-values in the protocol. The model parameters x were estimated by solving $\operatorname{argmin}_{x \geq 0} \left\| \ln\left(\frac{S_{\perp}}{S_0}\right) - Bx \right\|_2$. For the HOTmix model, its parameters were estimated by solving $\operatorname{argmin}_{x \geq 0} \left\| \frac{S_{\perp}}{S_0} - Dx \right\|_2$. The matrix B or D and coefficients x changed depending on the model, as follows.

Diffusion Tensor model

$$B = [-b^{(2)}] \quad (6.12)$$

$$x = [D_{\perp}^{(2)}] \quad (6.13)$$

Kurtosis model

$$B = \begin{bmatrix} -b^{(2)} & \frac{1}{6}(b^{(2)})^2 \end{bmatrix} \quad (6.14)$$

$$x = \begin{bmatrix} D_{\perp}^{(2)} & K \end{bmatrix}^T \quad (6.15)$$

Higher order tensor

$$B = \begin{bmatrix} -b^{(2)} & b^{(4)} \end{bmatrix} \quad (6.16)$$

$$x = \begin{bmatrix} D_{\perp}^{(2)} & D_{\perp}^{(4)} \end{bmatrix}^T \quad (6.17)$$

HOTmix model

$$D = \begin{bmatrix} e^{-b^{(2)}D_1^{(2)} + b^{(4)}D_1^{(4)}} & e^{-b^{(2)}D_1^{(2)} + b^{(4)}D_2^{(4)}} & \dots & e^{-b^{(2)}D_M^{(2)} + b^{(4)}D_N^{(4)}} \end{bmatrix} \quad (6.18)$$

$$x = \begin{bmatrix} w_1 & w_2 & \dots & w_{M \times N} \end{bmatrix}^T \quad (6.19)$$

6.2.6 Fitting of 3D signals

As fiber orientation in real brain tissue is usually unknown, reconstruction performance was also assessed on 3D signals. In this case, each shell in Table 6.1 was acquired in 60 directions homogeneously covering the unit sphere [20]. To avoid numerical instability when working

with the noiseless signal, in particular along the parallel direction, signal values lower than free diffusion were ignored during the fit. Regarding noisy signals, Rician bias was removed [55] and the signal denoised [97] before model fitting. For tensor fitting, negative values were ignored during the fit, while all values were considered for the fitting of HOTmix. SNR was set to 30 for ex vivo samples. As diffusivity is higher for in vivo samples, signal amplitude was lower for in vivo samples, in particular for samples in the parallel direction. We chose to use an SNR of 60 for in-vivo samples, to decrease the number of dMRI samples that were below the noise floor. This concerns signal samples that are parallel to the cylinders, as the signal as a function of the b-value decays the fastest in this direction. For a SNR of 30, most of shells' samples are below the noise floor, meaning the reconstruction method would fit more noise than real signal. Although a SNR of 60 is unrealistic for a single acquisition, averaging 4 volumes acquired with a SNR of 30 would be equivalent. We considered that increased scan time was a fair compromise in order to get a reliable signal to fit. For all models, the main orientation and parallel diffusivity $D_{\parallel}^{(2)}$ were estimated by fitting an axi-symmetric DT to the 3 shells with b-value lower than 3'000 s/mm². The remaining parameters of the different axi-symmetric tensor models were estimated by solving $\text{argmin}_{x \geq 0} \left\| \ln\left(\frac{S_{\perp}}{S_0}\right) + b^{(2)} D_{\parallel}^{(2)} \cos^2(\alpha) - Bx \right\|_2$. For the HOTmix model, its parameters were estimated by solving $\text{argmin}_{x \geq 0} \left\| \frac{S_{\perp}}{S_0} - Dx \right\|_2$. The matrix rows B_r or D_r and coefficients x changed depending on the model, as follows. The angle α represents the angle between the gradient direction and the estimated direction of the cylinders.

Diffusion Tensor model

$$B = [-b^{(2)} \sin^2(\alpha)] \quad (6.20)$$

$$x = [D_{\perp}^{(2)}] \quad (6.21)$$

Kurtosis model

$$B = \begin{bmatrix} -b^{(2)} \sin^2(\alpha) & \frac{1}{6}(b^{(2)})^2 \sin^4(\alpha) \end{bmatrix} \quad (6.22)$$

$$x = \begin{bmatrix} D_{\perp}^{(2)} & K \end{bmatrix}^T \quad (6.23)$$

Higher order tensor

$$B = \begin{bmatrix} -b^{(2)} \sin^2(\alpha) & b^{(4)} \sin^4(\alpha) \end{bmatrix} \quad (6.24)$$

$$x = \begin{bmatrix} D_{\perp}^{(2)} & D_{\perp}^{(4)} \end{bmatrix}^T \quad (6.25)$$

HOTmix model

$$D = \left[e^{-b^{(2)}(D_{\parallel}^{(2)} \cos^2(\alpha) + D_{\perp,1}^{(2)} \sin^2(\alpha)) + b^{(4)} D_{\perp,1}^{(4)} \sin^4(\alpha)} \quad \dots \quad e^{-b^{(2)}(D_{\parallel}^{(2)} \cos^2(\alpha) + D_{\perp,M}^{(2)} \sin^2(\alpha)) + b^{(4)} D_{\perp,N}^{(4)} \sin^4(\alpha)} \right] \quad (6.26)$$

$$x = \begin{bmatrix} w_1 & w_2 & \dots & w_{M \times N} \end{bmatrix}^T \quad (6.27)$$

6.2.7 HOTmix parameters and substrate properties

Spins in the EA space might carry microstructural information like the mean axon outer diameter, or axonal packing density. To verify whether microstructural features could be extracted from the HOTmix parameters, substrate features were computed from the position and sizes of the cylinders and compared to values extracted from HOTmix parameters.

The first microstructural feature that was tested was the IA volume fraction. According to the tortuosity constraint used in ActiveAx_{MMWMD} [4, 25], the IA volume fraction can be computed from the estimated 2nd-order parallel and perpendicular diffusivity: $IAVF = (D_{\parallel}^{(2)} - \bar{D}_{\perp}^{(2)}) / D_{\parallel}^{(2)}$. Here, $\bar{D}_{\perp}^{(2)}$ was the weighted average of the 2nd-order perpendicular diffusivities returned by the HOTmix model. The estimated IA volume fraction was computed using the previous equation, and compared to the ground-truth value used to design the substrates.

Secondly, the average 2nd-order perpendicular diffusivity was compared to the volume weighted mean diameter of the substrates.

Finally, the weighted average standard-deviation of the diffusivity pools for the shortest diffusion time was also computed and compared to the standard deviation of the cylinder diameters in the substrate. The shortest time was used as longer diffusion times have a blurring or "coarse-graining" effect [73].

6.2.8 Dyneema phantom

Three physical phantoms made of dyneema fibers were build following the procedure presented by Fieremans et al. [37]. Two types of yarn where used: the "SK99" and the "SK78", made of filaments of 10 μm and 20 μm in diameter respectively.

As the yarn had a diameter that was almost an order of magnitude higher than the ones used in the simulations, we created two substrates with diameters corresponding to Dyneema fibers, using a normal distribution with mean μ of 10 μm or 20 μm and standard deviation $\sigma = 0.2 \times \mu$. A third substrate was build using a mix of 10 μm and 20 μm cylinders, such that the volume of both populations was equal. The packing density was set to 70%. HOTmix with HOT components of order 4 was unable to fit the generated signal: it didn't capture the 3 different curves (potentially due to the higher diameter of the cylinders compared to the ones used in

Table 6.3 – Composition of dyneema phantoms

	SK99	SK78	Mix-SK99-SK78
# filaments of SK99	251680	-	125840
# filaments of SK78	-	63180	31590
Outer diameter after shrinkage	8.8	7.7	8.1
Inner diameter after shrinkage	7.06	5.74	6.36
Estimated hindered volume fraction	0.49	0.23	0.38

WM mimicking substrates). We extended the HOTmix model to include time-dependence in the 2nd-order perpendicular diffusivity [18, 27]. This involved replacing the atoms in the dictionary corresponding to $D_{\perp}^{(2)}$ with combinations of $D_{\infty}^{(2)}$ and A , two parameters related to the bulk diffusivity at infinite diffusion time and the correlation length of the EA space, respectively [18, 27]. Fitting improved drastically compared to the simple HOTmix model.

The physical phantoms composition is summarized in Table 6.3. For each phantom, the fibers were placed inside a transparent shrinking tube (Tyco Electronics, ref RNF-3000-18/6-X) underwater. Water was heated up to 90°C for initial shrinking. The tubes were taken out of the water and heated up to around 200°C using a heat gun, for the tube to shrink to their maximum. Shrunk tubes were placed underwater again, and remaining bubbles removed using the degazing program of a Branson (Danbury, United States) ultrasonic device. The phantoms were placed in hot water (60°C) during 24h for the water to diffuse and wet all the filaments. The phantoms were then cooled down to room temperature overnight and placed in the same plastic tube using a 3D printed holder. The plastic tube was then closed (Figure 6.2) and remaining air bubbles were removed using a 2nd session of degazing before MR acquisition.

6.2.9 MRI acquisition and processing

The phantoms were placed in a 4cm volume coil and scanned using a 7T Bruker preclinical scanner. Air-flow at room temperature was used to regulate the sample temperature during the whole acquisition. Temperature was monitored and fluctuated from 25.2°C to 27.7°C with a mean and standard deviation of 26.2±0.52°C. First, a high resolution T2-weighted image was acquired to check for remaining air bubbles, which were found to be negligible (Figure 6.3). The main orientation of the fibers was computed using a DTI acquisition with b-value of 1'000 acquired over 60 directions. The main orientation was determined by fitting the DTI model in all voxels inside the phantoms and averaging all the first eigen-vectors. The subsequent diffusion weighted images were then acquired in 3 directions on the plane perpendicular to the fibers. The PGSE parameters of the DWI images were set to be the same as for the protocol used in the MC simulations (ie more or less 31 b-values acquired by either varying G , Δ or δ). Imaging parameters are summarized in Table 6.4. Eight separate b0 images were acquired at regular intervals between the DWI volumes. All PGSE volume were corrected

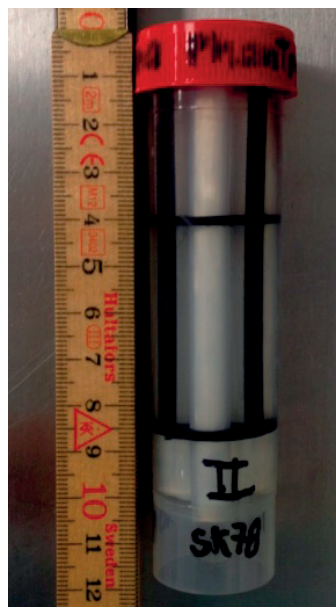


Figure 6.2 – Dyneema phantoms in closed plastic tube before MRI acquisition.

Table 6.4 – Imaging parameters for MRI acquisitions

	TurboRARE	PGSE
FoV	64x64mm ²	40x40mm ²
Image size	512x512	64x64
Slice thickness	1.3mm	1.3mm
Resolution	0.078125x0.078125x1.3mm	1x1x1.3mm
Number of slices	30	30
Repetition time	10s	5s
Echo time		65.026ms

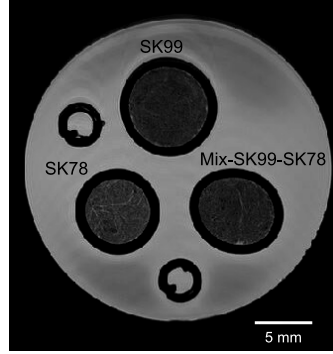


Figure 6.3 – High resolution T2 weighted scan of the dyneema phantoms.

for gibbs ringing [56]. The signal for each phantom was computed by averaging over the 3 perpendicular directions, normalizing to the mean b_0 volume and averaging over all voxels inside the corresponding phantom. HOTmix with time-dependent $D_{\perp}^{(2)}$ was fitted to the data.

6.3 Results

6.3.1 Ex vivo WM signals

All models were first evaluated using the noiseless perpendicular signal. Plots showing the reconstructed perpendicular signal compared to the ground truth are shown in Figure 6.4, for the two substrates shown in Figure 6.1. The fit was done using 9 samples: 3 samples of each of the 3 curves simultaneously (smallest, intermediate and highest b -value of each of the three curves). The reconstructed signal was then computed from the fit for all intermediate values, for comparison with the ground-truth signal. The DT model can only fit a line to the log of the perpendicular signal, and was therefore unable to capture the curvature nor the differences between curves. By estimating the diffusion kurtosis, the KT model was able to capture the curve of the signal. However, the formulation presented by Jensen et al. [52] assumes that the diffusion time remains constant in order to estimate $K(\Delta)$. As the same model was used to fit a protocol where all G , Δ and δ were changing, the model was unable to fit the 3 different curves at the same time. The HOT model was able to distinguish the 3 different curves, but not with the required curvature (higher order tensors might be required). Finally, the HOTmix model was able to capture the curvature of the 3 different curves simultaneously. The HOTmix model had the lowest reconstruction error over all generated ex vivo WM signals. Fitting error over all substrates are shown in Figure 6.5. Figure 6.5a summarizes the fitting error for the noiseless perpendicular signal. As fiber orientation in real brain tissue is usually unknown, reconstruction performance was also assessed on 3D signals (Figure 6.5b). The HOTmix model was also the one that best reconstructed the EA dMRI signal from noisy samples. Figure 6.5b and Figure 6.5c summarize the distribution of the reconstruction error for the different models when the perpendicular and the 3D dMRI signals were contaminated

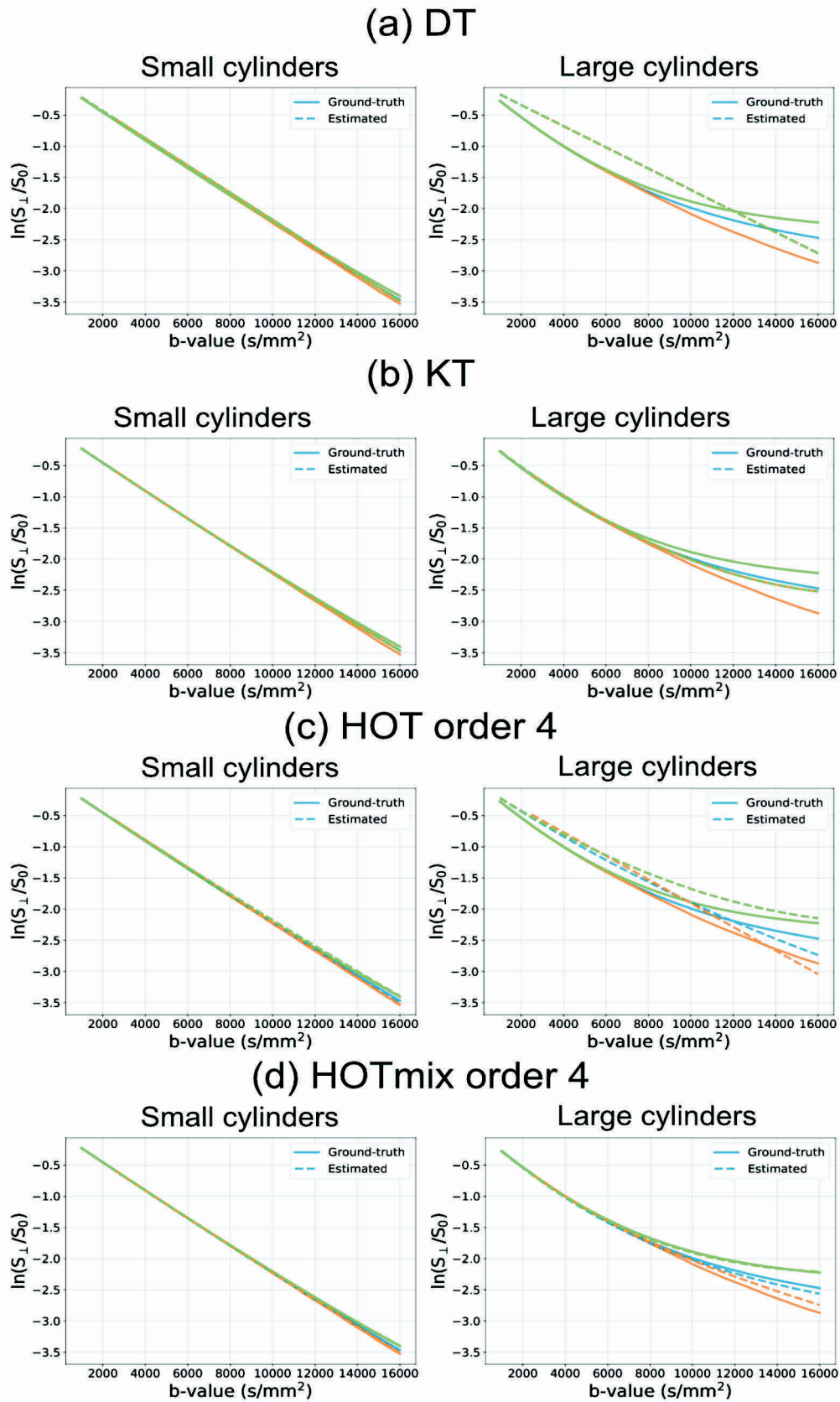


Figure 6.4 – Reconstructed signals (dotted lines) overlapped with the ground-truth (full lines) when using (a) DT, (b) KT, (c) single HOT tensor, and (d) HOTmix (mixture of HOTs, proposed method). Green, orange and blue represent varying-G, varying- Δ , and varying- δ , respectively (as in Figure 6.1). The substrate with smallest (left) and highest (right) mean cylinder size are shown.

with Rician noise corresponding to an SNR of 30. As mentioned earlier, including a time-

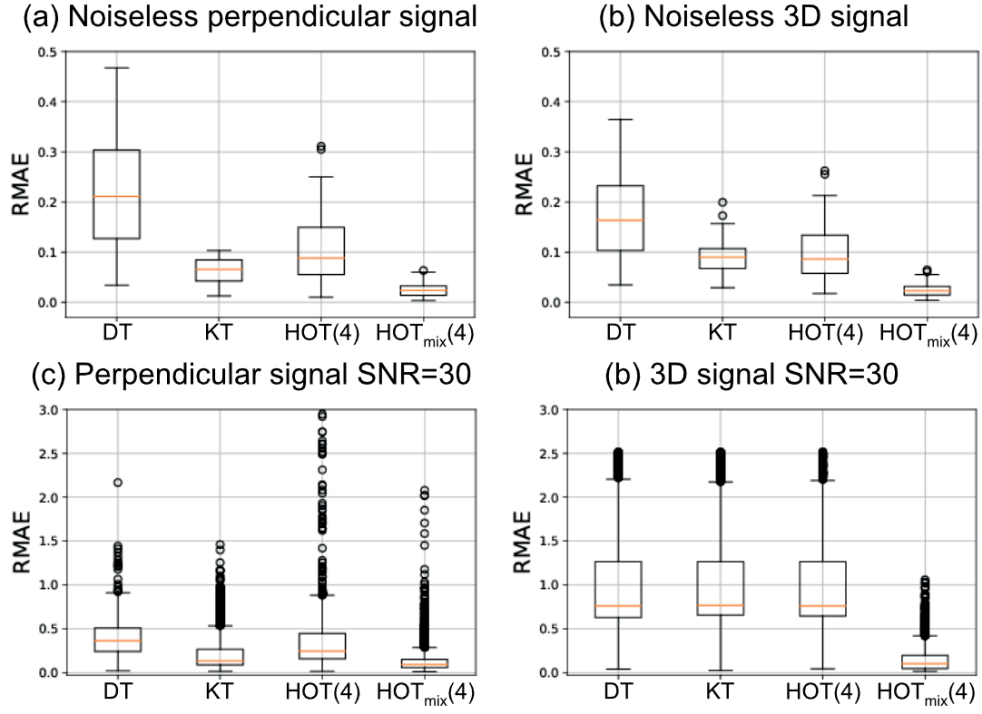


Figure 6.5 – Fitting error for different models used on (a) the noiseless ex vivo perpendicular signal, (b) the noiseless ex vivo 3D signal, and (c) the noisy ex vivo 3D signal. DTI: Diffusion Tensor Imaging, DKI: Diffusion Kurtosis Imaging, HOT(4): Higher Order Tensor of order 4. HOT_{mix}(4): mixture of Higher Order Tensors of order 4 (proposed method). RMAE: Relative Mean Absolute Error.

dependent $D_{\perp}^{(2)}$ term as proposed by De Santis et al.[27, 18] didn't significantly improve the reconstruction error. Regarding the substrate with largest distribution of cylinders, computing the average mean-square displacement of the center of mass of the spins between the two gradient pulses showed that the instantaneous diffusivity was of $0.29 \text{ mm}^2/\text{s}$ for a diffusion time $t = 8.2\text{ms}$, $0.28 \text{ mm}^2/\text{s}$ for $t = 29.5\text{ms}$, and $0.27 \text{ mm}^2/\text{s}$ for $t = 52.5\text{ms}$.

6.3.2 HOTmix parameters and substrate properties

A summary of HOTmix parameter values for two substrates is shown in Figure 6.6.

Parameters estimated from the weights of HOTmix on the noiseless 3D signal were compared to substrate properties and are summarized in Figure 6.7. The IA volume fraction was underestimated on average by 8, 11.5 and 14 percentage points for volume fractions of 50%, 60% and 70% respectively (6.7a). This underestimation matches the underestimation presented by Novikov and Fieremans [72] for substrates with high IA volume fractions. The size of the cylinders seemed to have an influence on the estimated IA volume fraction, as substrates with bigger cylinders had a lower estimated IA volume fractions. As the signal of a tensor with

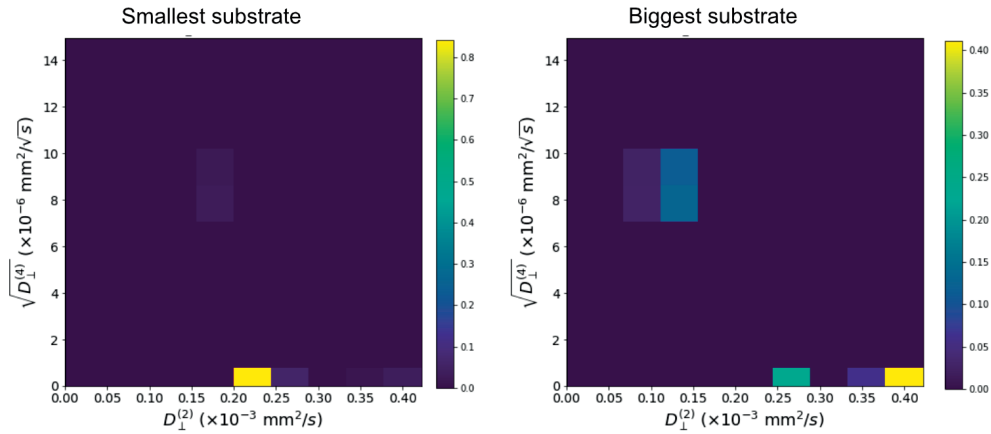


Figure 6.6 – HOTmix parameter values for two substrates used in the study, using their noiseless 3D signals.

low perpendicular diffusivity is closer to the signal of a large cylinder than a small cylinder, contributions of large cylinders might be confused with hindered diffusion and captured by the tensors with low diffusivity. If that's the case, the EA volume fraction would increase, and the estimated IA volume fraction decrease, explaining our observations regarding substrates with large diameters.

The mean 2nd-order perpendicular diffusivity was clearly related to the substrate's mean volume weighted diameter as well as the IA volume fractions (Figure 6.7b). Plotting the mean 2nd-order perpendicular diffusivity against the log of the diameter showed 3 different lines, with slope and offset that depended on the IA volume fraction.

The average standard deviation of the diffusivity pools was also influenced by both the IA volume fraction and the standard deviation of the diameters in the substrates (Figure 6.7c). While there was little correlation between the variance of the diffusivity pools and the variance of the diameters for substrates with IA volume fractions of 50%, there was a very high correlation for substrates with IA volume fractions of 70% (pearson correlation coefficient of 0.98, $p < 1e-9$). This is likely explained by the variance of the cylinder diameters driving most of the variance of the diffusivity pools in the EA space when the packing density is high. At lower packing densities, the relationship is less clear, but a pattern was still observable.

6.3.3 In vivo WM signals

Figure 6.8 shows the reconstructions obtained using the noiseless perpendicular signal for two substrates.

Reconstruction error over all substrates are summarized in Figure 6.9. Results include fitting error for the noiseless perpendicular signals (Figure 6.9a), the noiseless 3D signals (Figure 6.9b), the noisy perpendicular signals (Figure 6.9c) and noisy 3D signals (Figure 6.9d). The HOTmix

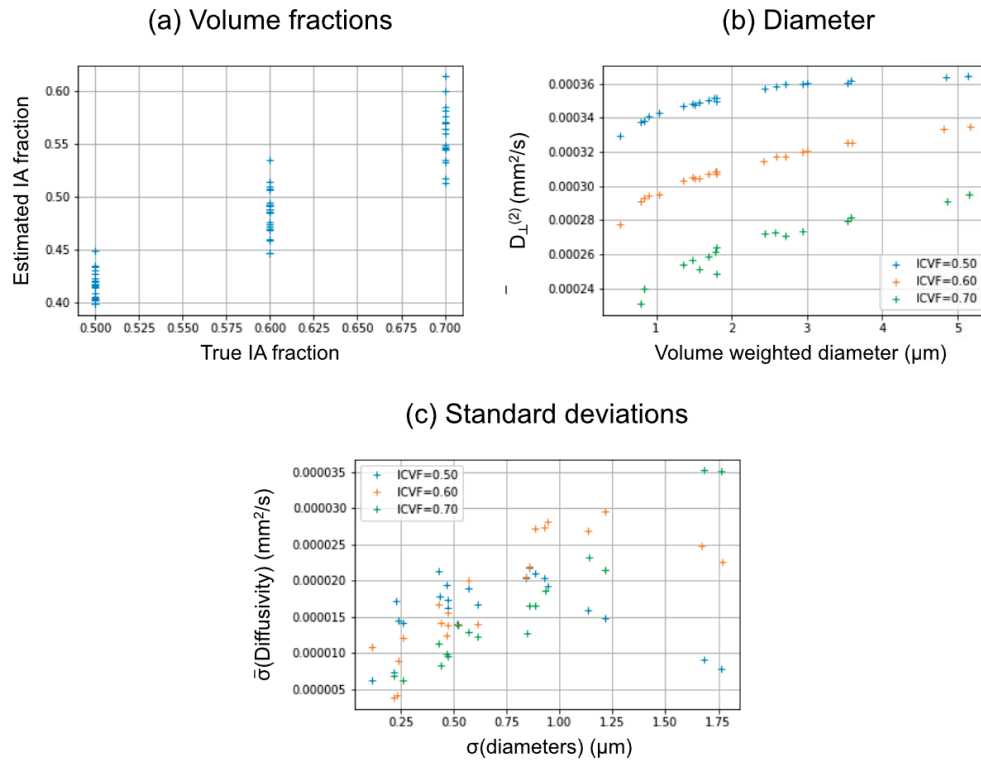


Figure 6.7 – HOTmix features compared to substrate properties. (a) Estimated IA volume fraction inspired from the tortuosity model in [4] compared to the ground-truth IA volume fraction. (b) Relationship between the mean 2nd-order perpendicular diffusivity estimated from HOTmix and the volume weighted diameter. (c) Average standard deviation of diffusivity pools estimated from HOTmix and compared to the standard deviation of the radii in the substrate.

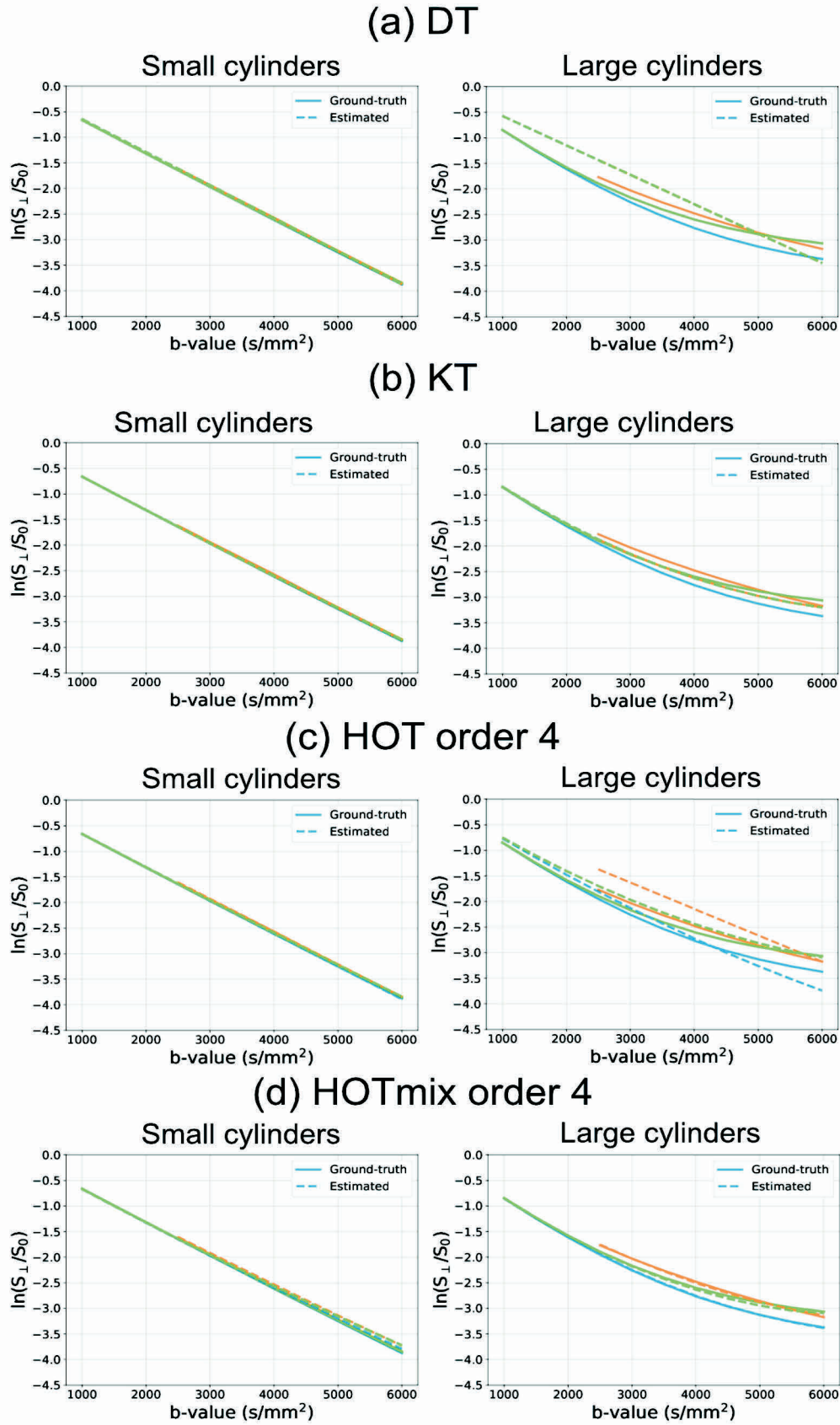


Figure 6.8 – Reconstructed signals (dotted lines) overlapped with the corresponding ground-truth (full lines) for two in vivo substrates. Green, orange and blue represent varying-G, varying- Δ , and varying- δ , respectively.

model had the lowest reconstruction error for all simulated signals.

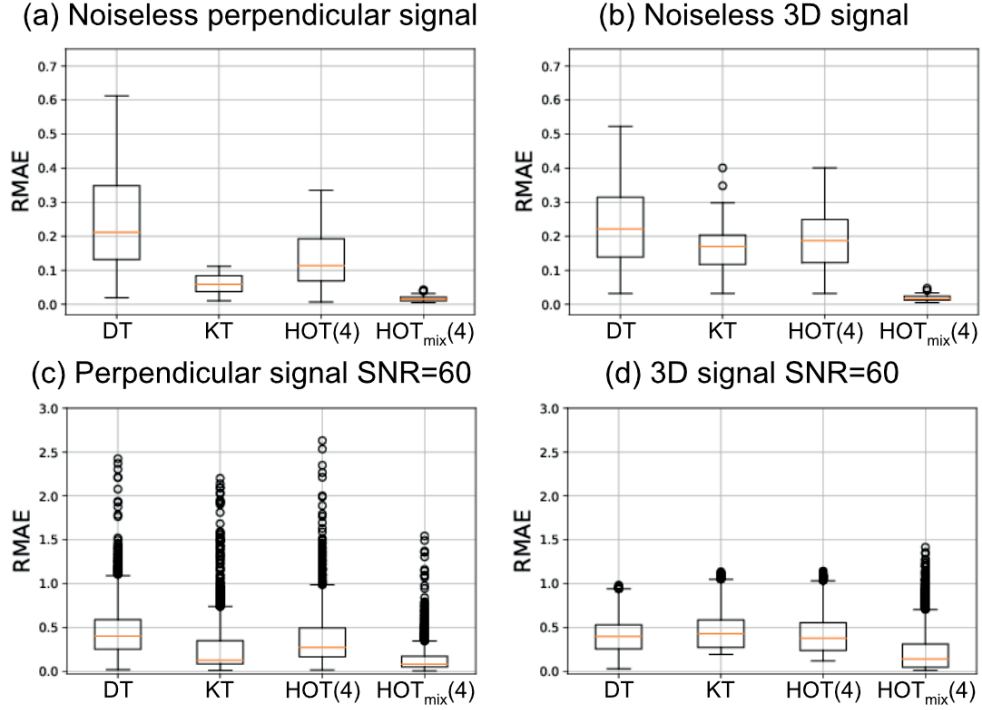


Figure 6.9 – Fitting error of different models used on in vivo signals (a) noiseless perpendicular signal, (b) the noiseless 3D signal, and (c) perpendicular signal with SNR = 350. DT: Diffusion Tensor, DK: Diffusion Kurtosis, HOT(4): Higher Order Tensor of order 4, HOTmix(4): mixture of Higher Order Tensors of order 4 (proposed method). RMAE: Relative Mean Absolute Error.

6.3.4 Dyneema phantom

Reconstructed signals using MC simulations for the Dyneema phantom are shown in Figure 6.10. HOTmix without a time-dependent $D_{\perp}^{(2)}$ term was unable to distinguish the 3 different curves (1st row). However, including time dependence as proposed by De Santis et al. [27, 18] did improve the reconstruction accuracy (2nd row). When considering the simulations for the SK99 fiber (mean diameter of $10\mu\text{m}$), computing the instantaneous diffusivity from the mean square displacement of the spin's center of mass between the two diffusion pulses resulted in a diffusivity of $0.97 \times 10^{-3} \text{ mm}^2/\text{s}$ for $t=4.7\text{ms}$, $0.84 \times 10^{-3} \text{ mm}^2/\text{s}$ for $t=28.5\text{ms}$ and $0.80 \times 10^{-3} \text{ mm}^2/\text{s}$ for $t=50.7\text{ms}$. For the SK78 fiber, the instantaneous diffusivity was $1.19 \times 10^{-3} \text{ mm}^2/\text{s}$, $1.0 \times 10^{-3} \text{ mm}^2/\text{s}$, and $0.94 \times 10^{-3} \text{ mm}^2/\text{s}$ for diffusion times of 4.7 ms, 28.5 ms and 50.7 ms, respectively. For all simulations, the parallel instantaneous diffusivity was estimated to be $2.0 \times 10^{-3} \text{ mm}^2/\text{s}$ (which corresponds to the intrinsic diffusivity), and remained constant over diffusion times, providing confidence on the reliability of the estimated instantaneous diffusivity.

The acquired signal using the physical Dyneema phantom is shown in Figure 6.11 along

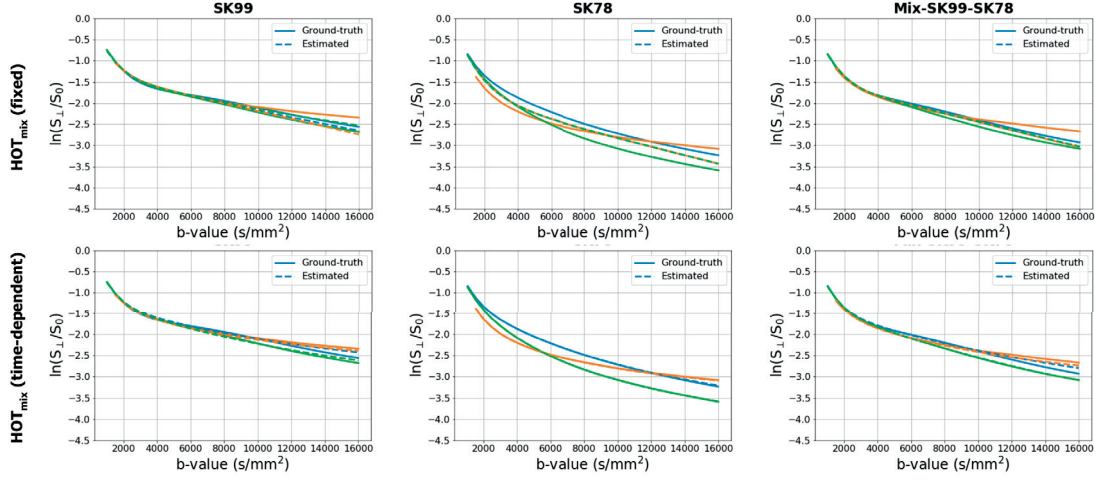


Figure 6.10 – Reconstruction of MC simulated Dyneema phantom signals. HOTmix is either used with HOTs of order 4 with fixed $D_{\perp}^{(2)}$ (first row), or time-varying $D_{\perp}^{(2)}$ (2nd row).

with the reconstructed signal using HOTmix. The behavior of HOTmix was similar to the observations made for the MC simulated signal: the basic HOTmix model with fixed $D_{\perp}^{(2)}$ failed to reconstruct the three curves while the formulation with time-dependent perpendicular diffusivity significantly improved the quality of the fit. This highlights the importance of including time-dependence when modeling the EA compartment in phantoms made of Dyneema fibers [37].

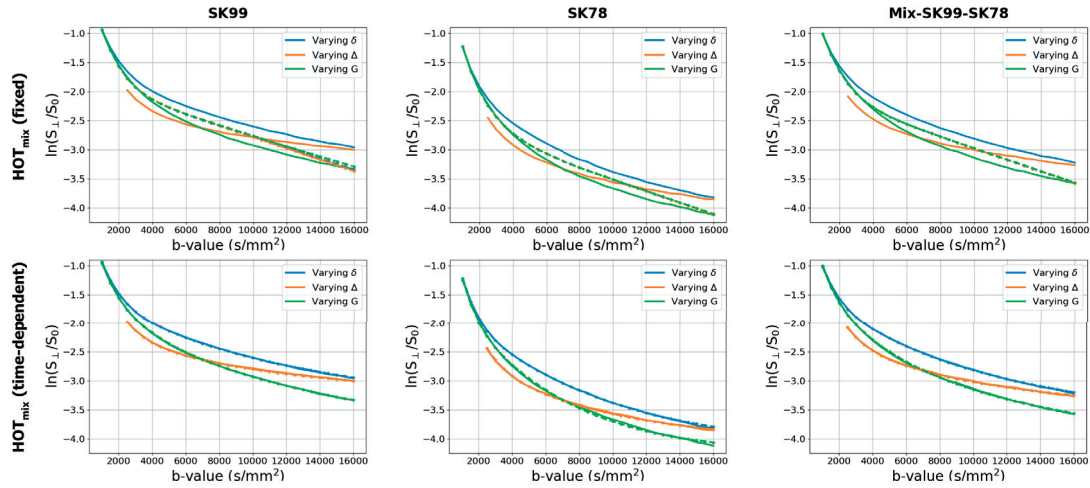


Figure 6.11 – Reconstruction of Dyneema phantom signals. HOTmix is either used with HOTs of order 4 with fixed $D_{\perp}^{(2)}$ (first row), or time-varying $D_{\perp}^{(2)}$ (2nd row), significantly improving the quality of the fit, as expected from MC simulations.

6.4 Discussion

Our experiments showed that the HOTmix model improves the reconstruction of the EA signal compared to single tensor models like the DT, KT and HOT. In simulations, the model adapts to the shape of the EA signal for a wide variety of distributions inspired from histology [59, 1, 4, 31], for both the tested ex vivo and in vivo protocols. The methods also shows robust signal reconstruction even in the presence of noise.

In terms of physical interpretation, HOTmix corresponds to a weighted sum of higher order tensors. It can be interpreted as the reconstruction of a distribution of tensors, which raises from packets of spins sampling different local microenvironments, similar to the DIAMOND model [86]. HOTmix differs mainly because no particular distribution shape is imposed, nor the number of peaks. HOTmix is also proposed to model hindered diffusion in particular, while DIAMOND was proposed as a generic model to capture all restricted, hindered and isotropic diffusion tensors. HOTmix is only composed of tensors that are anisotropic, with a parallel diffusivity which is set to the spins estimated intrinsic diffusivity (as there is no hindrance in the parallel direction when considering hollow cylinders). The perpendicular diffusivity on the other hand is lower, due to the hindrance caused by the cylinder walls. Each tensor has a different apparent 2nd-order perpendicular diffusivity, as well as a 4th-order perpendicular diffusivity, depending on the local microenvironment sampled by the spins. The inclusion of higher order diffusivities makes it able to capture local non-gaussian behaviors, as opposed to a distribution of 2nd-order tensors only [100]. The use of the higher order b-value defined by Liu et al. [64] also makes it able to distinguish the effect of the gradient amplitude G , separation Δ and duration δ (up to a certain limit). This feature is not the case for the DT or KT, as only a single signal can be generated for a given b-value, while the simulated signals show a different behavior when different G , Δ or δ are used.

The HOTmix model can be interpreted as the reconstruction of a distribution of diffusivities using a mixture of gaussians. In the formulation used for WM, it appeared that the mean of such gaussians was not required to vary with diffusion time, as suggested by Burcaw et al. [18], in order to provide accurate signal reconstruction. For the diffusion times used in our simulations, and the distribution of cylinder diameters present in the WM mimicking substrates, it appeared that the instantaneous diffusivity remained stable over time. This goes in line with the observations of Burcaw et al. [18], in particular in Figure 11, where $D(t) - D_\infty$ is very close to zero for diffusion times between 10ms and 100ms, when considering WM substrates. As shown by Figures 11a and 11c in Burcaw et al. [18], the importance of time-dependent diffusivity decreases for smaller diameters. Indeed, for a given diffusion time, as A is related to the EA characteristic length and the axon diameters, a decrease in mean diameter lowers the value of A which in turn brings the instantaneous diffusivity closer to D_∞ . As no myelin sheet was included in our substrates, the spins in the EA space of our experiments probed cylinder diameters that were smaller compared to the simulations presented by Burcaw et al [18], decreasing the importance of including a time-varying factor. However, regarding the dyneema phantom, as diameters are an order of magnitude larger, including a time-dependent

term for the 2nd-order diffusivity significantly improved reconstruction results. The presence of time-dependent diffusivity was confirmed by computing the instantaneous diffusivity at different diffusion times using the mean squared displacement between the center of masses of the spins during the two diffusion pulses. The instantaneous diffusivity was observed to decrease significantly with diffusion time, illustrating the need to account for time-dependent diffusivity in the HOTmix model. This again goes in line with observations presented by Burcaw et al [18], in particular Figure 6a, where the perpendicular instantaneous diffusivity of water in a dyneema phantom greatly varies for diffusion times between 0 and 200ms.

As pointed out by Burcaw et al. [18] and De Santis et al. [27], modeling inaccuracies in the EA compartment might result in a "residual" that might be captured by the IA compartment, biasing estimated microstructural features. In the case of ADD estimation, this might be a potential source of the bias observed in Chapters 4 and 5. Our simulations indicate that varying the protocol parameters G , Δ and δ have different effects on the EA signal for the exact same b-value. At least two parameters change between shells used in protocols for ADD or mean diameter estimation [6, 4, 31, 30], or to optimize sensitivity to a set of diameters (see Chapter 5). The HOTmix model might prove to be useful in the context of ADD estimation by capturing the shape of the EA signal with better accuracy compared to the EA models used previously. Experiments exploring the use of the HOTmix model for ADD mapping are presented in the next chapter.

Our experiments also indicate that parameters from the HOTmix model are related to microstructural features like the IA volume fraction or the mean diameter index and the standard deviation of the cylinder diameters. Such observations might be exploited in ADD mapping in order to constrain the problem, linking IA and EA estimates. Robustness of microstructural features to noise should also be explored in order to propose a method applicable to real dMRI signals.

As pointed out earlier, Westin et al. [99] linked characteristics of the b-tensor used for encoding and the 4th and higher orders of the diffusion tensor. Such acquisitions might provide higher sensitivity to the higher order components, providing improved fitting performance.

6.5 Conclusion

This chapter shows that the EA signal is better characterized when using the HOTmix model compared to standard tensor models. The last chapter will present preliminary results regarding ADD mapping when including such a model for the EA compartment.

7 Joint model

Overview

In Chapter 4, ADD reconstruction was shown to be robust when using the IA signal and the ActiveAx protocol. However, estimates were biased when considering the EA compartment. A richer PGSE protocol was proposed in Chapter 5, which improved the reconstruction of unimodal and bimodal ADDs. A new model to characterize the EA dMRI signal was also proposed in Chapter 6. In this chapter, we explore whether ADD reconstruction from the full signal (IA and EA) can be improved by using the protocol proposed in Chapter 5 and the HOTmix model to describe the EA compartment.

7.1 Introduction

As pointed out by Burcaw et al. [18] and De Santis et al. [27], improper modeling of the EA space might be a major factor in the overestimation of the mean diameter index observed when comparing ActiveAx_{MMWMD} to histology. The same observation is likely to hold for ADD estimation. As seen previously, robust ADD estimates can be obtained from noisy IA signals using an ActiveAx protocol. The aims of the experiments described hereafter are to explore the benefits of using another protocol designed to maximize sensitivity to a set of diameters, and of using the HOTmix model, in terms of ADD reconstruction accuracy.

7.2 Methods

The different models used in this chapter were tested on a selection of substrates with 18 different gamma distributions and 70% packing density.

We first focused on the 20-shell protocol proposed in Chapter 5. The EA signal was computed using our in-house MC simulator [81], as done in Chapter 4, and mixed with the IA signal such that the IA volume fraction was of 70%. For the fitting, we used the ActiveAx_{ADD} formulation,

namely a dictionary with an IA and an EA compartment. The dictionary was build with a selection of cylinders to model the IA compartment (as done in Chapter 4), and either (i) a mixture of zeppelins (to explore the benefits of using a richer protocol compared to the ActiveAx protocol) or (ii) the HOTmix model to characterize the EA compartment (as done in Chapter 6, to explore the benefits of using such a model for the EA compartment instead of a mixture of zeppelins). No time-dependent term was used for $D_{\perp}^{(2)}$ as experiments in the previous chapter showed that the instantaneous diffusivity varied only slightly over the diffusion times used in our simulations and the size of WM mimicking cylinders. Furthermore, including time-dependence in the HOTmix model didn't improve the results compared to the basic HOTmix model.

As results improved when using HOTmix instead of a mixture of zeppelins, but were not perfect, we explored whether adding a prior on the IA volume fraction could improve the ADD reconstruction. In practice, if the IA volume fraction was to be known, it could be translated into the problem by adding a row of ones to the IA columns, and zeros to the EA columns. The signal to be fit should be extended with a value being equal to the IA volume fraction (set to be 70% in this case). This should promote solutions to the problem for which the sum of the IA weights is close to the estimated IA volume fraction.

7.3 Results

Figure 7.1 shows the estimated ADD for 3 different substrates using either the IA signal only (1st row), the whole signal with zeppelins for the EA compartment (2nd row), the whole signal with the HOTmix model (3rd row), and the whole signal with the HOTmix model and a prior on the IA volume fraction (4th row).

Similarly to the results using the ActiveAx protocol, the addition of the EA space had a relatively minor effect on the ADD estimates for substrates with low diameter index. However, for substrates with higher diameter index, the estimated ADD was heavily biased. The reconstructed ADD was bimodal even though the ground-truth was generated using a gamma distribution (Figure 7.1, 2nd row).

The use of the HOTmix model improved ADD estimates of substrates with large cylinders, but worsened the estimated ADD for substrates with small cylinders (Figure 7.1, 3rd row).

Finally, the addition of a prior on the IA volume fraction slightly improved the ADD reconstruction for substrates with small cylinders, but worsened the ADD estimates for substrates with large cylinders, as a spurious peak appeared at the end of the ADD (Figure 7.1, 4th row).

The l2-norm between the largest cylinder used in the IA dictionary and the closest atom in the EA dictionary was found to be 0.18 for the mixture of zeppelins, and 0.15 for the HOTmix model (for 1'200 diffusion weighted samples). Even though the HOTmix model improved the reconstruction of the EA signal, some of its components were closer to the signal of a cylinder

compared to the axi-symmetric tensors used previously. When reconstructing the ADD from the joint model, the IA signal was therefore more likely to be captured by components of the HOTmix model. Furthermore, the condition number of the dictionary was found to be 3.6×10^{16} when using a mixture of zeppelins for the EA compartment, and it raised to 1.7×10^{17} when using the HOTmix model. Using the HOTmix model therefore made the problem more ill-conditioned compared to using axi-symmetric tensors.

7.4 Discussion

Using the HOTmix model to characterize the EA compartment had a limited impact on ADD estimation. As shown in the results, ADD estimates improved for substrates with large cylinders, but worsened for substrates with small cylinders.

Regularization might play an important role in the compartment model used for ADD reconstruction. Indeed, no regularization was used for the EA compartment in this experiment [15]. However, HOTmix estimates appear to be sparse (*i.e.* only a few higher order tensors are selected, as observable in Figure 6.6) even though such solutions are not particularly promoted. Promoting such solutions, by applying an l1-penalty on the EA coefficients exclusively, might improve ADD estimates compared to the current approach.

Having a higher correlation between the components of the HOTmix model and cylinders showed that the IA axonal signal was more likely to be captured by components of the HOTmix model, compared to the mixture of axi-symmetric tensors used previously. As the HOTmix model improved the reconstruction of the EA signal, it seems that the EA signal has components that are similar to cylinders (*i.e.* pseudo-restricted pools) which might arise from closely packed cylinders. Improved EA reconstruction might therefore come at the cost of a larger fraction of the IA signal being captured by cylinders in the EA compartment model, and vice versa. Overall, using the HOTmix model coupled to a PGSE sequence seems to make it harder to distinguish between the IA and EA compartments.

Westin et al. [99] proposed a formulation for b-tensors such that some elements can be associated to the higher order components of the diffusion tensor. By properly designing a b-tensor, the contrast to higher order components could be increased. If the IA and EA signals can be better segregated with their higher order components, using b-tensor encoding might be helpful in order to better distinguish the two compartments. Other sequences might also improve the distinction between hindered and restricted compartments, like DDE, as it has recently been shown to reduce model degeneracy [22]. Another viable approach, as the problem seems to be the similarity between the IA and EA compartments, would be to eliminate the EA signal. This can be done by using diffusion spectroscopy with metabolites that are known to be present in the IA compartment only, for example. The first option has the advantage that metabolites have lower diffusivity compared to water, lowering the diameter lower bound and increasing sensitivity to small diameters. It comes at the cost of very large voxel size, challenging the assumption of parallel cylinders. Factoring out the orientation

dependence, using the Spherical Mean Technique (SMT) for example [55], might be an option to circumvent this limitation. Using high b -values to eliminate the EA signal might be easier to achieve on in vivo samples compared to ex vivo samples, as the diffusivity is higher and the EA signal should decay faster to zero compared to ex-vivo samples. Finally, considering different intrinsic diffusivities for the IA and EA compartment [58] might prove to be helpful in order to distinguish between the two compartments.

NODDI_{AMICO} and the framework proposed by Rensonnet et al. [83] use atoms that are mixtures of IA and EA signals. Such an approach might be beneficial here, as the issue seems to be the similarity between the IA and EA signals. In our approach however, there is no constrain avoiding the solution to be made of purely IA atoms, or purely EA atoms, which is never observed in our selection of substrates. In the framework presented by Rensonnet et al. [83], each atom is generated from a MC simulation performed on both the IA and EA compartments, and only one atom is selected per fiber population present in the voxel. The relative volume fractions of the two compartments is therefore fixed, and by selecting only the atom that best fits the signal, the two compartments can easily be segregated.

7.5 Conclusion

This chapter presents preliminary results concerning the use of the protocol designed in Chapter 5 and the HOTmix model presented in Chapter 6, in terms of ADD reconstruction accuracy when considering both the IA and EA compartments. Interestingly, results were ambiguous when using the HOTmix model, showing worse ADD estimates for simulations with small cylinders, but improved ADD reconstruction for simulations with large cylinders. The limiting factor seems to be the similarity of the IA and EA signals. Further work is required in order to provide accurate non-parametric and orientationally invariant ADD estimates from signals including both IA and EA compartments.

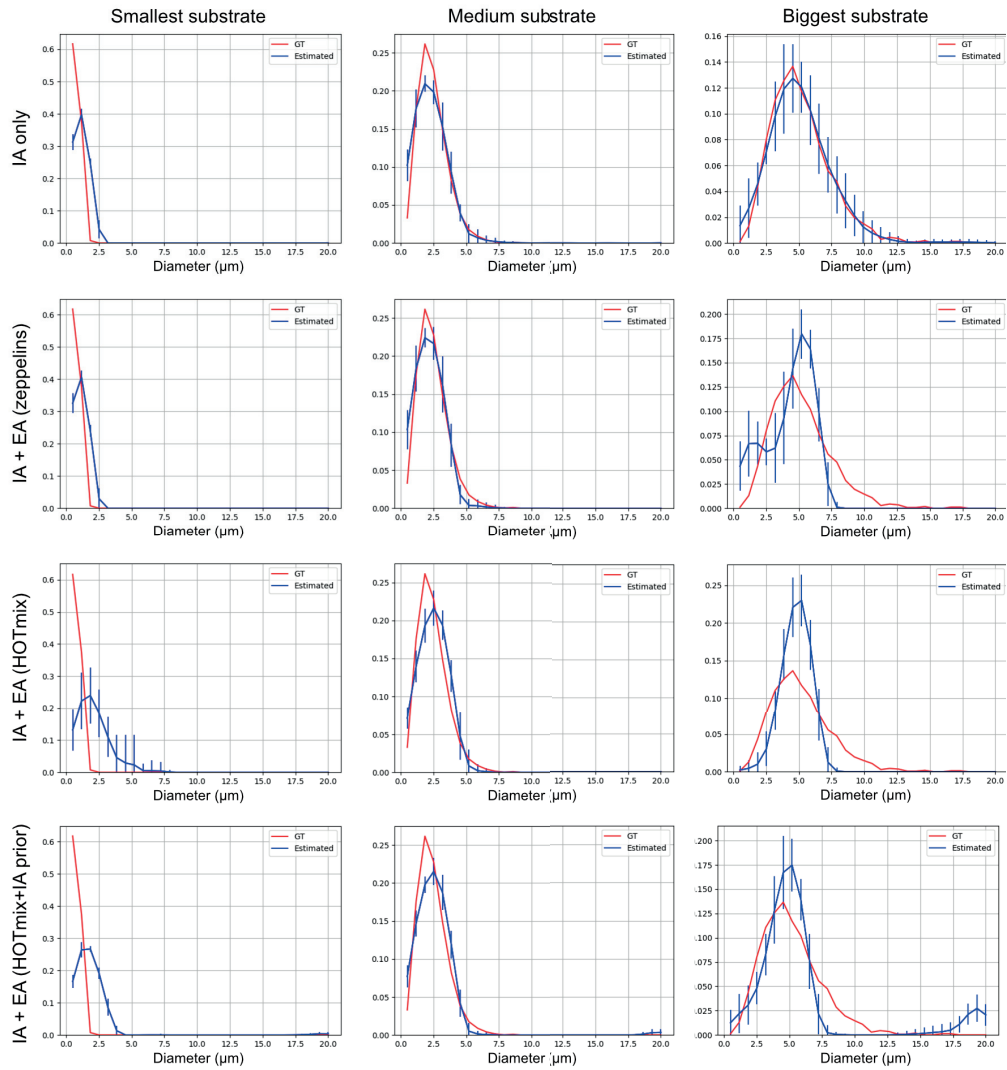


Figure 7.1 – Effect of using a mixture of zeppelins (2nd row) or the HOTmix (3rd row) EA models on the estimated ADD. The first row shows estimates when considering the IA signal only.

8 Conclusion

In this thesis, we have studied the different challenges at stake when estimating Axon Diameter Distributions (ADDs) from diffusion MRI: model degeneracy, the "diameter lower bound", and the difficulty in modeling properly the extra-axonal signal.

Performance was assessed by comparing estimates with ground-truth obtained from MC simulations. The effect of voxel size on the dMRI signal was shown in Chapter 3, and motivated the use of realistic voxel sizes in the remaining chapters.

In Chapter 4, $\text{ActiveAx}_{\text{AMICO}}$ was extended to $\text{ActiveAx}_{\text{ADD}}$ by including Laplacian regularization for the IA compartment. This formulation was shown to better regularize the problem, providing robust ADD estimates for a wide variety of simulated white matter samples. ADD estimates were however worsened when considering the EA compartment.

The diffusion protocol was modified to increase sensitivity to a set of diameters in Chapter 5, showing improved ADD reconstruction when using the IA signal, as well as sensitivity to population specific changes within the distribution, decreasing the degeneracy of the problem.

In Chapter 6, a new model to characterize the EA compartment signal was proposed, and showed better signal reconstructions as compared to other state-of-the-art models.

However, as shown in Chapter 7, different combinations of these specific improvements didn't automatically yield better results in terms of ADD reconstruction when considering both the IA and EA compartments. Even though experiments were focused on a very simple white matter model (perfectly parallel and impermeable cylinders), the similarity between the IA and EA compartment remained a challenging problem.

8.1 Perspectives

From our experimental results, it appeared that a wide variety of ADDs can be reconstructed when using the IA signal. Most acquisitions consist of a mixture of IA and EA signals, but the

Chapter 8. Conclusion

IA signal can be isolated by using diffusion spectroscopy on metabolites that are known to be present in the IA compartment only. The advantage of using such an approach would be the lower diffusivity of metabolites compared to water, which would decrease the diameter lower bound and increase sensitivity to smaller diameters. Specific protocols would nevertheless have to be optimized for such lower diffusivity. As spectroscopy acquisitions have voxel sizes of the order of the centimetre, it is highly unlikely to have perfectly parallel axons within a voxel. ADD estimates should then be performed after factoring out the effect of orientation, either by using the SMT method [55], or isotropic encoding sequences. In the case of crossing fascicles with different ADDs, the estimated distribution might be multi-modal after factoring out the orientation. This should in theory not be a problem for our framework, as shown in Chapter 5, in particular thanks to the lower diffusivity of metabolites. The IA signal can also be isolated by using b-values that are high enough to suppress the EA signal. For ex vivo samples, b-values of $16'000 \text{ mm}^2/\text{s}$ were not enough to suppress the perpendicular component of the EA signal (as shown in Chapter 6 and Chapter 7). However, b-values higher than $6'000 \text{ mm}^2/\text{s}$ should be enough to suppress the EA compartment. In such a picture, the measured signal can be modeled with a mixture of cylinders, giving estimates similar to the ones presented in Chapter 4.

There are several options that might improve ADD estimates from whole signals (IA and EA signals). First, the protocol proposed in Chapter 5 was designed considering the IA signal only. Taking the EA signal into account [2, 13], using the HOTmix model for example, might result in a protocol more suited for ADD estimation. As discussed in Chapter 7, model parameters might be further constrained by imposing relationships between the IA and EA coefficients. Such a relationship could be the tortuosity constrain in $\text{ActiveAx}_{\text{MMWMD}}$ [4]. The parameters might also be constrained to follow the relationship observed between the mean 2nd-order perpendicular diffusivity and the volume weighted mean diameter, as observed in Figure 6.7b. Such constraints might require to implement an iterative fitting procedure, or a non-linear implementation, and might also not improve drastically the estimated ADD.

Our experiments were exclusively based on the Pulsed Gradient Spin Echo sequence. Benjamin et al. [15] showed ADD estimates in the ferret spinal cord that were in agreement with measurements from histology, using Double Diffusion Encoding. The motivation behind using DDE was to reduce the similarity between axons of similar diameter [14, 15]. However, our experiments showed that similar accuracy in ADD reconstruction can be obtained using $\text{ActiveAx}_{\text{ADD}}$ and the signal of the IA compartment. The actual benefit of using DDE might actually be an improved distinction between the hindered and the restricted signal. This might be in line with observations made by Coelho et al. [22] with respect to DDE being able to "prevent degeneracy in parameter estimation of biophysical models in diffusion MRI". The degeneracy mentioned here concerns the IA and EA diffusivity, and DDE might provide IA and EA signals that are less alike compared to PGSE. Careful experiments should be carried on in order to see if using DDE could improve ADD estimates when considering both the IA and EA compartments. Such experiments should include the generation of the EA signal using MC simulations with realistic voxel sizes. If the tensor model turned out to deviate

from the EA signal, the HOTmix model might be of interest to model the EA signal and might be incorporated in the model after deriving its formulation for a DDE sequence. Finally, if using DDE is not a successful approach, other sequences like oscillating gradients [88] or b-tensors [99] might be of interest to explore. Indeed, as pointed out by Westin et al. [99], a link can be expressed between the structure of the b-tensor and higher order components of the diffusion tensor. Properly designing a b-tensor might therefore provide a contrast to better estimated this higher order components, increasing the sensitivity to the differences between the IA and EA compartments.

All the work presented in this thesis was also based on the main assumption that white matter tissue can be represented by infinite, straight, parallel and impermeable cylinders. This approximation might be unrealistic, given the structure observable from electron microscopy and synchrotron imaging. The time-varying behavior of the instantaneous diffusivity estimated from MRI was also observed for the longitudinal diffusivity, but without specificity with respect to the IA or EA compartment [36]. This illustrates the presence of disorder in the parallel direction of the axons, countering the hypothesis that WM can be modelled with perfectly parallel cylinders. For ADD mapping to be applied on real WM signals, the effect of dispersion, permeability and crossings should be examined first. If the effect of such parameters influences the estimated ADD, then they should be included in the formulation of the model. Dispersion might be included in the dictionary, after being estimated using NODDI_{AMICO} [102, 25]. Indeed, each cylinder in the IA model can be generated with a given diameter and dispersion [101]. Crossings can also be modeled by identifying populations using Constrained Spherical Deconvolution (CSD), and the dictionary for ADD mapping replicated for each population, similarly to the work done for the mean diameter index in crossing voxels [8, 83].

A Appendix: Derivation of the axisymmetric HOT model

As all cylinders are perfectly aligned, the medium is isotropically symmetric, meaning that the 4th order tensor only has 6 non-zero terms: $D_{1111}^{(4)}$, $6D_{1122}^{(4)}$, $6D_{1133}^{(4)}$, $D_{2222}^{(4)}$, $6D_{2233}^{(4)}$ and $D_{3333}^{(4)}$. Assuming that diffusion is gaussian along \mathbf{n} and independent of the radial diffusion process, all terms of the 4th order tensor involving index 3 are set to zero. The 4th order tensor can thus be reduced to:

$$b_{i_1 i_2 i_3 i_4}^{(4)} D_{i_1 i_2 i_3 i_4}^{(4)} = b_{1111}^{(4)} D_{1111}^{(4)} + 6b_{1122}^{(4)} D_{1122}^{(4)} + b_{2222}^{(4)} D_{2222}^{(4)}.$$

Expanding the expression of the b-value gives:

$$b_{i_1 i_2 i_3 i_4}^{(4)} D_{i_1 i_2 i_3 i_4}^{(4)} = \gamma^4 \delta^4 (\Delta - 3\delta/5) (g_x^4 D_{1111}^{(4)} + 6g_x^2 g_y^2 D_{1122}^{(4)} + g_y^4 D_{2222}^{(4)}).$$

Assuming that the radial dMRI signal is the same for any perpendicular gradient with amplitude G_\perp ; that $D_{1111}^{(4)} = D_{2222}^{(4)} = D_\perp^{(4)}$; and considering two radial diffusion gradients \mathbf{g}_1 and \mathbf{g}_2 with angles α_1 and α_2 with respect to the x-axis respectively, such that $\|\mathbf{g}_1\| = \|\mathbf{g}_2\| = G_\perp$, the following must hold:

$$D_\perp^{(4)} (g_{1,x}^4 + g_{1,y}^4) + 6g_{1,x}^2 g_{1,y}^2 D_{1122}^{(4)} = D_\perp^{(4)} (g_{2,x}^4 + g_{2,y}^4) + 6g_{2,x}^2 g_{2,y}^2 D_{1122}^{(4)}$$

As

$$g_{1,x} = G_\perp \cos(\alpha_1), \text{ and}$$

$$g_{1,y} = G_\perp \sin(\alpha_1)$$

Appendix A. Appendix: Derivation of the axi-symmetric HOT model

then

$$\begin{aligned} g_{1,x}^4 + g_{1,y}^4 &= G_{\perp}^4 ((\cos^2(\alpha_1) + \sin^2(\alpha_1))^2 - 2\cos^2(\alpha_1)\sin^2(\alpha_1)) \\ &= G_{\perp}^4 (1 - 2\cos^2(\alpha_1)\sin^2(\alpha_1)). \end{aligned}$$

Similarly,

$$g_{2,x}^4 + g_{2,y}^4 = G_{\perp}^4 (1 - 2\cos^2(\alpha_2)\sin^2(\alpha_2)).$$

Furthermore,

$$\begin{aligned} g_{1,x}^2 g_{1,y}^2 &= G_{\perp}^4 \cos^2(\alpha_1) \sin^2(\alpha_1), \text{ and} \\ g_{2,x}^2 g_{2,y}^2 &= G_{\perp}^4 \cos^2(\alpha_2) \sin^2(\alpha_2). \end{aligned}$$

The previous equation then becomes:

$$\begin{aligned} G_{\perp}^4 D_{\perp}^{(4)} (1 - 2\cos^2(\alpha_1)\sin^2(\alpha_1)) + 6G_{\perp}^4 \cos^2(\alpha_1)\sin^2(\alpha_1) D_{1122}^{(4)} = \\ G_{\perp}^4 D_{\perp}^{(4)} (1 - 2\cos^2(\alpha_2)\sin^2(\alpha_2)) + 6G_{\perp}^4 \cos^2(\alpha_2)\sin^2(\alpha_2) D_{1122}^{(4)} \end{aligned}$$

$$\begin{aligned} 6\cos^2(\alpha_1)\sin^2(\alpha_1) D_{1122}^{(4)} - 6\cos^2(\alpha_2)\sin^2(\alpha_2) D_{1122}^{(4)} = \\ D_{\perp}^{(4)} (1 - 2\cos^2(\alpha_2)\sin^2(\alpha_2)) - D_{\perp}^{(4)} (1 - 2\cos^2(\alpha_1)\sin^2(\alpha_1)) \end{aligned}$$

$$\begin{aligned} 3D_{1122}^{(4)} (2\cos^2(\alpha_1)\sin^2(\alpha_1) - 2\cos^2(\alpha_2)\sin^2(\alpha_2)) = \\ D_{\perp}^{(4)} (1 - 2\cos^2(\alpha_2)\sin^2(\alpha_2) - 1 + 2\cos^2(\alpha_1)\sin^2(\alpha_1)) \end{aligned}$$

$$\begin{aligned} 3D_{1122}^{(4)} (2\cos^2(\alpha_1)\sin^2(\alpha_1) - 2\cos^2(\alpha_2)\sin^2(\alpha_2)) = \\ D_{\perp}^{(4)} (2\cos^2(\alpha_1)\sin^2(\alpha_1) - 2\cos^2(\alpha_2)\sin^2(\alpha_2)) \end{aligned}$$

$$3D_{1122}^{(4)} = D_{\perp}^{(4)}$$

$$D_{1122}^{(4)} = D_{\perp}^{(4)} / 3$$

The expression for the 4th order tensor can thus be written as:

$$b_{i_1 i_2 i_3 i_4}^{(4)} D_{i_1 i_2 i_3 i_4}^{(4)} = \gamma^4 \delta^4 (\Delta - 3\delta/5) D_{\perp}^{(4)} (g_x^4 + 2g_x^2 g_y^2 + g_y^4).$$

Coming back to an arbitrary diffusion gradient \mathbf{g} such that $\|\mathbf{g}\| = G$, we have

$$G \sin(\alpha) = \sqrt{g_x^2 + g_y^2},$$

so

$$g_x^4 + 2g_x^2 g_y^2 + g_y^4 = G^4 \sin^4(\alpha),$$

and the 4th order tensor finally reduces to:

$$b_{i_1 i_2 i_3 i_4}^{(4)} D_{i_1 i_2 i_3 i_4}^{(4)} = b^{(4)} D_{\perp}^{(4)} \sin^4(\alpha) \quad (\text{A.1})$$

where $b^{(4)} = \gamma^4 G^4 \delta^4 (\Delta - 3\delta/5)$. Equation 6.2 then becomes:

$$\begin{aligned} \ln(S/S_0) = & -b^{(2)} D_{\parallel}^{(2)} \cos^2(\alpha) - b^{(2)} D_{\perp}^{(2)} \sin^2(\alpha) \\ & + b^{(4)} D_{\perp}^{(4)} \sin^4(\alpha). \end{aligned} \quad (\text{A.2})$$

Bibliography

- [1] ABOITIZ, F., SCHEIBEL, A. B., FISHER, R. S., AND ZAIDEL, E. Fiber composition of the human corpus callosum. *Brain Res.* 598, 1-2 (dec 1992), 143–153.
- [2] ALEXANDER, D. C. A general framework for experiment design in diffusion MRI and its application in measuring direct tissue-microstructure features. *Magn. Reson. Med.* 60, 2 (aug 2008), 439–48.
- [3] ALEXANDER, D. C., DYRBY, T. B., NILSSON, M., AND ZHANG, H. Imaging brain microstructure with diffusion MRI: practicality and applications. *NMR Biomed.* (2017).
- [4] ALEXANDER, D. C., HUBBARD, P. L., HALL, M. G., MOORE, E. A., PTITO, M., PARKER, G. J. M., AND DYRBY, T. B. Orientationally invariant indices of axon diameter and density from diffusion MRI. *Neuroimage* 52, 4 (oct 2010), 1374–89.
- [5] ASSAF, Y., AND BASSER, P. J. P. Composite hindered and restricted model of diffusion (CHARMED) MR imaging of the human brain. *Neuroimage* 27, 1 (2005), 48–58.
- [6] ASSAF, Y., BLUMENFELD-KATZIR, T., YOVEL, Y., AND BASSER, P. J. AxCaliber: a method for measuring axon diameter distribution from diffusion MRI. *Magn. Reson. Med.* 59 (2008), 1347–1354.
- [7] ASSAF, Y., FREIDLIN, R. Z., ROHDE, G. K., AND BASSER, P. J. New modeling and experimental framework to characterize hindered and restricted water diffusion in brain white matter. *Magn. Reson. Med.* 52, 5 (nov 2004), 965–78.
- [8] AURÍA RASCLOSA, A., ROMASCANO, D. P. R., CANALES-RODRIGUEZ, E., WIAUX, Y., DIRBY, T. B., ALEXANDER, D., THIRAN, J.-P., AND DADUCCI, A. Accelerated Microstructure Imaging via Convex Optimisation for regions with multiple fibres (AMICOx). In *IEEE Int. Conf. Image Process. 2015* (2015).
- [9] BADEA, A., KANE, L., ANDERSON, R. J., QI, Y., FOSTER, M., COFER, G. P., MEDVITZ, N., BUCKLEY, A. F., BADEA, A. K., WETSEL, W. C., AND COLTON, C. A. The fornix provides multiple biomarkers to characterize circuit disruption in a mouse model of Alzheimer’s disease. *Neuroimage* 142 (nov 2016), 498–511.

Bibliography

- [10] BARAZANY, D., BASSER, P. J., AND ASSAF, Y. In vivo measurement of axon diameter distribution in the corpus callosum of rat brain. *Brain* 132, Pt 5 (may 2009), 1210–20.
- [11] BASSER, P. J., MATTIELLO, J., AND LEBIHAN, D. Estimation of the effective self-diffusion tensor from the NMR spin echo. *J. Magn. Reson. B* 103, 3 (mar 1994), 247–54.
- [12] BASSER, P. J., AND PIERPAOLI, C. Microstructural and physiological features of tissues elucidated by quantitative-diffusion-tensor MRI. *J. Magn. Reson. B* 111, 3 (jun 1996), 209–19.
- [13] BENJAMINI, D., KATZ, Y., AND NEVO, U. A proposed 2D framework for estimation of pore size distribution by double pulsed field gradient NMR. *J. Chem. Phys.* 137, 22 (2012), 224201.
- [14] BENJAMINI, D., KOMLOSH, M. E., BASSER, P. J., AND NEVO, U. Nonparametric pore size distribution using d-PFG: Comparison to s-PFG and migration to MRI. *J. Magn. Reson.* 246 (2014), 36–45.
- [15] BENJAMINI, D., KOMLOSH, M. E., HOLTZCLAW, L. A., NEVO, U., AND BASSER, P. J. White matter microstructure from nonparametric axon diameter distribution mapping. *Neuroimage* 135 (2016), 333–344.
- [16] BENVENISTE, H., HEDLUND, L. W., AND JOHNSON, G. A. Mechanism of detection of acute cerebral ischemia in rats by diffusion-weighted magnetic resonance microscopy. *Stroke.* 23, 5 (may 1992), 746–54.
- [17] BUDDE, M. D., AND FRANK, J. A. Neurite beading is sufficient to decrease the apparent diffusion coefficient after ischemic stroke. *Proc. Natl. Acad. Sci. U. S. A.* 107, 32 (aug 2010), 14472–7.
- [18] BURCAW, L. M., FIEREMANS, E., AND NOVIKOV, D. S. Mesoscopic structure of neuronal tracts from time-dependent diffusion. *Neuroimage* 114 (jul 2015), 18–37.
- [19] BUSZA, A. L., ALLEN, K. L., KING, M. D., VAN BRUGGEN, N., WILLIAMS, S. R., AND GADIAN, D. G. Diffusion-weighted imaging studies of cerebral ischemia in gerbils. Potential relevance to energy failure. *Stroke.* 23, 11 (nov 1992), 1602–12.
- [20] CARUYER, E., LENGLET, C., SAPIRO, G., AND DERICHE, R. Design of multishell sampling schemes with uniform coverage in diffusion MRI. *Magn. Reson. Med.* 69, 6 (jun 2013), 1534–1540.
- [21] CLUSKEY, S., AND RAMSDEN, D. Mechanisms of neurodegeneration in amyotrophic lateral sclerosis. *Mol. Pathol.* (2001).
- [22] COELHO, S., POZO, J. M., JESPERSEN, S. N., JONES, D. K., AND FRANGI, A. F. Double Diffusion Encoding Prevents Degeneracy in Parameter Estimation of Biophysical Models in Diffusion MRI. *arXiv:1809.05059* (sep 2018).

-
- [23] COLELLO, R. J., POTT, U., AND SCHWAB, M. E. The role of oligodendrocytes and myelin on axon maturation in the developing rat retinofugal pathway. *J. Neurosci.* 14, 5 Pt 1 (may 1994), 2594–605.
- [24] COOK, P., BAI, Y., NEDJATI-GILANI, S., SEUNARINE, K., HALL, M., PARKER, G. J. M., AND ALEXANDER, D. Camino: open-source diffusion-MRI reconstruction and processing. In *14th Annu. Meet. Int. Soc. Magn. Reson. Med.* (2006).
- [25] DADUCCI, A., CANALES-RODRÍGUEZ, E. J., ZHANG, H., DYRBY, T. B., ALEXANDER, D. C., AND THIRAN, J.-P. Accelerated Microstructure Imaging via Convex Optimization (AM-ICO) from diffusion MRI data. *Neuroimage* 105 (jan 2015), 32–44.
- [26] DARDZINSKI, B. J., SOTAK, C. H., FISHER, M., HASEGAWA, Y., LI, L., AND MINEMATSU, K. Apparent diffusion coefficient mapping of experimental focal cerebral ischemia using diffusion-weighted echo-planar imaging. *Magn. Reson. Med.* 30, 3 (sep 1993), 318–25.
- [27] DE SANTIS, S., JONES, D. K., AND ROEBROECK, A. Including diffusion time dependence in the extra-axonal space improves in vivo estimates of axonal diameter and density in human white matter. *Neuroimage* 130 (2016), 91–103.
- [28] DELUCA, G. C., EBERS, G. C., AND ESIRI, M. M. Axonal loss in multiple sclerosis: a pathological survey of the corticospinal and sensory tracts. *Brain* 127, 5 (feb 2004), 1009–1018.
- [29] DOLLÉ, J.-P., MORRISON, B., SCHLOSS, R. S., YARMUSH, M. L., AND YARMUSH, M. L. Brain-on-a-chip microsystem for investigating traumatic brain injury: Axon diameter and mitochondrial membrane changes play a significant role in axonal response to strain injuries. *Technology* 2, 2 (jun 2014), 106.
- [30] DROBNJAK, I., ZHANG, H., IANUS, A., KADEN, E., AND ALEXANDER, D. C. PGSE, OGSE, and Sensitivity to Axon Diameter in Diffusion MRI: Insight from a Simulation Study. *Magn. Reson. Med.* 75 (2016), 688–700.
- [31] DYRBY, T., SOGAARD, L., HALL, M., PTITO, M., AND ALEXANDER, D. C. Contrast and stability of the axon diameter index from microstructure imaging with diffusion MRI. *Magn. Reson. Med.* 70 (2013), 711–721.
- [32] DYRBY, T. B., INNOCENTI, G. M., BECH, M., AND LUNDELL, H. Validation strategies for the interpretation of microstructure imaging using diffusion MRI. *Neuroimage* (jun 2018).
- [33] EINSTEIN, A. Über die von der molekularkinetischen Theorie der Wärme geforderte Bewegung von in ruhenden Flüssigkeiten suspendierten Teilchen. *Ann. Phys.* (1905).
- [34] EVANGELOU, N., KONZ, D., ESIRI, M. M., SMITH, S., PALACE, J., AND MATTHEWS, P. M. Size-selective neuronal changes in the anterior optic pathways suggest a differential susceptibility to injury in multiple sclerosis. *Brain* 124, 9 (sep 2001), 1813–1820.

Bibliography

- [35] FAN, Q., NUMMENMAA, A., WICHTMANN, B., WITZEL, T., MEKKAOU, C., SCHNEIDER, W., WALD, L. L., AND HUANG, S. Y. Validation of Diffusion MRI estimates of compartment size and volume fraction in a biomimetic brain phantom using a human MRI scanner with 300 mT/m maximum gradient strength. *Neuroimage* 182 (nov 2018), 469–478.
- [36] FIEREMANS, E., BURCAW, L. M., LEE, H.-H., LEMBERSKIY, G., VERAART, J., AND NOVIKOV, D. S. In vivo observation and biophysical interpretation of time-dependent diffusion in human white matter. *Neuroimage* 129 (apr 2016), 414–427.
- [37] FIEREMANS, E., DE DEENE, Y., DELPUTTE, S., ÖZDEMİR, M. S., ACHTEN, E., AND LEMAHIEU, I. The design of anisotropic diffusion phantoms for the validation of diffusion weighted magnetic resonance imaging. *Phys. Med. Biol.* 53, 19 (oct 2008), 5405–5419.
- [38] GREBENKOV, D. S. Laplacian eigenfunctions in NMR. I. A numerical tool. *Concepts Magn. Reson. Part A* 32A, 4 (jul 2008), 277–301.
- [39] HACKE, W., DONNAN, G., FIESCHI, C., KASTE, M., VON KUMMER, R., BRODERICK, J. P., BROTT, T., FRANKEL, M., GROTTA, J. C., HALEY, E. C., KWIATKOWSKI, T., LEVINE, S. R., LEWANDOWSKI, C., LU, M., LYDEN, P., MARLER, J. R., PATEL, S., TILLEY, B. C., ALBERS, G., BLUHMKI, E., WILHELM, M., AND HAMILTON, S. Association of outcome with early stroke treatment: pooled analysis of ATLANTIS, ECASS, and NINDS rt-PA stroke trials. *Lancet* 363, 9411 (mar 2004), 768–74.
- [40] HALL, M., AND ALEXANDER, D. Convergence and Parameter Choice for Monte-Carlo Simulations of Diffusion MRI. *IEEE Trans. Med. Imaging* 28, 9 (sep 2009), 1354–1364.
- [41] HALL, M. G., NEDJATI-GILANI, G., AND ALEXANDER, D. C. Realistic voxel sizes and reduced signal variation in Monte-Carlo simulation for diffusion MR data synthesis. *Prepr. (arxiv.org, doi1701.03634)* (jan 2017).
- [42] HANSEN, P. C. *Discrete inverse problems : insight and algorithms*. Society for Industrial and Applied Mathematics, 2010.
- [43] HASEGAWA, Y., LATOUR, L. L., SOTAK, C. H., DARDZINSKI, B. J., AND FISHER, M. Temperature dependent change of apparent diffusion coefficient of water in normal and ischemic brain of rats. *J. Cereb. blood flow Metab.* 14, 3 (may 1994), 383–90.
- [44] HOEHN-BERLAGE, M. Diffusion-weighted NMR imaging: application to experimental focal cerebral ischemia. *NMR Biomed.* 8, 7-8 (jan 1995), 345–58.
- [45] HOLLINGSWORTH, K. G., AND JOHNS, M. L. Measurement of emulsion droplet sizes using PFG NMR and regularization methods. *J. Colloid Interface Sci.* 258, 2 (2003), 383–389.

-
- [46] HOROWITZ, A., BARAZANY, D., TAVOR, I., BERNSTEIN, M., YOVEL, G., AND ASSAF, Y. In vivo correlation between axon diameter and conduction velocity in the human brain. *Brain Struct. Funct.* 220, 3 (2015), 1777–1788.
- [47] HUANG, S. Y., NUMMENMAA, A., WITZEL, T., DUVAL, T., COHEN-ADAD, J., WALD, L. L., AND MCNAB, J. A. The impact of gradient strength on in vivo diffusion MRI estimates of axon diameter. *Neuroimage* 106 (feb 2015), 464–472.
- [48] HUGHES, J. R. Autism: the first firm finding = underconnectivity? *Epilepsy Behav.* 11, 1 (aug 2007), 20–4.
- [49] INNOCENTI, G. M., CAMINITI, R., AND ABOITIZ, F. Comments on the paper by Horowitz et al. (2014). *Brain Struct. Funct.* 220, 3 (may 2015), 1789–1790.
- [50] INNOCENTI, G. M., VERCELLI, A., AND CAMINITI, R. The Diameter of Cortical Axons Depends Both on the Area of Origin and Target. *Cereb. Cortex* 24, 8 (aug 2014), 2178–2188.
- [51] JELESCU, I. O., VERAART, J., FIEREMANS, E., AND NOVIKOV, D. S. Degeneracy in model parameter estimation for multi-compartmental diffusion in neuronal tissue. *NMR Biomed.* 29, 1 (jan 2016), 33–47.
- [52] JENSEN, J. H., HELPERN, J. A., RAMANI, A., LU, H., AND KACZYNSKI, K. Diffusional kurtosis imaging: The quantification of non-gaussian water diffusion by means of magnetic resonance imaging. *Magn. Reson. Med.* 53, 6 (jun 2005), 1432–1440.
- [53] JESPERSEN, S. N., LUNDELL, H., SØNDERBY, C. K., AND DYRBY, T. B. Orientationally invariant metrics of apparent compartment eccentricity from double pulsed field gradient diffusion experiments. *NMR Biomed.* 26, 12 (dec 2013), 1647–1662.
- [54] JOHANSEN-BERG, H., AND BEHRENS, T. E. J. *Diffusion MRI: From quantitative measurement to in-vivo neuroanatomy*, academic p ed. Elsevier, 2009.
- [55] KADEN, E., KRUGGEL, F., AND ALEXANDER, D. C. Quantitative mapping of the per-axon diffusion coefficients in brain white matter. *Magn. Reson. Med.* 75, 4 (apr 2016), 1752–1763.
- [56] KELLNER, E., DHITAL, B., KISELEV, V. G., AND REISERT, M. Gibbs-ringing artifact removal based on local subvoxel-shifts. *Magn. Reson. Med.* 76, 5 (nov 2016), 1574–1581.
- [57] KINGSLEY, P. Introduction to diffusion tensor imaging mathematics: Part II. Anisotropy, diffusion-weighting factors, and gradient encoding schemes. *Concepts Magn. Reson. Part A* (2006).
- [58] KUNZ, N., DA SILVA, A. R., AND JELESCU, I. O. Intra- and extra-axonal axial diffusivities in the white matter: which one is faster? *Prepr. (arxiv.org, doi1805.00391)* (may 2018).

Bibliography

- [59] LAMANTIA, A.-S., AND RAKIC, P. Cytological and quantitative characteristics of four cerebral commissures in the rhesus monkey. *J. Comp. Neurol.* 291, 4 (jan 1990), 520–537.
- [60] LASIČ, S., NILSSON, M., LÄTT, J., STÅHLBERG, F., AND TOPGAARD, D. Apparent exchange rate mapping with diffusion MRI. *Magn. Reson. Med.* 66, 2 (aug 2011), 356–365.
- [61] LE, N. T. T., CHANG, L., KOVLYAGINA, I., GEORGIU, P., SAFREN, N., BRAUNSTEIN, K. E., KVARTA, M. D., VAN DYKE, A. M., LEGATES, T. A., PHILIPS, T., MORRISON, B. M., THOMPSON, S. M., PUCHE, A. C., GOULD, T. D., ROTHSTEIN, J. D., WONG, P. C., AND MONTEIRO, M. J. Motor neuron disease, TDP-43 pathology, and memory deficits in mice expressing ALS-FTD-linked UBQLN2 mutations. *Proc. Natl. Acad. Sci. U. S. A.* 113, 47 (nov 2016), E7580–E7589.
- [62] LEE, H.-H., FIEREMANS, E., AND NOVIKOV, D. S. What dominates the time dependence of diffusion transverse to axons: Intra- or extra-axonal water? *Neuroimage* (dec 2017).
- [63] LIEWALD, D., MILLER, R., LOGOTHETIS, N., WAGNER, H.-J., AND SCHÜZ, A. Distribution of axon diameters in cortical white matter: an electron-microscopic study on three human brains and a macaque. *Biol. Cybern.* 108, 5 (oct 2014), 541–57.
- [64] LIU, C., BAMMER, R., ACAR, B., AND MOSELEY, M. E. Characterizing non-gaussian diffusion by using generalized diffusion tensors. *Magn. Reson. Med.* 51, 5 (may 2004), 924–937.
- [65] LOVAS, G., SZILAGYI, N., MAJTENYI, K., PALKOVITS, M., AND KOMOLY, S. Axonal changes in chronic demyelinated cervical spinal cord plaques. *Brain* 123, 2 (feb 2000), 308–317.
- [66] LU, H., JENSEN, J. H., RAMANI, A., AND HELPERN, J. A. Three-dimensional characterization of non-gaussian water diffusion in humans using diffusion kurtosis imaging. *NMR Biomed.* 19, 2 (apr 2006), 236–247.
- [67] MOSELEY, M. E., COHEN, Y., MINTOROVITCH, J., CHILEUITT, L., SHIMIZU, H., KUCHARCZYK, J., WENDLAND, M. F., AND WEINSTEIN, P. R. Early detection of regional cerebral ischemia in cats: comparison of diffusion- and T2-weighted MRI and spectroscopy. *Magn. Reson. Med.* 14, 2 (may 1990), 330–46.
- [68] NEUMAN, C. Spin echo of spins diffusing in a bounded medium. *J. Chem. Phys.* (1974).
- [69] NILSSON, M., LASIC, S., DROBNJAK, I., TOPGAARD, D., AND WESTIN, C.-F. Resolution limit of cylinder diameter estimation by diffusion MRI: The impact of gradient waveform and orientation dispersion. *NMR Biomed.* (2017), e3711.
- [70] NILSSON, M., LÄTT, J., STÅHLBERG, F., WESTEN, D., AND HAGSLÄTT, H. The importance of axonal undulation in diffusion MR measurements: a Monte Carlo simulation study. *NMR Biomed.* 25, 5 (may 2012), 795–805.
- [71] NJIOKIKTJIEN, C., DE SONNEVILLE, L., AND VAAL, J. Callosal size in children with learning disabilities. *Behav. Brain Res.* 64, 1-2 (oct 1994), 213–8.

-
- [72] NOVIKOV, D., AND FIEREMANS, E. Relating extracellular diffusivity to cell size distribution and packing density as applied to white matter. In *ISMRM* (2012), p. 1829.
- [73] NOVIKOV, D. S., JESPERSEN, S. N., KISELEV, V. G., AND FIEREMANS, E. Quantifying brain microstructure with diffusion MRI: Theory and parameter estimation. *arXiv:1612.02059* (dec 2016).
- [74] ÖZARSLAN, E., AND MARECI, T. H. Generalized diffusion tensor imaging and analytical relationships between diffusion tensor imaging and high angular resolution diffusion imaging. *Magn. Reson. Med.* 50, 5 (nov 2003), 955–965.
- [75] ÖZARSLAN, E., SHEMESH, N., AND BASSER, P. J. A general framework to quantify the effect of restricted diffusion on the NMR signal with applications to double pulsed field gradient NMR experiments. *J. Chem. Phys.* 130, 10 (mar 2009), 104702.
- [76] PALOMBO, M., LIGNEUL, C., HERNANDEZ-GARZON, E., AND VALETTE, J. Can we detect the effect of spines and leaflets on the diffusion of brain intracellular metabolites? *Neuroimage* (may 2017).
- [77] PANAGIOTAKI, E., SCHNEIDER, T., SIOW, B., HALL, M. G., LYTHGOE, M. F., AND ALEXANDER, D. C. Compartment models of the diffusion MR signal in brain white matter: A taxonomy and comparison. *Neuroimage* 59, 3 (feb 2012), 2241–2254.
- [78] PIVEN, J., BAILEY, J., RANSON, B., AND ARNDT, S. An MRI study of the corpus callosum in autism. *Am. J. Psychiatry* 154, 8 (1997), 1051–1056.
- [79] RAFAEL-PATIÑO, J., GIRARD, G., ROMASCANO, D., BARAKOVIC, M., RENSONNET, G., THIRAN, J.-P., AND DADUCCI, A. Realistic 3D Fiber Crossing Phantom Models for Monte Carlo Diffusion Simulations. In *26th Annu. Meet. Int. Soc. Magn. Reson. Med.* (2018).
- [80] RAFAEL-PATIÑO, J., RAMIREZ-MANZANARES, A., PEÑA, J., AND ZHANG, H. Validating Particle Dynamics in Monte Carlo Diffusion Simulation Using the Finite Element Method. In *25th Annu. Meet. Int. Soc. Magn. Reson. Med.* (2017).
- [81] RAFAEL-PATIÑO, J., ROMASCANO, D., RAMIREZ-MANZANARES, A., GIRARD, G., CANALES-RODRIGUEZ, E., DADUCCI, A., AND THIRAN, J.-P. Towards realistic designs for Monte Carlo Simulations in Diffusion MRI. *NeuroImage (submitted)* (2018).
- [82] RANDALL, P. L. Schizophrenia, abnormal connection, and brain evolution. *Med. Hypotheses* 10, 3 (mar 1983), 247–80.
- [83] RENSONNET, G., SCHERRER, B., JANKOVSKI, A., WARFIELD, S. K., MACQ, B., THIRAN, J.-P., AND TAQUET, M. Towards microstructure fingerprinting: estimation of tissue properties from a dictionary of Monte Carlo diffusion MRI simulations. *NeuroImage (accepted)* (2018).

Bibliography

- [84] RICE, D., AND BARONE, S. Critical periods of vulnerability for the developing nervous system: evidence from humans and animal models. *Environ. Health Perspect.* 108 Suppl (jun 2000), 511–33.
- [85] ROMASCANO, D., BARAKOVIC, M., RAFAEL-PATIÑO, J., DYRBY, T. B., THIRAN, J.-P., AND DADUCCI, A. ActiveAx-ADD: towards non-parametric and orientationally invariant axon diameter distribution mapping using PGSE. *MRM* (2018).
- [86] SCHERRER, B., SCHWARTZMAN, A., TAQUET, M., SAHIN, M., PRABHU, S. P., AND WARFIELD, S. K. Characterizing brain tissue by assessment of the distribution of anisotropic microstructural environments in diffusion-compartment imaging (DIAMOND). *Magn. Reson. Med.* 76, 3 (sep 2016), 963–977.
- [87] SEPEHRBAND, F., ALEXANDER, D. C., KURNIAWAN, N. D., REUTENS, D. C., AND YANG, Z. Towards higher sensitivity and stability of axon diameter estimation with diffusion-weighted MRI. *NMR Biomed.* 29, 3 (mar 2016), 293–308.
- [88] SIOW, B., DROBNJAK, I., IANUS, A., CHRISTIE, I., LYTHGOE, M., AND ALEXANDER, D. Axon radius estimation with Oscillating Gradient Spin Echo (OGSE) Diffusion MRI. *Diffus. Fundam.* 18, 1 (2013), 1–6.
- [89] STEJSKAL, E. O., AND TANNER, J. E. J. Spin diffusion measurements: spin echoes in the presence of a time-dependent field gradient. *J. Chem. Phys.* 42, 1 (jan 1965), 288–292.
- [90] SZAFAER, A., ZHONG, J., AND GORE, J. Theoretical model for water diffusion in tissues. *Magn. Reson. Med.* (1995).
- [91] TARIQ, M., SCHNEIDER, T., ALEXANDER, D. C., GANDINI WHEELER-KINGSHOTT, C. A., AND ZHANG, H. Bingham–NODDI: Mapping anisotropic orientation dispersion of neurites using diffusion MRI. *Neuroimage* 133 (jun 2016), 207–223.
- [92] TASAKI, I., ISHII, K., AND ITO, H. On the relation between the conduction-rate, the fiber-diameter and the internodal distance of the medullated nerve fiber. *Jpn J Med Sci III, Biophys.* 9 (1943), 189–199.
- [93] TOMASI, S., CAMINITI, R., AND INNOCENTI, G. M. Areal Differences in Diameter and Length of Corticofugal Projections. *Cereb. Cortex* 22, 6 (jun 2012), 1463–1472.
- [94] TRAPP, B. D., PETERSON, J., RANSOHOFF, R. M., RUDICK, R., MÖRK, S., AND BÖ, L. Axonal Transection in the Lesions of Multiple Sclerosis. *N. Engl. J. Med.* 338, 5 (jan 1998), 278–285.
- [95] VAN DER TOORN, A., SYKOVÁ, E., DIJKHUIZEN, R. M., VORÍSEK, I., VARGOVÁ, L., SKOBISOVÁ, E., VAN LOOKEREN CAMPAGNE, M., REESE, T., AND NICOLAY, K. Dynamic changes in water ADC, energy metabolism, extracellular space volume, and tortuosity in neonatal rat brain during global ischemia. *Magn. Reson. Med.* 36, 1 (jul 1996), 52–60.

-
- [96] VAN GELDEREN, P., DESPRES, D., VAN ZIJL, P. C., AND MOONEN, C. T. Evaluation of restricted diffusion in cylinders. Phosphocreatine in rabbit leg muscle. *J. Magn. Reson. B* 103, 3 (mar 1994), 255–60.
- [97] VERAART, J., FIEREMANS, E., AND NOVIKOV, D. S. Diffusion MRI noise mapping using random matrix theory. *Magn. Reson. Med.* 76, 5 (nov 2016), 1582–1593.
- [98] WAXMAN, S. Determinants of conduction velocity in myelinated nerve fibers. *Muscle Nerve* 3 (1980), 141–150.
- [99] WESTIN, C.-F., SZCZEPANKIEWICZ, F., PASTERNAK, O., OZARSLAN, E., TOPGAARD, D., KNUTSSON, H., AND NILSSON, M. Measurement tensors in diffusion MRI: generalizing the concept of diffusion encoding. *Med. Image Comput. Comput. Assist. Interv.* 17, Pt 3 (2014), 209–16.
- [100] YABLONSKIY, D. A., BRETTHORST, G. L., AND ACKERMAN, J. J. H. Statistical model for diffusion attenuated MR signal. *Magn. Reson. Med.* 50, 4 (oct 2003), 664–9.
- [101] ZHANG, H., HUBBARD, P. L., PARKER, G. J. M., AND ALEXANDER, D. C. Axon diameter mapping in the presence of orientation dispersion with diffusion MRI. *Neuroimage* 56, 3 (jun 2011), 1301–15.
- [102] ZHANG, H., SCHNEIDER, T., WHEELER-KINGSHOTT, C. A., AND ALEXANDER, D. C. NODDI: practical in vivo neurite orientation dispersion and density imaging of the human brain. *Neuroimage* 61, 4 (jul 2012), 1000–16.

Curriculum Vitae

- **Name:** David Romascano
- **Profession:** Life Science Engineer
- **Nationality:** Swiss and Guatemalan
- **Born:** 14.05.1988

- **Address:** Rue Madeleine 2, 1003 Lausanne, Switzerland
- **Phone:** +41 76 822 47 99
- **E-Mail:** david.romascano@epfl.ch

Education

PhD Student at the LTS5 (EPFL)

November 2014 - Today

PhD conducted at the École Polytechnique Fédérale de Lausanne (EPFL), under the supervision of Prof. Jean-Philippe Thiran and Prof. Dyrby (DRCMR, Denmark). The subject of the thesis is the implementation and evaluation of advanced diffusion MRI techniques for microstructural brain imaging. Mobility project for ex-vivo validation of a new model for white matter microstructure conducted with Prof. Tim Dyrby in Copenhagen during 6 months (April-September 2017).

M.Sc. in Life Science (with an orientation in neurosciences) at EPFL

September 2011 – July 2013

Master project performed under the supervision of Dr. Granziera, on the characterization of structural and functional connectivity differences in the cerebellum of Multiple Sclerosis patients and healthy controls, using Diffusion Spectrum Imaging, resting-state functional MRI, and multi-contrast structural MRI data as T1, T2 and MTR.

B.Sc in Life Science at EPFL

October 2006 – July 2010

Baccalauréat Scientifique at the Lycée Jules Verne in Guatemala

August 2006

Professional Experiences

Scientific collaborator at the EPFL (LTS5)

December 2013 – May 2014

Implementation and release of a beta version for the Connectome Mapper, a tool for diffusion MRI processing developed by the LTS5 group at EPFL.

Scientific collaborator at the CHUV (University Hospital, Neurology department)

May 2011 – September 2011

Conducted a clinical study on structural differences in the cerebellum of migraineurs with or without aura and healthy controls, under the supervision of Dr. Granziera (CHUV), Dr. Krueger (Siemens Healthcare) and Dr. Hadjikhani (EPFL)

Scientific collaborator at the UNIL (CIG)

January 2011 – May 2011

Project on the characterization of the human P RNAse promoter, under the supervision of Dr. Canella and Prof. Hernandez at the Centre Intégré de Génétique (CIG), at the University of Lausanne (UNIL).

Student Assistant at the CHUV (LDCS)

March 2008 – July 2013

Part time assistant for Prof. Barrandon at the Laboratory of Stem Cell Dynamics (LDCS). Several projects involved preparation of histology for autologous skin grafts biopsies, microscopy and analysis, as well as stem cell culture and implementation of automated stem cell classification and monitoring.

Skills & interests

MRI processing: Microstructure Brain imaging, Diffusion MRI, Structural MRI, group statistical analysis, network analysis

Publications: <https://people.epfl.ch/cgi-bin/people?id=175245&op=publications>

Programming languages: Python, Matlab, C++

Spoken languages: Spanish and French (mother tongues), English (fluently spoken and written)

Internships

Internship in Lomé (Togo)

September – November 2014

Based on our experience in Tanzania (see below), we performed an internship in collaboration with Ingénieurs du Monde, Afrik Demain and the Togolese Ministry of Health to conduct a study on healthcare waste management in the city of Lomé in Togo. A detailed report containing instructions to build needle safety boxes as well as printable summaries for safety and waste segregation instructions was handed to the Ministry of Health and visited health facilities.

Internship in Dodoma (Tanzania)

October – December 2013

Internship in collaboration with the Swiss Tropical Institute, Ingénieurs du Monde and the Tanzanian Ministry of Health to conduct a study on healthcare waste management in the region of Dodoma in Tanzania.

